

Project Title: “**Instrumentation and Monitoring of FRP bars in Bridge Deck Link-Slab for FPID 435390-1-52-01**”

Contract Number: BDV34 986-02

Final Report

Submitted by:

<p>Adel ElSafty, Principal Investigator University of North Florida School of Engineering 1 UNF Drive, Jacksonville, FL 32224-2645 Email Address: adel.el-safty@unf.edu Phone Number: (904) 620-1398</p>	<p>James Fletcher, Co-Investigator University of North Florida School of Engineering 1 UNF Drive, Jacksonville, FL 32224-2645 Email Address: jfletche@unf.edu Phone Number: (904) 620-1844</p>
<p>Thomas Fowler Undergraduate Engineering Student University of North Florida School of Engineering 1 UNF Drive, Jacksonville, FL 32224-2645 Email Address: n00880684@unf.edu</p>	<p>Dylan Jones Undergraduate Engineering Student University of North Florida School of Engineering 1 UNF Drive, Jacksonville, FL 32224-2645 Email Address: n01180016@unf.edu</p>

Submitted to: **Steven Nolan**, Project Manager
The Florida Department of Transportation
State Structures Design Office
605 Suwannee Street, MS 33
Tallahassee, FL 32399-0450
Email Address: Steven.Nolan@dot.state.fl.us
Phone: (850) 414-4272

Dr. Cheresa Y. Boston, Director of Sponsored Research
University of North Florida
Office of Research and Sponsored Programs
1 UNF Drive, Jacksonville, Florida 32224
Email: cheresa.boston@unf.edu
Phone: (904) 620-2455, Fax: (904) 620-2457

September 29, 2021

DISCLAIMER

The opinions, findings, and conclusions expressed in the publication are those of the authors and not necessary those of the State of Florida Department of Transportation.

0.1 Metric Conversion Table

Approximate Conversions to SI Units				
Symbol	Known	Conversion Factor	Find	Symbol
Length				
in	inches	25.4	millimeters	mm
ft	feet	0.305	meters	m
yd	yards	0.914	meters	m
Area				
in ²	square inches	645.2	square millimeters	mm ²
ft ²	square feet	0.093	square meters	m ²
yd ²	square yard	0.836	square meters	m ²
Volume				
ft ³	cubic feet	0.028	cubic meters	m ³
yd ³	cubic yards	0.765	cubic meters	m ³
gal	gallons	3.785	Liters	L
Mass				
oz	ounces	28.35	grams	g
lb	pounds	0.454	kilograms	kg
Temperature				
°F	Fahrenheit	5(F-32)/9 or (F-32)/1.8	Celsius	°C
Force and Pressure or Stress				
lbf	poundforce	4.45	Newtons	N
lb/in ²	poundforce/square inch	6.89	kilopascals	kPa
Illumination				
fc	foot-candles	10.76	Lux	lx
fl	foot-Lamberts	3.426	candela/m ²	cd/m ²
Approximate Conversions from SI Unites				
Symbol	Known	Conversion Factor	Find	Symbol
Length				
mm	millimeters	0.039	inches	in
m	meters	3.28	Feet	ft
m	meters	1.09	yards	yd
Area				
mm ²	square millimeters	0.0016	square inches	in ²
m ²	square meters	10.764	square feet	ft ²
m ²	square meters	1.195	square yard	yd ²
Volume				
m ³	cubic meters	35.314	cubic feet	ft ³
m ³	cubic meters	1.307	cubic yards	yd ³
L	liters	0.264	gallons	gal
Mass				
g	grams	0.035	ounces	oz
kg	kilograms	2.202	pounds	lb
Temperature				
°C	Celsius	1.8C+32	Fahrenheit	°F
Force and Pressure or Stress				
N	Newtons	2.225	poundforce	lbf
kPa	kilopascals	0.145	poundforce/square inch	lb/in ²
Illumination				
lx	lux	0.0929	foot-candles	fc
cd/m ²	candela/m ²	0.2919	foot-Lamberts	fl

0.2 Technical Report Documentation Page

1. Report No.	2. Government Accession No.	3. Recipient's Catalog No.	
4. Title and Subtitle BRIDGE DECK WITH LINK-SLAB For FPID: 435390-1-52-01: US 41 from Midway Blvd to Enterprise		5. Report Date	
		6. Performing Organization Code	
7. Author(s) Adel ElSafty and James Fletcher		8. Performing Organization Report No.	
9. Performing Organization Name and Address University of North Florida 1 UNF Drive Jacksonville, FL 32224		10. Work Unit No. (TRAVIS)	
		11. Contract or Grant No. BDV34 986-02	
12. Sponsoring Agency Name and Address		13. Type of Report and Period Covered Final Report	
		14. Sponsoring Agency Code	
15. Supplementary Notes			
16. Abstract The goal of the project is to investigate and monitor the performance of the link-slab that is reinforced with Basalt Fiber Reinforced Polymers bars, BFRP-RC. The research also provided recommendations for the instrumentation of the link-slabs, a suggested monitoring plan, and an instrumentation system to monitor the temperature, strain, and elongation of link-slabs. The research also installed the instrumentation to monitor the link-slab during concrete casting and after casting. The research team started measuring and monitoring the strains, deformations, and cracks in the link-slab. The team also investigated the performance of the link-slab, evaluated the data from installed instrumentation, analyzed the results, and provided conclusions. The strains experienced by the sensors indicated small strain levels compared to the BFRP ultimate strain levels. In addition to live load flexural effects, this type of thermal cycling could contribute to the concrete cracking over time in the link-slab if tension stresses build-up due to global shrinkage and creep restraint of the connected FSB spans. However, after about 90 days over the time of monitoring, the average strain in the mid-joint gauges did not change significantly indicating minimal creep and or shrinkage restraint was experienced to date by the link-slab since the initial casting date. The strains experienced by the sensors indicated small strain levels compared to the BFRP ultimate strain levels. The maximum daily strain change due to thermal effects is about 500 microstrain.			
17. Key Word		18. Distribution Statement	
19. Security Classif. (of this report) Unclassified	20. Security Classif. (of this page) Unclassified	21. No. of Pages	22. Price

0.3 Executive Summary

Bridge deck joints are costly to buy, install, and maintain; providing severe performance and maintenance problems. One of the solutions is to adopt jointless bridges and eliminate expansion joints in bridge decks. That has been an effective method of constructing bridges. It corresponds to reduced maintenance and improved bridge-deck life expectancy. Using a link-slab and making the bridge girders (partially continuous) continuous only for lateral and longitudinal load effects, provides lower cost, improved durability, longer spans, improved seismic performance, better resistance to wind loads and storm wave loads, improved structural integrity, and improved riding quality. There is a need for simple guidelines for design and detailing of the popular connection system for jointless bridge using a deck link-slab, that is continuous for lateral and longitudinal load effects, but not for vertical live load effects.

The aim of this research is to investigate the performance of the link-slab using BFRP-RC. In specific, the overall goal of the project is to investigate and monitor the performance of the link-slab that is reinforced with BFRP-RC on Bridge No. 019003 over Morning Star Waterway. The team investigated the feasibility of an innovative system for reducing or eliminating the number of bridge deck joints using link-slab. The research also provided recommendations for the instrumentation of the link-slab, a suggested monitoring plan, and an instrumentation system to monitor the temperature, strain, and elongation of link-slabs. The research also installed the instrumentation to monitor the link-slab during concrete casting and after casting. The research team started measuring and monitoring the strains, deformations, and cracks in the link-slab. The team also investigated the performance of the link-slab, evaluated the data from installed instrumentation, analyzed the results, and provided conclusions.

The research team investigated the concrete simple-span beams that are made continuous by pouring a continuity link-slab between the beam ends. The bridge has been instrumented with embedded and surface-mounted sensors and has been monitored to evaluate the performance of the new link-slab. Several types of sensors were used, and a data acquisition system recorded strains/deformations at a regular time interval. The preferred sensor types for this application are vibrating wire sensors with integrated thermistors (per FDOT request). The sensors were strategically located on both sides of the midline of the link slab to capture strains in the BFRP bars, strains in the concrete link-slab, and the gap between adjacent beams' ends.

All measurements have been corrected for temperature changes per recommendations of the gauge manufacturer. Data has been collected during service over two periods of approximately 3 months each. The data acquisition system has been able to keep record of strains developed in the BFRP reinforcement. The strains experienced by the sensors indicated small strain levels compared to the BFRP ultimate strain levels. In addition to live load flexural effects, this type of thermal cycling could contribute to the concrete cracking over time in the link-slab if tension stresses build-up due to global shrinkage and creep restraint of the connected FSB spans. However, after about 90 days over the time of monitoring, the average strain in the mid-joint gauges did not change significantly indicating minimal creep and or shrinkage restraint was experienced to date by the link-slab since the initial casting date. The strains

experienced by the sensors indicated small strain levels compared to the BFRP ultimate strain levels. The maximum daily strain change due to thermal effects is about 500 microstrain.

0.4 Contents

0.1	Metric Conversion Table	3
0.2	Technical Report Documentation Page.....	4
0.3	Executive Summary	5
0.4	Contents	7
0.5	List of Figures	8
0.6	List of Tables	9
1	Introduction	10
1.1	Background Statement	10
1.2	Research Approach	12
1.3	Literature Review.....	12
2	Instrumentation	13
2.1	Embedded sensors.....	13
2.1.1	Sensor Wiring and Cables:.....	20
2.1.2	Cable Routing	21
2.2	Data Acquisition	21
2.3	Sensor setup	24
3	Data Reduction	28
3.1	Data reduction for Strandmeters	28
3.2	Data reduction for Sisterbars.....	29
4	Results and Data Analysis	30
4.1	Amendments to the dataset	30
4.2	Graphs of reduced data	30
4.3	Samples of reduced data	35
4.4	Results and Analysis	36
5	Evaluation of FDOT Link-Slab Details	37
6	Summary	38
7	References	39
8	Appendix A Images and Illustrations of The Bridge and Sensor Layout	42
9	Appendix B Sensor Layout and Information	46
10	Appendix C Manufacturer’s instrument datasheets	51
11	Appendix D Literature Review	61
12	Appendix E Annotated Plans Details For Link-Slab MONITORING PROJECT BDV34 986-02	87

0.5 List of Figures

Figure 1.1: Link Slab Option	11
Figure 2.1: Location of embedded sensor array, top view	15
Figure 2.2: Schematic of Strandmeter (Red) and Sisterbar (Green & Blue) placement	15
Figure 2.3: Link slab reinforcement and embedded sensors	16
Figure 2.4: Link-slab photos prior to setting reinforcement.....	17
Figure 2.5: Finished link slab and close up view	17
Figure 2.6: Data acquisition modules and wiring	18
Figure 2.7: Vandalized surface mounted crackmeters	18
Figure 2.8: Southwest outboard EDTs.....	19
Figure 2.9: External displacement transducers	19
Figure 2.10: Cable routing through EPS.....	21
Figure 2.11: Detail of embedded sensor routing, side view.....	21
Figure 2.12: Details of embedded sensors and wiring, top view	23
Figure 2.13: Sensor setup in LogView software.....	27
Figure 4.1: Graphed deformation from Strandmeters	31
Figure 4.2: Graphed strain from Strandmeters.....	32
Figure 4.3: Graphed load related strain from Sisterbars	33
Figure 4.4: Graphed actual strain from Sisterbars	34

0.6 List of Tables

Table 1: List of Geokon sensors serial numbers	23
Table 2: First 20 data points of Strandmeter deformation	35
Table 3: First 20 data points of Strandmeter microstrain.....	35
Table 4: First 20 data points of load related microstrain from Sisterbars	36
Table 5: First 20 data points of actual microstrain from Sisterbars	36

1 Introduction

1.1 Background Statement

Bridge deck expansion joints are costly to buy, install, and maintain. They have provided severe performance and maintenance problems as water and deck drainage contaminated with chemicals leak through the superstructure and onto the pier caps below, thus damaging or eventually compromising some vital parts of bridges such as prestressing cable anchorage systems, beams, bearings, substructure seat areas, and end diaphragms. Also, debris accumulation in the joints may restrain deck expansion (ElSafty 1994).

One of the proposed solutions is to adopt jointless bridges and eliminate expansion joints in bridge decks. This has been an effective method of constructing bridges in many states. It corresponds to reduced maintenance and improved bridge-deck life expectancy. It is possible to replace bearing devices with simple elastomeric pads, or totally integrate the superstructure with the supports. With the use of jointless bridge decks, there are no joints to purchase and reduced bearing maintenance, the riding surface is smoother, the initial and life-cycle cost are lower, and there may be some reduction in span bending moments and deflections, but this is not considered in the design. In conclusion, using a link-slab and making the bridge girders (partially continuous) continuous provides lower cost, improved durability, longer spans, improved seismic performance, better resistance to wind loads and storm wave loads, improved structural integrity, and improved riding quality. Current consensus seems to allow elimination of expansion joints on bridges as long as 650 feet. Much longer bridges have occasionally been constructed without reported distress. There is a need for simple guidelines for design and detailing of the popular connection system. An option for jointless bridge deck link-slab is shown in Fig. 1. A brief literature review of link-slab is provided in Appendix D.

The aim of this research is to investigate the performance of the link-slab using Basalt Fiber-Reinforced Polymer (BFRP) reinforcing bars in a Reinforced Concrete (RC) deck (structural overlay) on the Florida Slab Beams (FSB) for a two-span pedestrian bridge along US-41 over Morningstar Waterway. Details of the bridge link-slab are provided in Appendix E. The team evaluated the data from installed instrumentation, analyzed the results, and provided conclusions.

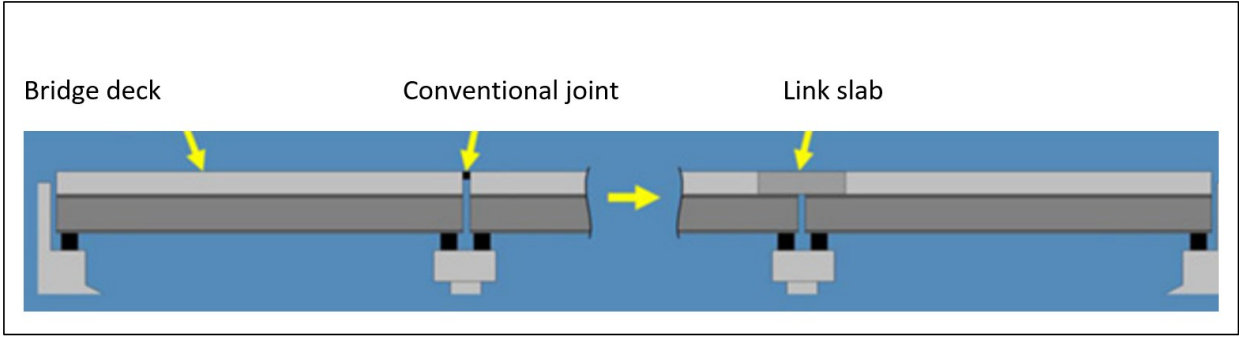


Figure 1.1: Link Slab Option

1.2 Research Approach

The methodology for addressing the problem was to break down the solution process into four tasks (deliverables) – (1) literature review, (2) recommendations on instrumentation and monitoring of the link slab, (3) installing instrumentation and monitoring the link slab after casting, (4) and evaluate the data from the instrumentation within the link slab.

The purpose of the literature review was to further investigate the feasibility of an innovative system for reducing or eliminating the number of bridge deck joints.

The purpose of the second task was to provide recommendations for the instrumentation of the link-slabs, a suggested monitoring plan, and an instrumentation system to monitor the temperature, strain, rotation, and elongation of different link-slabs.

The purpose of the third task was to install the instrumentation to monitor the FDOT designed link-slab during concrete casting and periodically for the following 90 days. For the investigated bridge link-slab, the research team started measuring and monitoring the strains, deformations, and cracks in the link-slab. Due to project delays a second period of monitoring for 75 days was possible.

The purpose of the fourth task was to investigate the performance of the link-slab. The data from the instrumentation was evaluated and provided enough information to draw preliminary conclusions.

The overall goal of the project is to investigate and monitor the performance of the link-slab that is reinforced with BFRP-RC on Bridge No. 019003 over Morning Star Waterway.

1.3 Literature Review

A literature review has been conducted on the link-slab and jointless bridge decks. The literature review is presented in Appendix D.

2 Instrumentation

The research team developed a monitoring plan and instrumentation system to monitor the temperature, strain, and elongation of link-slabs. The team investigated the concrete simple-span beams that are made continuous by pouring a continuity link-slab between the beam ends. The bridge has been instrumented with embedded and surface-mounted sensors and has been monitored to evaluate the performance of the new link-slab. Several types of sensors were used, and a data acquisition system recorded strains/deformations at a regular time interval. The preferred sensor types for this application are vibrating wire sensors with integrated thermistors (per FDOT request). The sensors were strategically located on both sides of the midline of the link slab to capture strains in the BFRP bars, strains in the concrete link-slab, and the gap between adjacent beams' ends.

The bridge link-slab monitoring system included sensors, data acquisition system, cabling and conduit. The system installation activities were coordinated between involved parties (FDOT technical team, Contractor and other subcontractors, the project manager, and the research team) to establish the installation schedule and implementation of both the embedded and surface-mounted sensors. The monitoring system including sensors were installed in coordination with the construction contractor and the FDOT representatives.

All measurements have been corrected for temperature changes per recommendations of the gauge manufacturer. Data has been collected periodically during service. Substantial delays occurred in data retrieval due to COVID-19 travel restrictions. As such, two periods (4.5 and 3.5 months) of monitoring data were available over a span of approximately one-year. The data acquisition system has been able to keep record of strains developed in the BFRP reinforcement.

2.1 Embedded sensors

The embedded sensors are for measuring strains within and across the link-slab. This was composed of a 3x3 array of Strandmeters and Sister bar paired to each other, for a total of 18 (9 pairs) embedded sensors. The Strandmeter measures deformation/strains in the BFRP link-slab reinforcement (Geokon model 4410 Strandmeter). The adjacent "Sister bar" (Geokon model 4911 Rebar Strainmeter) measures strain in the link-slab concrete at approximately the same location. It is recommended by BDI Inc. that the sister bar be tied off to its paired strandmeter via loose wire during installation.

Placement of the 3x3 array is a roughly symmetrical location of the 9 pairs of embedded sensors. From the southwest side of the bridge the first three pairs of sensors (labeled as row "A") were located on the fourth BFRP rebar from the southwest side of the link-slab. The second row of three sensor pairs (labeled as row "B") is located on the twelfth BFRP rebar from the

southwest side of the link-slab. The third row of three sensor pairs (labeled as row “C”) is located on the twenty-first BFRP rebar from the southwest side of the link slab. Each pair of sensors in a row is identified by its relative compass position. For example, the northernmost pair of embedded sensors is identified as the “NW-C” location (northwest side, row-C) and the other two pairs within that row are in the “Mid-C” and “SE-C” locations. This layout is shown in the following, Figure 2.1, Location of Embedded Sensor Array, Top View. Note the orientation of a Sister bar relative to its corresponding BFRP rebar is always toward the centerline of the bridge, while the accompanying strandmeter sits sets on the opposite side of the BFRP rebar.

The sensors were installed on 3/7/2020. The first set of data was recovered on 11/14/20 which contained data from 3/7/2020 to 8/2/2020. The second set of data was recovered on 2/28/20 which contained data from 11/14/2020 to 2/28/2021. Data was recorded once every hour.

Strandmeter (model 4410, Geokon): These deformation/strain sensors were clamped to the link-slab longitudinal reinforcement (BFRP rebars inside cast-in-place link-slab) at the specified locations. Special treatment per the product manual dictates surrounding sensor with grease prior to encasing inside concrete. BDI advised that the strandmeter sensor (model 4410) is preferable in this application because it is readily attached to a rounded surface (i.e. the reinforcement bars) and is more appropriate for embedment in concrete than the model 4151 alternative. ***Number of sensors: 9***

Sisterbar (model 4911, Geokon): These strain sensors are fabricated on a #4 epoxy-coated steel reinforcing bar. The standard stock length is 36 inches. For this link-slab, all the sisterbars had an overall length of 31 inches, with the transducer centered on the sensor. The sisterbar sensors were ordered from Geokon or BDI Inc. already custom cut to this length. One sisterbar is paired with each strandmeter (BFRP gauge) and placed adjacent to it in order to measure strain in the concrete surrounding reinforcement bars. The team followed the BDI suggestion to loosely tying each sisterbar adjacent to its accompanying strandmeter-mounted reinforcement bar with wire using the transverse link-slab reinforcing. ***Number of sensors: 9***

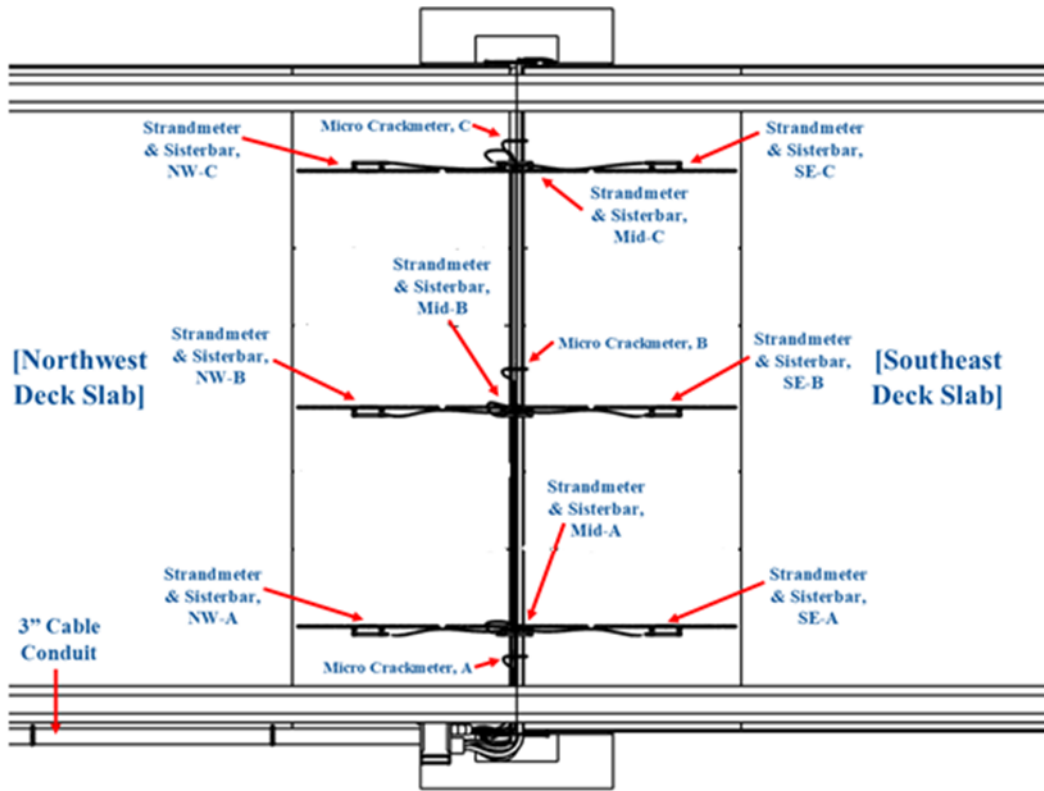


Figure 2.1: Location of embedded sensor array, top view

Figures 2.2 – 2.9 show the sensors installed in the link slab:

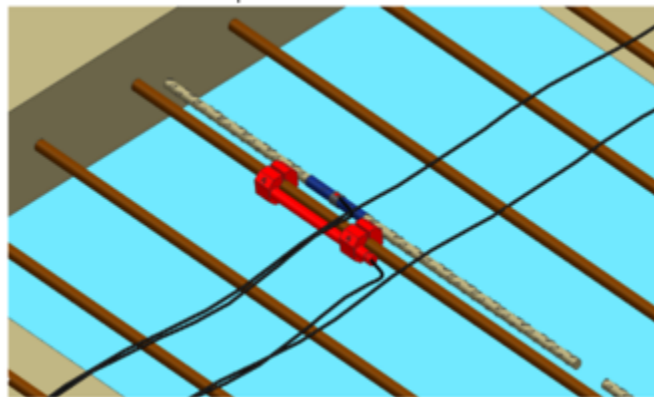


Figure 2.2: Schematic of Strandmeter (Red) and Sisterbar (Green & Blue) placement



Figure 2.3: Link slab reinforcement and embedded sensors



Figure 2.4: Link-slab photos prior to setting reinforcement



Figure 2.5: Finished link slab and close up view



Figure 2.6: Data acquisition modules and wiring



Figure 2.7: Vandalized surface mounted crackmeters

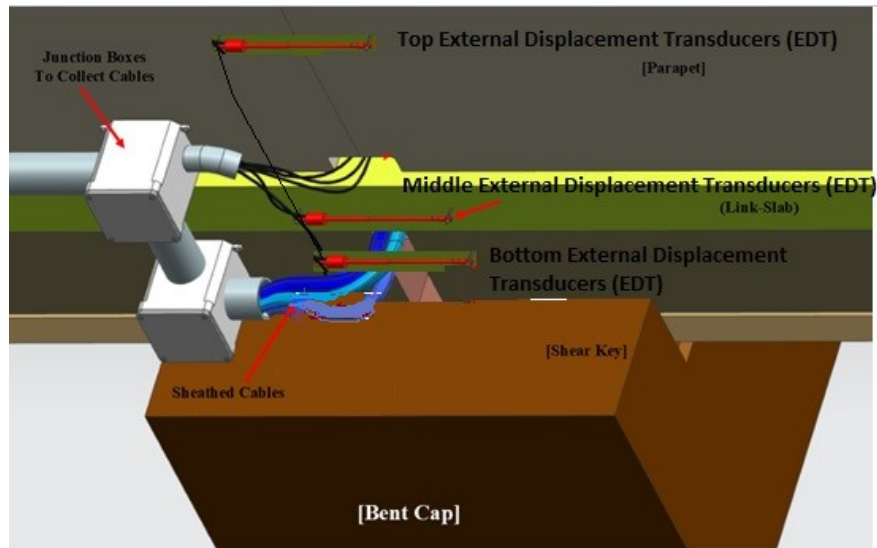


Figure 2.8: Southwest outboard EDTs



Figure 2.9: External displacement transducers

2.1.1 Sensor Wiring and Cables:

Connections between the sensors and data acquisition system is accomplished via a “Vibrating Wire” cable (abbreviated as VW cable). VW cable consists of five conducting elements: 2 twisted wire pairs (red/black & white/green), and a 24AWG stranded copper wire for grounding. A 0.0625-inch diameter blue PVC jacket protects the cable.

All cables were intended to be routed through a PVC conduit pipe from the dataloggers toward the northeast side of the link-slab, however, due to construction delays they are externally mounted on the southwest side of the link-slab. From this point, cables diverged in bundles to their respective sensor locations. Most of these cables partly or fully crossed beneath the transverse midline of the link-slab and do so within channels of the Expanded Poly-Styrene Gap Filler (EPS Gap Filler) between the northwest and southeast FSBs and Deck Slabs. Cables of the 3x3 Embedded Sensor Array were routed along their respective BFRP rebar toward the transverse midline of the link-slab, held close and securely to the rebar with zip-ties. At the midline, these cables exited through the link-slab bottom into channels at the top of the EPS Gap Filler.

Sensors were delivered with pre-attached heavy-duty VW cables. Special care was taken to protect the cables, especially at exit points for embedded sensors’ cables and around sharp edges. Protective containers were provided at exit points with enough room to store cable ends for protection against damage and accidental cutting during concrete casting and curing. High quality cable tags were used at multiple points along each cable in order to positively identify each cable and its associated sensor.

Cables running from the surface mounted Micro Crackmeters (Group #3) were held down with cable clips screwed down onto the link-slab. Unfortunately, these Micro Crackmeters were vandalized and damaged before any useful data could be retrieved.

2.1.2 Cable Routing

All cables were led from the dataloggers at the Southeast side of the link-slab. Three VW cables lead directly to the Outboard EDTs. 18 VW cables lead to the embedded Strandmeters and Sisterbars.

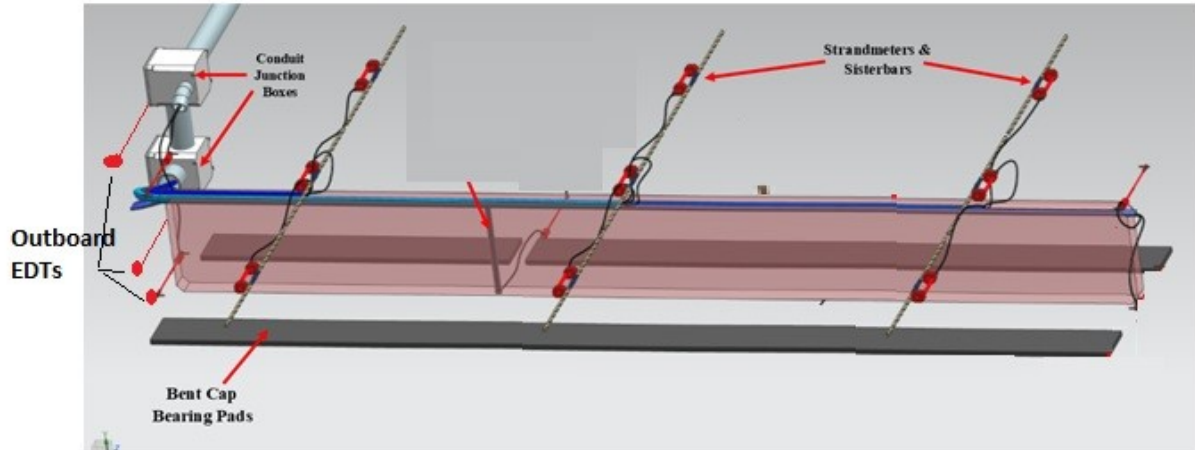


Figure 2.10: Cable routing through EPS

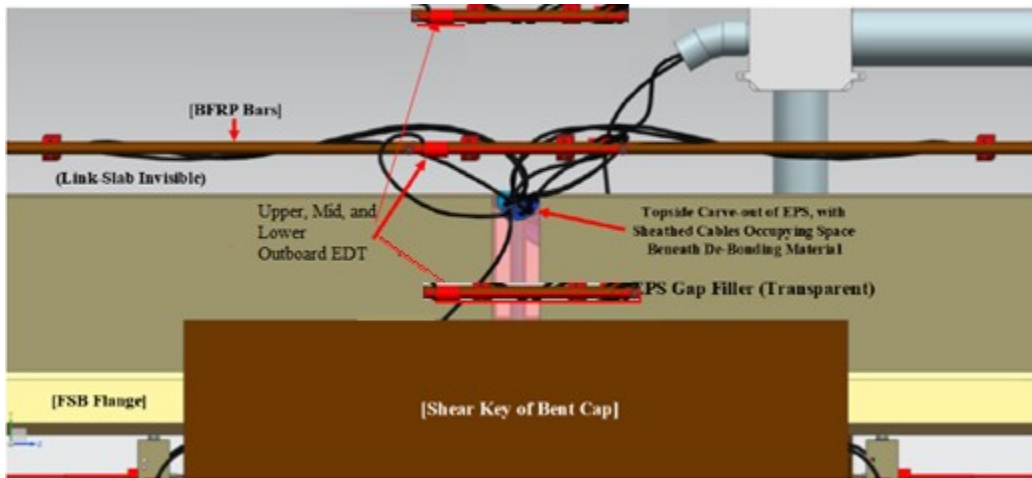


Figure 2.11: Detail of embedded sensor routing, side view

2.2 Data Acquisition

Data acquisition was accomplished by two Geokon brand, model 8002-16-1 dataloggers, also referred to as LC-2x16 datalogger units (also abbreviated as LC-2). Each of these units is capable of monitoring input from up to 16 VW cables for a total of 32 possible inputs, of which only 29 are planned for use. Storage capacity of the dataloggers is 320 KB of EEPROM type memory (data not lost upon de-energizing system), which provides storage for up to 3,555 readings from all 32 possible VW inputs. At an instrument reading rate of once per hour, this

provides a maximum window of 148 days or approximately 5 months to retrieve data before capacity is reached and data points are compromised. Datalogger internal power is supplied by either four alkaline D-cell batteries or a 12-volt external grid supply. Recorded sensor data was accessed by direct retrieval on a periodic basis. Interfacing with the LC-2 units has been accomplished either through an RS-232 Serial Interface or a USB 2.0 port, using LogView software.

The data acquisition system was located on the outboard side of the southwest facing parapet, near the midspan of the bridge. LC-2 Datalogger units were housed inside fiberglass NEMA 4X weatherproof enclosures. For future use and long-term security, three 12"x12" plastic junction boxes are provided for cable bundling and storage when Datalogger units are removed.

Strandmeter (model 4410, Geokon): These sensors measure deformation. *Number of sensors: 9*

Sister Bar (model 4911, Geokon): These sensors measure strain. *Number of sensors: 9*

Table 1: List of Geokon sensors serial numbers

Strandmeter Serial Numbers			
	A	B	C
SE	1947585	1947588	1947591
Mid	1947584	1947587	1947590
NW	1947583	1947586	1947589

Sister Bar Serial Numbers			
	A	B	C
SE	2009690	2009693	2009696
Mid	2009689	2009692	2009695
NW	2009688	2009691	2009694

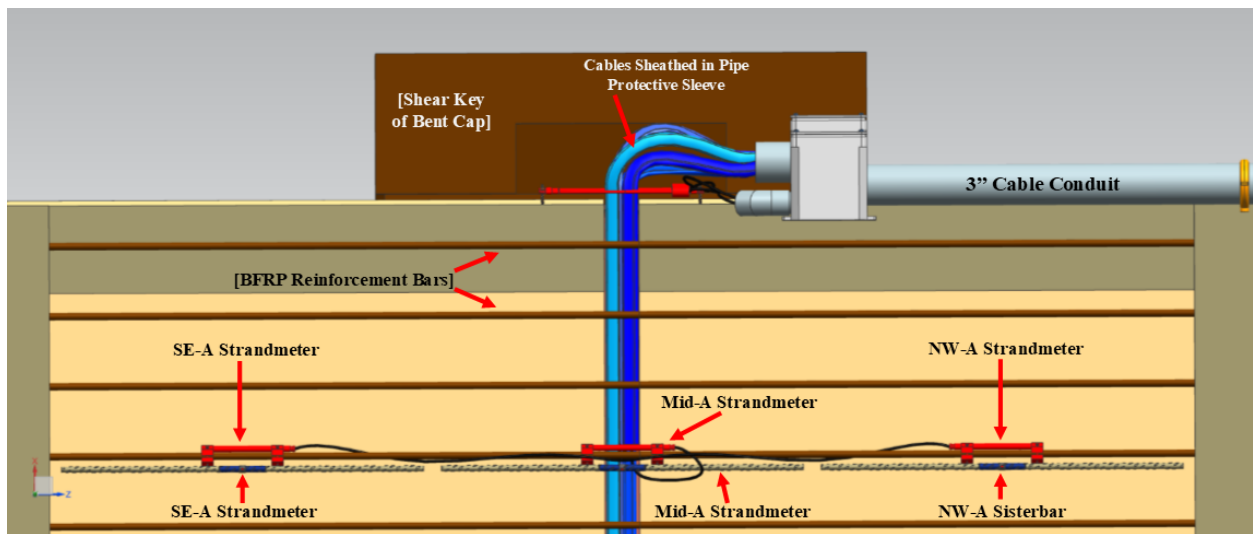


Figure 2.12: Details of embedded sensors and wiring, top view

2.3 Sensor setup

Figure 2.13 is a screen capture from the LogView data acquisition software that show the sensor setup information.

Datalogger No.1 Sensor Setup Info, Channels 1 Through 16:

General sensor information	Units conversion	Temperature correction
Sensor Id: G0307093733 Sensor Name: SE-A-Strand Description: 1947585 Model: 44xx Type: VIBRATING_WIRE Date created: Mar 7 2020	Measurement: default Input units: none Output units: none Conversion method: Linear Output calculation: $G(R1 - R0)$ Zero reading: 9000.794 Gage factor: 3.365E-5 Gage offset: 0.0	Allow temp correction: no Initial temp: 95.7 Temperature factor: 1.0 Convert temp to F: yes Thermistor Type: Standard
Sensor Id: G0307093734 Sensor Name: Mid-A-Strand Description: 1947584 Model: 44xx Type: VIBRATING_WIRE Date created: Mar 7 2020	Measurement: default Input units: none Output units: none Conversion method: Linear Output calculation: $G(R1 - R0)$ Zero reading: 8978.683 Gage factor: 8.484E-4 Gage offset: 0.0	Allow temp correction: no Initial temp: 97.7 Temperature factor: 1.0 Convert temp to F: yes Thermistor Type: Standard
Sensor Id: G0307093735 Sensor Name: NW-A-Strand Description: 1947583 Model: 44xx Type: VIBRATING_WIRE Date created: Mar 7 2020	Measurement: default Input units: none Output units: none Conversion method: Linear Output calculation: $G(R1 - R0)$ Zero reading: 8744.644 Gage factor: 8.465E-4 Gage offset: 0.0	Allow temp correction: no Initial temp: 97.2 Temperature factor: 1.0 Convert temp to F: yes Thermistor Type: Standard
Sensor Id: G0307093736 Sensor Name: SE-B-Strand Description: 1947588 Model: 44xx Type: VIBRATING_WIRE Date created: Mar 7 2020	Measurement: default Input units: none Output units: none Conversion method: Linear Output calculation: $G(R1 - R0)$ Zero reading: 8805.653 Gage factor: 8.238E-4 Gage offset: 0.0	Allow temp correction: no Initial temp: 92.1 Temperature factor: 1.0 Convert temp to F: yes Thermistor Type: Standard

<p>General sensor information</p> <p>Sensor Id: G0307093737 Sensor Name: Mid-B-Strand Description: 1947587 Model: 44xx Type: VIBRATING_WIRE Date created: Mar 7 2020</p>	<p>Units conversion</p> <p>Measurement: default Input units: none Output units: none Conversion method: Linear Output calculation: $G(R1 - R0)$ Zero reading: 8811.292 Gage factor: 8.508E-4 Gage offset: 0.0</p>	<p>Temperature correction</p> <p>Allow temp correction: no Initial temp: 90.1 Temperature factor: 1.0 Convert temp to F: yes Thermistor Type: Standard</p>
<p>General sensor information</p> <p>Sensor Id: G0307093738 Sensor Name: NW-B-Strand Description: 1947586 Model: 44xx Type: VIBRATING_WIRE Date created: Mar 7 2020</p>	<p>Units conversion</p> <p>Measurement: default Input units: none Output units: none Conversion method: Linear Output calculation: $G(R1 - R0)$ Zero reading: 8892.411 Gage factor: 8.495E-4 Gage offset: 0.0</p>	<p>Temperature correction</p> <p>Allow temp correction: no Initial temp: 91.8 Temperature factor: 1.0 Convert temp to F: yes Thermistor Type: Standard</p>
<p>General sensor information</p> <p>Sensor Id: G0307093739 Sensor Name: SE-C-Strand Description: 1947591 Model: 44xx Type: VIBRATING_WIRE Date created: Mar 7 2020</p>	<p>Units conversion</p> <p>Measurement: default Input units: none Output units: none Conversion method: Linear Output calculation: $G(R1 - R0)$ Zero reading: 8850.494 Gage factor: 8.508E-4 Gage offset: 0.0</p>	<p>Temperature correction</p> <p>Allow temp correction: no Initial temp: 93.7 Temperature factor: 1.0 Convert temp to F: yes Thermistor Type: Standard</p>
<p>General sensor information</p> <p>Sensor Id: G0307093740 Sensor Name: Mid-C-Strand Description: 1947589 Model: 44xx Type: VIBRATING_WIRE Date created: Mar 7 2020</p>	<p>Units conversion</p> <p>Measurement: default Input units: none Output units: none Conversion method: Linear Output calculation: $G(R1 - R0)$ Zero reading: 8780.526 Gage factor: 8.501E-4 Gage offset: 0.0</p>	<p>Temperature correction</p> <p>Allow temp correction: no Initial temp: 93.2 Temperature factor: 1.0 Convert temp to F: yes Thermistor Type: Standard</p>
<p>General sensor information</p> <p>Sensor Id: G0307093741 Sensor Name: SE-A-Sis Description: 2009690 Model: 49xx Type: VIBRATING_WIRE Date created: Mar 7 2020</p>	<p>Units conversion</p> <p>Measurement: default Input units: none Output units: none Conversion method: Linear Output calculation: $G(R1 - R0)$ Zero reading: 7997.503 Gage factor: 0.355 Gage offset: 0.0</p>	<p>Temperature correction</p> <p>Allow temp correction: no Initial temp: 98.1 Temperature factor: 1.0 Convert temp to F: yes Thermistor Type: Standard</p>

<p>General sensor information</p> <p>Sensor Id: G0307093742 Sensor Name: Mid-A-Sis Description: 2009689 Model: 49xx Type: VIBRATING_WIRE Date created: Mar 7 2020</p>	<p>Units conversion</p> <p>Measurement: default Input units: none Output units: none</p> <p>Conversion method: Linear</p> <p>Output calculation: $G(R1 - R0)$ Zero reading: 8124.18 Gage factor: 0.353 Gage offset: 0.0</p>	<p>Temperature correction</p> <p>Allow temp correction: no Initial temp: 99.1 Temperature factor: 1.0 Convert temp to F: yes Thermistor Type: Standard</p>
<p>General sensor information</p> <p>Sensor Id: G0307093743 Sensor Name: NW-A-Sis Description: 2009688 Model: 49xx Type: VIBRATING_WIRE Date created: Mar 7 2020</p>	<p>Units conversion</p> <p>Measurement: default Input units: none Output units: none</p> <p>Conversion method: Linear</p> <p>Output calculation: $G(R1 - R0)$ Zero reading: 7621.272 Gage factor: 0.353 Gage offset: 0.0</p>	<p>Temperature correction</p> <p>Allow temp correction: no Initial temp: 104.5 Temperature factor: 1.0 Convert temp to F: yes Thermistor Type: Standard</p>
<p>General sensor information</p> <p>Sensor Id: G0307093744 Sensor Name: SE-B-Sis Description: 2009693 Model: 49xx Type: VIBRATING_WIRE Date created: Mar 7 2020</p>	<p>Units conversion</p> <p>Measurement: default Input units: none Output units: none</p> <p>Conversion method: Linear</p> <p>Output calculation: $G(R1 - R0)$ Zero reading: 7833.814 Gage factor: 0.354 Gage offset: 0.0</p>	<p>Temperature correction</p> <p>Allow temp correction: no Initial temp: 93.9 Temperature factor: 1.0 Convert temp to F: yes Thermistor Type: Standard</p>
<p>General sensor information</p> <p>Sensor Id: G0307093745 Sensor Name: Mid-B-Sis Description: 2009692 Model: 49xx Type: VIBRATING_WIRE Date created: Mar 7 2020</p>	<p>Units conversion</p> <p>Measurement: default Input units: none Output units: none</p> <p>Conversion method: Linear</p> <p>Output calculation: $G(R1 - R0)$ Zero reading: 7879.003 Gage factor: 0.353 Gage offset: 0.0</p>	<p>Temperature correction</p> <p>Allow temp correction: no Initial temp: 100.8 Temperature factor: 1.0 Convert temp to F: yes Thermistor Type: Standard</p>
<p>General sensor information</p> <p>Sensor Id: G0307093746 Sensor Name: NW-B-Sis Description: 2009691 Model: 49xx Type: VIBRATING_WIRE Date created: Mar 7 2020</p>	<p>Units conversion</p> <p>Measurement: default Input units: none Output units: none</p> <p>Conversion method: Linear</p> <p>Output calculation: $G(R1 - R0)$ Zero reading: 7521.281 Gage factor: 0.354 Gage offset: 0.0</p>	<p>Temperature correction</p> <p>Allow temp correction: no Initial temp: 93.9 Temperature factor: 1.0 Convert temp to F: yes Thermistor Type: Standard</p>

<p>General sensor information</p> <p>Sensor Id: G0307093747 Sensor Name: SE-C-Sis Description: 2009696 Model: 49xx Type: VIBRATING_WIRE Date created: Mar 7 2020</p>	<p>Units conversion</p> <p>Measurement: default Input units: none Output units: none</p> <p>Conversion method: Linear</p> <p>Output calculation: $G(R1 - R0)$ Zero reading: 7639.152 Gage factor: 0.356 Gage offset: 0.0</p>	<p>Temperature correction</p> <p>Allow temp correction: no Initial temp: 86.5 Temperature factor: 1.0 Convert temp to F: yes Thermistor Type: Standard</p>
<p>General sensor information</p> <p>Sensor Id: G0307093748 Sensor Name: Mid-C-Sis Description: 2009695 Model: 49xx Type: VIBRATING_WIRE Date created: Mar 7 2020</p>	<p>Units conversion</p> <p>Measurement: default Input units: none Output units: none</p> <p>Conversion method: Linear</p> <p>Output calculation: $G(R1 - R0)$ Zero reading: 8050.535 Gage factor: 0.356 Gage offset: 0.0</p>	<p>Temperature correction</p> <p>Allow temp correction: no Initial temp: 85.5 Temperature factor: 1.0 Convert temp to F: yes Thermistor Type: Standard</p>

Datalogger No.2 Setup Info, Channels 1 & 2:

Note: The temperature was not converted to Fahrenheit

<p>General sensor information</p> <p>Sensor Id: G0307094734 Sensor Name: NW-C-Strand Description: 1947590 Model: 44xx Type: VIBRATING_WIRE Date created: Mar 7 2020</p>	<p>Units conversion</p> <p>Measurement: default Input units: none Output units: none</p> <p>Conversion method: Linear</p> <p>Output calculation: $G(R1 - R0)$ Zero reading: 8570.04 Gage factor: $8.0E-4$ Gage offset: 0.0</p>	<p>Temperature correction</p> <p>Allow temp correction: no Initial temp: 29.3 Temperature factor: 1.0 Convert temp to F: no Thermistor Type: Standard</p>
<p>General sensor information</p> <p>Sensor Id: G0307094735 Sensor Name: NW-C-Sis Description: 2009694 Model: 49xx Type: VIBRATING_WIRE Date created: Mar 7 2020</p>	<p>Units conversion</p> <p>Measurement: default Input units: none Output units: none</p> <p>Conversion method: Linear</p> <p>Output calculation: $G(R1 - R0)$ Zero reading: 8177.211 Gage factor: 0.353 Gage offset: 0.0</p>	<p>Temperature correction</p> <p>Allow temp correction: no Initial temp: 29.8 Temperature factor: 1.0 Convert temp to F: no Thermistor Type: Standard</p>

Figure 2.13: Sensor setup in LogView software

3 Data Reduction

3.1 Data reduction for Strandmeters

The data outputted from the LC2 dataloggers for the strandmeters was in millimeters of deformation. This is obtained through the equation:

$$Deformation = (Current\ Reading - Initial\ Reading) * (Calibration\ Factor)$$

$$D = (R_1 - R_0) * G$$

The initial reading and calibration factor were inputted into the datalogger and used to calculate the output. To correct for the effects of temperature on the material, the following equation is used:

$$D_{Corrected} = [(R_1 - R_0) * G] + [(T_1 - T_0) * K]$$

Where K is the thermal coefficient of the transducer and can be found using:

$$K = [(R_1 * 0.00520) + 3.567] * G$$

Once the deformation was corrected for temperature effects, it was then used to calculate the strain based off the deformation using:

$$\mu = \left(\frac{D}{203.2} \right) * 10^6$$

This outputs the strain as microstrain.

3.2 Data reduction for Sisterbars

The data outputted from the LC2 dataloggers for the sister bars is in apparent (micro) strain. This is obtained through the equation:

$$\textit{Apparent Strain} = (\textit{Current Reading} - \textit{Intial Reading}) * (\textit{Calibration Factor})$$

$$\varepsilon_{\textit{apparent}} = (R_1 - R_0) * C$$

The initial reading and calibration factor were inputted into the datalogger and used to calculate the output. From the apparent strain, the temperature corrected load related strain and actual strain can be found.

$$\varepsilon_{\textit{load related}} = [(R_1 - R_0) * C] + [(T_1 - T_0) * K_{\textit{diff}}]$$

$$\varepsilon_{\textit{actual}} = [(R_1 - R_0) * C] + [(T_1 - T_0) * K_{\textit{steel}}]$$

Where K_{diff} is the difference between the coefficients of thermal expansion for steel and concrete.

4 Results and Data Analysis

4.1 Amendments to the dataset

The strandmeters and sister bars were installed before the link slab was cast. This left the sensors exposed directly to thermal effects. To see the deformation and strain in the concrete after it was poured, the data was zeroed and shifted to start at hour 92.

4.2 Graphs of reduced data

Figures 4.1 – 4.4 show graphs of the recorded data. Average daily strain at the Mid sensors appears constant from 90+ days, as shown in figures 4.1 – 4.4. As shown in Figure 4.4, there have been some outliers or daily strain changes and maximum differential recorded on the site from Sisterbars and BFRP bars. That could be due to any interference with the system electronics or other electronics systems in the close vicinity of the sensors or due to glitches caused sometimes by the data acquisition system that could cause spikes.

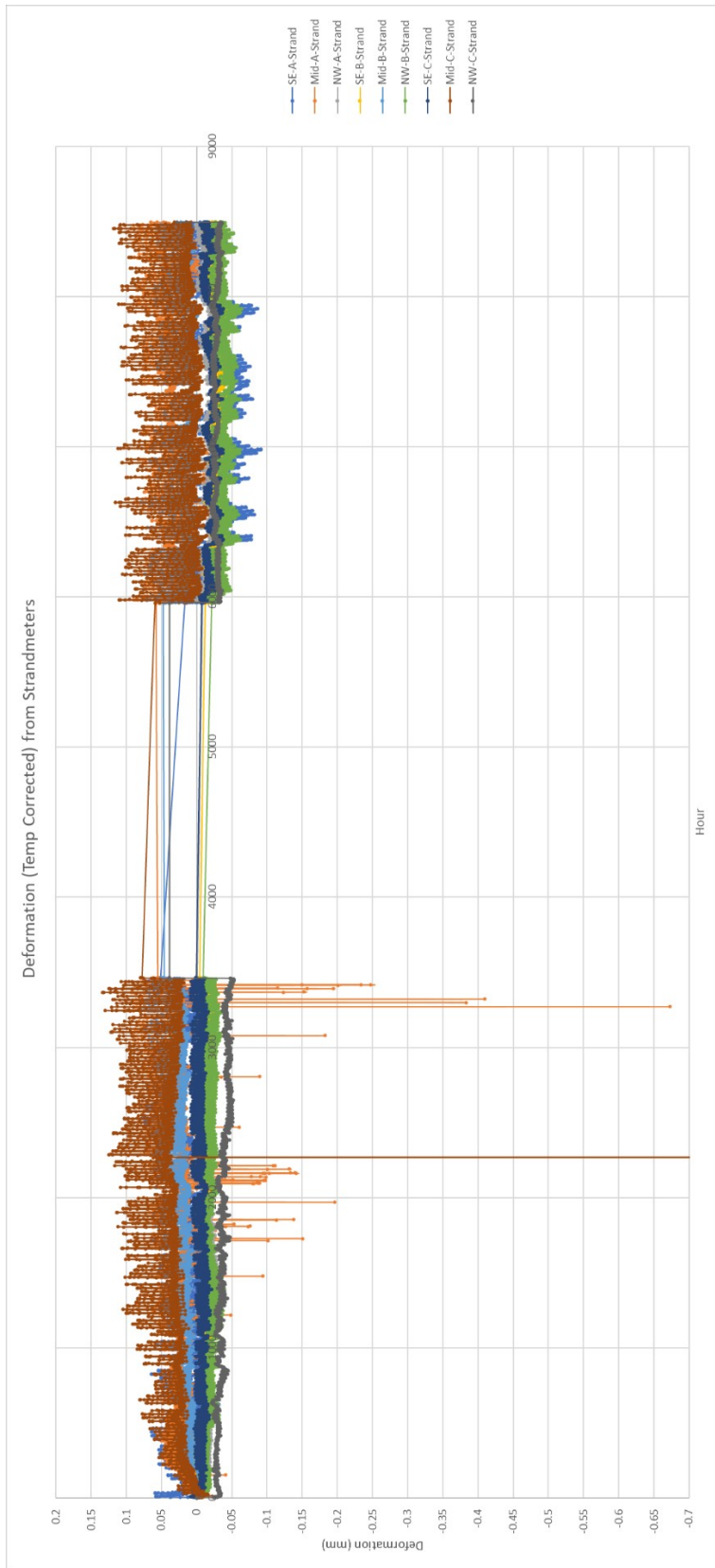


Figure 4.1: Graphed deformation from Strandmeters

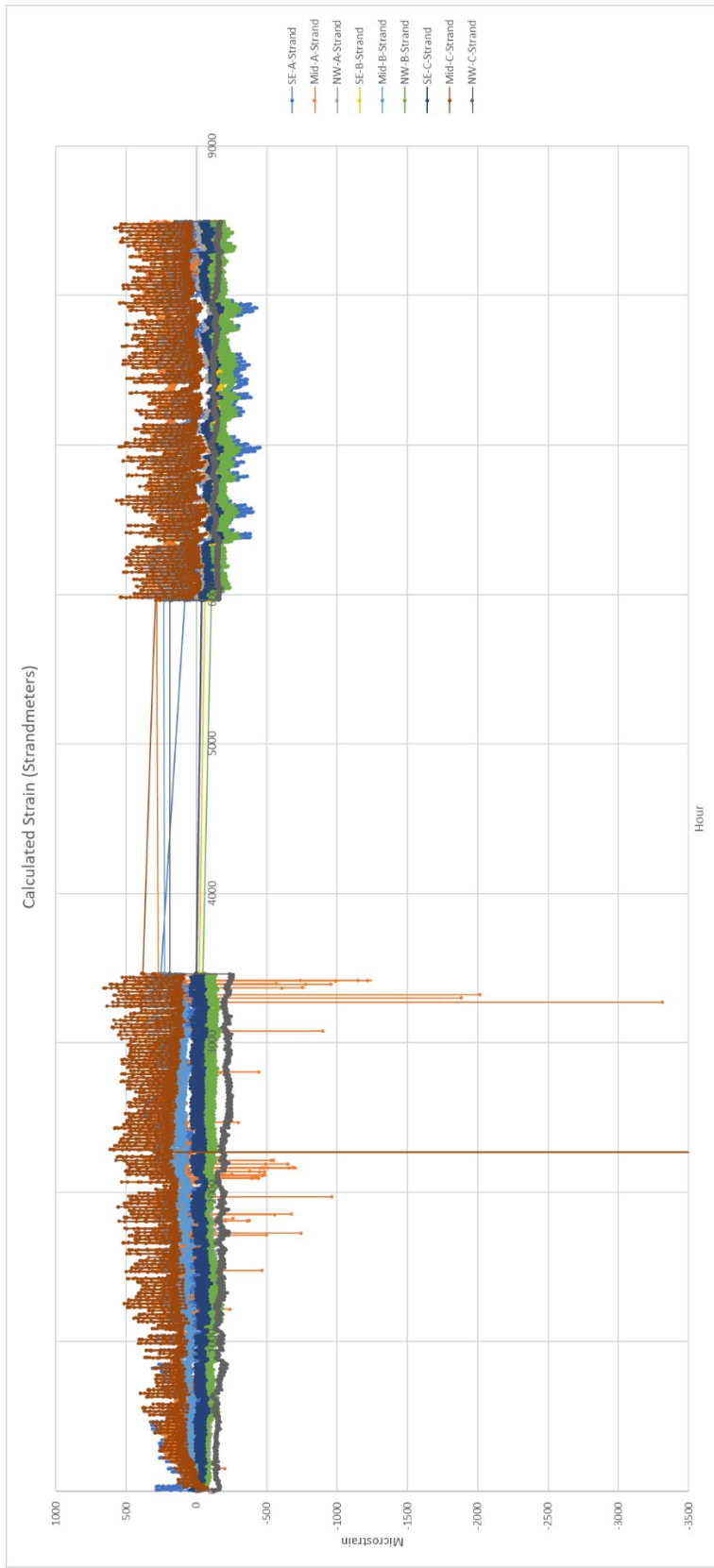


Figure 4.2: Graphed strain from Strandmeters

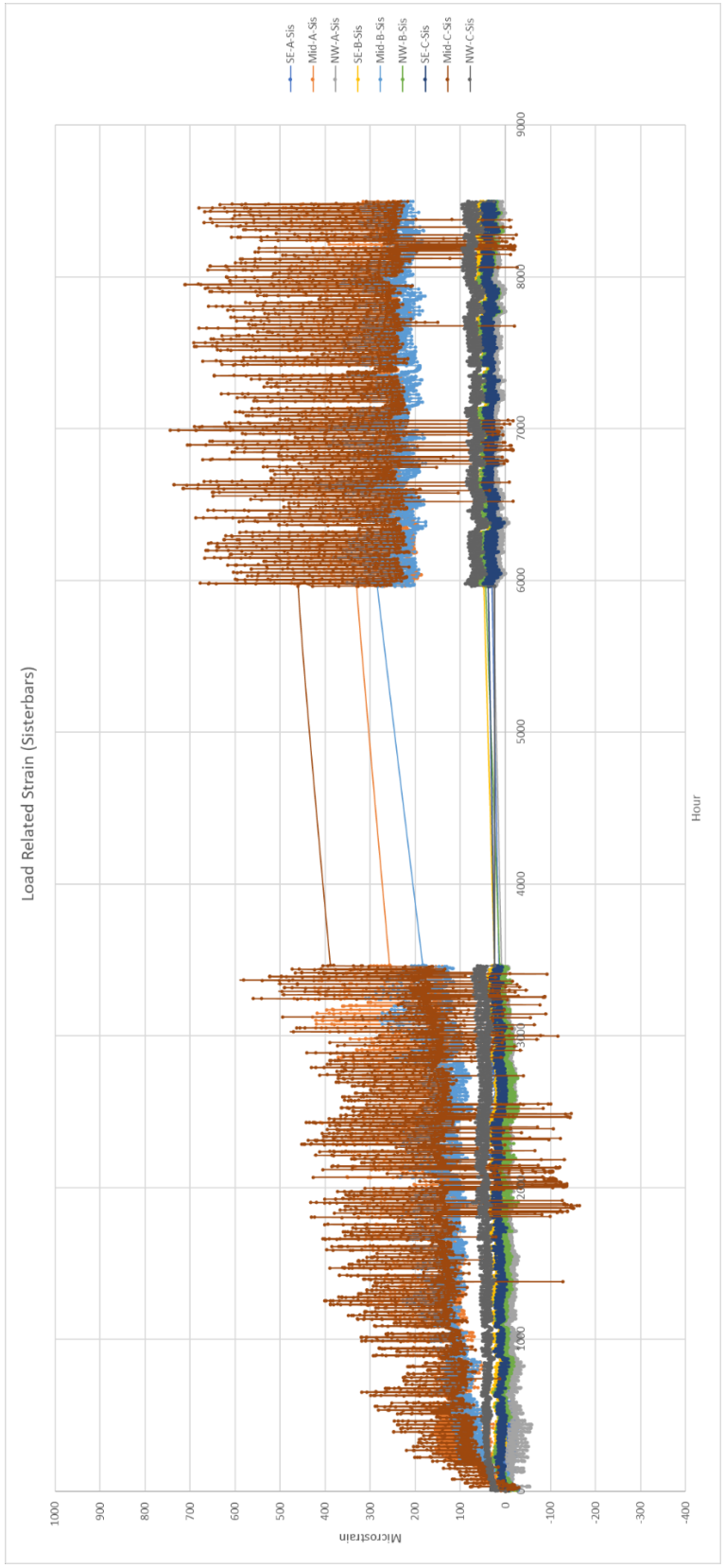


Figure 4.3: Graphed load related strain from Sisterbars

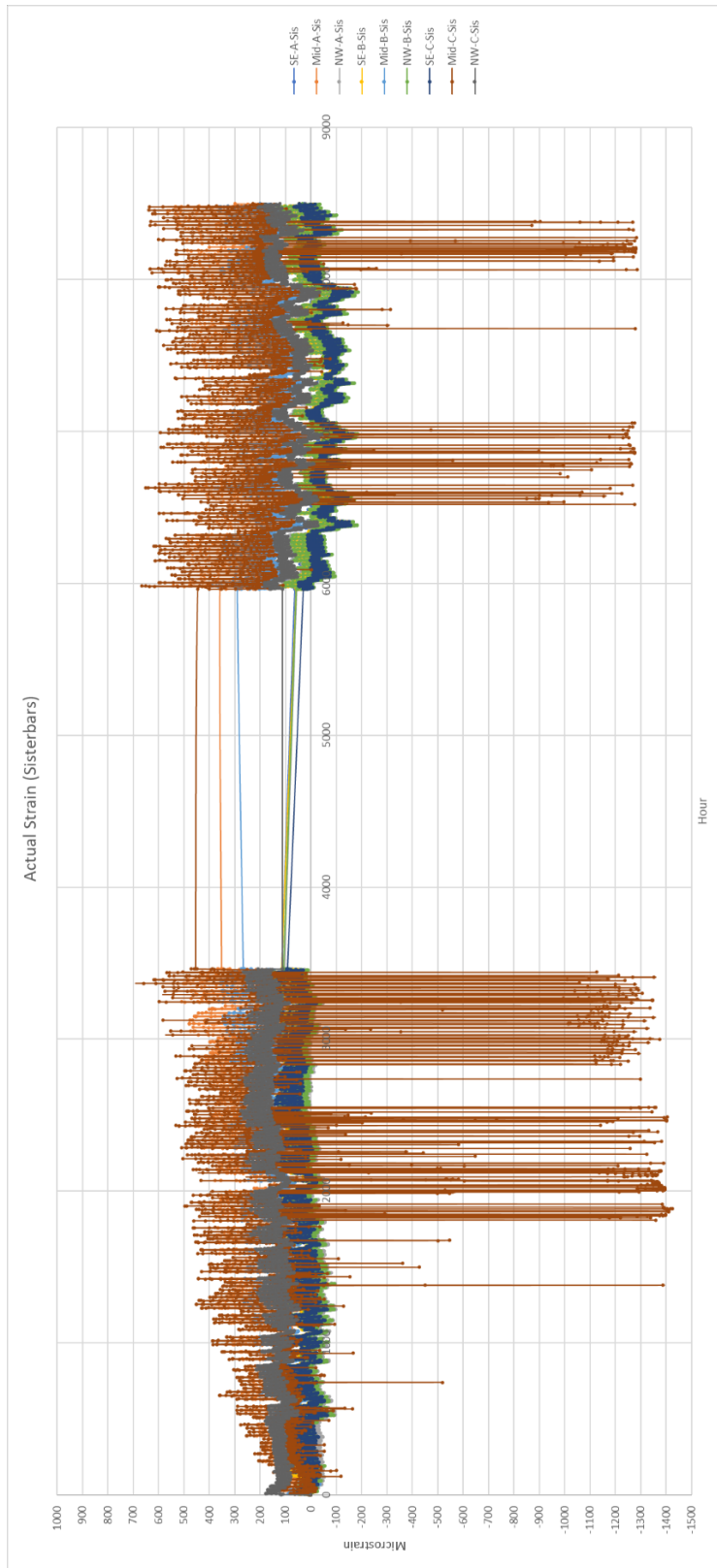


Figure 4.4: Graphed actual strain from Sisterbars

4.3 Samples of reduced data

Tables 2 – 5 show the first 20 reduced data points (hours).

Table 2: First 20 data points of Strandmeter deformation

1947585	1947584	1947583	1947588	1947587	1947586	1947591	1947590	1947589
Deformation (Temp corrected) - SE-A-Strand	Deformation (Temp corrected) - Mid-A-Strand	Deformation (Temp corrected) - NW-A-Strand	Deformation (Temp corrected) - SE-B-Strand	Deformation (Temp corrected) - Mid-B-Strand	Deformation (Temp corrected) - NW-B-Strand	Deformation (Temp corrected) - SE-C-Strand	Deformation (Temp corrected) - Mid-C-Strand	Deformation (Temp corrected) - NW-C-Strand
0	0	0	0	0	0	0.001	0.002	0.001
-0.02369748	-0.012723064	-0.005571296	-0.005157161	-0.003387939	-0.007150382	-0.011651521	-0.00277011	0.001
-0.045870424	-0.021867122	-0.005821181	-0.006081978	-0.007024604	-0.009361547	-0.014825541	-0.001136189	0.000303231
-0.078800397	-0.031089908	-0.009846981	-0.014642322	-0.015462199	-0.016420979	-0.02195966	-0.003906299	0.010322311
-0.097009548	-0.034668359	-0.01126572	-0.017330236	-0.019581462	-0.021389912	-0.025471965	-0.005382874	0.026954466
-0.106766578	-0.035233966	-0.013531903	-0.019733419	-0.021596313	-0.024692478	-0.028576377	-0.006657433	0.028973546
-0.112254906	-0.035681203	-0.014966941	-0.021022709	-0.02336244	-0.025752811	-0.029645985	-0.007840473	0.034179855
-0.118572678	-0.036944186	-0.016005872	-0.023368945	-0.02525293	-0.02902521	-0.032232995	-0.009569272	0.035721702
-0.123451193	-0.037575677	-0.016837017	-0.024364386	-0.027501655	-0.030267444	-0.034392162	-0.011824856	0.038386164
-0.127719893	-0.040628163	-0.018064268	-0.025478279	-0.02775038	-0.031509677	-0.035640887	-0.012152984	0.039747396
-0.13015915	-0.03983866	-0.018781787	-0.026122924	-0.029088664	-0.032236827	-0.035979172	-0.011935351	0.041018319
-0.132903315	-0.03895703	-0.01919736	-0.026592171	-0.028909546	-0.03366096	-0.035496574	-0.011481111	0.041592474
-0.135037665	-0.0390754	-0.019310985	-0.027236816	-0.029033908	-0.033782076	-0.036620937	-0.013263479	0.04407632
-0.135037665	-0.0390754	-0.019914879	-0.026942967	-0.029033908	-0.034176043	-0.036317456	-0.012954327	0.043863397
-0.134427851	-0.0390754	-0.019310985	-0.026767569	-0.028819987	-0.03357001	-0.035710495	-0.011717719	0.045650474
-0.135952386	-0.039285897	-0.018820718	-0.026824515	-0.028640869	-0.03538811	-0.036227897	-0.012263479	0.045650474
-0.133208222	-0.038864903	-0.018103199	-0.025298322	-0.026695624	-0.034054926	-0.033889613	-0.011171959	0.044953705
-0.1194874	-0.031733689	-0.011609765	-0.01743501	-0.019631117	-0.024631694	-0.025466867	-0.001439801	0.046347244
-0.099753713	-0.026102752	-0.003301484	-0.013405419	-0.015337836	-0.01496668	-0.02054667	0.003330309	0.046863397
-0.06468939	-0.020485214	-0.003012669	-0.010015914	-0.015273329	-0.013634398	-0.016964757	-0.002029052	0.045992626

Table 3: First 20 data points of Strandmeter microstrain

1947585	1947584	1947583	1947588	1947587	1947586	1947591	1947590	1947589
Strain (micro) - SE-A-Strand	Strain (micro) - Mid-A-Strand	Strain (micro) - NW-A-Strand	Strain (micro) - SE-B-Strand	Strain (micro) - Mid-B-Strand	Strain (micro) - NW-B-Strand	Strain (micro) - SE-C-Strand	Strain (micro) - Mid-C-Strand	Strain (micro) - NW-C-Strand
0	0	0	0	0	0	4.921259843	9.842519685	4.921259843
-116.6214565	-62.61350295	-27.41779724	-25.37972992	-16.67293031	-35.18888755	-57.34016156	-13.63243058	4.921259843
-225.7402762	-107.6137886	-28.64754306	-29.93099498	-34.56990118	-46.07060753	-72.96033977	-5.591481791	1.492277137
-387.7972313	-153.0015171	-48.45954995	-72.05867136	-76.09349823	-80.81190625	-108.0691922	-19.22391237	50.79877322
-477.4091953	-170.6120045	-55.44153593	-85.2865937	-96.36546024	-105.2653137	-125.354156	-26.49052039	132.6499297
-525.4260709	-173.3955035	-66.59400984	-97.11328031	-106.2810699	-121.5180997	-140.6317748	-32.7629584	142.5863471
-552.4355634	-175.5964732	-73.65620423	-103.4582128	-114.972639	-126.7362739	-145.8955941	-38.58500369	168.2079479
-583.5269602	-181.8119394	-78.76905364	-115.0046523	-124.2762283	-142.8406026	-158.626943	-47.09287526	175.7957783
-607.535398	-184.9196724	-82.85933317	-119.9034752	-135.3427886	-148.9539545	-169.2527643	-58.19318856	188.9082889
-628.5427811	-199.9417472	-88.89895768	-125.3852293	-136.5668291	-155.0673063	-175.3980677	-59.80799034	195.6072625
-640.547	-196.0563984	-92.43005487	-128.5576956	-143.1528722	-158.6457997	-177.0628534	-58.73696584	201.8618076
-654.0517463	-191.7176679	-94.47519464	-130.8669835	-142.2713868	-165.6543292	-174.6878633	-56.50153228	204.68737
-664.5554378	-192.3001972	-95.03437697	-134.0394497	-142.8834071	-166.2503752	-180.2211449	-65.27302746	216.9110237
-664.5554378	-192.3001972	-98.00629183	-132.5933402	-142.8834071	-168.1891877	-178.727639	-63.75161024	215.863175
-661.5543831	-192.3001972	-95.03437697	-131.7301618	-141.8306441	-165.2067404	-175.7406272	-57.66594134	224.657846
-669.0570199	-193.3361083	-92.62164444	-132.010409	-140.9491587	-174.1540824	-178.286897	-60.35176762	224.657846
-655.5522736	-191.2642862	-89.09054724	-124.4996141	-131.3761041	-167.5931417	-166.7795916	-54.98011506	221.2288633
-588.0285423	-156.1697291	-57.13466929	-85.80221417	-96.60982776	-121.218968	-125.3290706	-7.085634687	228.0868287
-490.9139415	-128.4584268	-16.24746038	-65.97154911	-75.48147795	-73.65491954	-101.1155017	16.38931558	230.6269545
-318.3532949	-100.8130632	-14.826125	-49.29091339	-75.16402047	-67.09841339	-83.4879784	-9.985494411	226.3416621

Table 4: First 20 data points of load related microstrain from Sisterbars

2009690	2009689	2009688	2009693	2009692	2009691	2009696	2009695	2009694
Load Related Strain (micro) - SE-A-Sis	Load Related Strain (micro) - Mid-A-Sis	Load Related Strain (micro) - NW-A-Sis	Load Related Strain (micro) - SE-B-Sis	Load Related Strain (micro) - Mid-B-Sis	Load Related Strain (micro) - NW-B-Sis	Load Related Strain (micro) - SE-C-Sis	Load Related Strain (micro) - Mid-C-Sis	Load Related Strain (micro) - NW-C-Sis
-0.119	0.168	0.099	0.01	0.494	-0.538	0.335	-0.098	0.28
-12.204	-13.313	-16.388	-11.471	-14.262	-14.519	-7.989	-12.149	1.076
-21.323	-22.407	-27.207	-18.658	-23.937	-23.639	-13.769	-14.558	0.65
-38.872	-40.961	-47.931	-34.357	-43.759	-37.144	-27.668	-26.971	-10.909
-47.267	-49.169	-55.961	-42.872	-51.814	-45.189	-35.685	-34.919	-16.298
-51.149	-53.505	-60.527	-46.555	-56.338	-49.749	-39.723	-38.71	-24.714
-54.004	-56.081	-63.185	-48.927	-58.797	-52.426	-42.276	-41.775	-31.836
-57.379	-59.102	-65.935	-52.577	-62.355	-55.776	-46.163	-44.865	-36.437
-59.2	-61.199	-68.234	-54.987	-64.707	-58.097	-48.033	-47.533	-38.889
-61.47	-63.427	-69.985	-56.735	-66.485	-59.711	-50.037	-49.071	-42.248
-62.685	-64.136	-71.056	-58.085	-67.657	-61.075	-51.536	-50.327	-44.737
-63.551	-65.425	-71.877	-59.097	-68.236	-61.844	-52.391	-51.287	-46.928
-64.448	-65.947	-73.06	-60.117	-69.458	-62.92	-53.135	-52.356	-48.011
-64.428	-66.093	-72.803	-59.635	-68.824	-62.598	-52.82	-52.053	-48.976
-63.781	-65.618	-72.553	-59.11	-68.43	-61.813	-52.445	-51.58	-49.824
-64.913	-66.578	-73.447	-60.152	-69.24	-62.866	-53.45	-52.558	-49.924
-62.805	-64.283	-71.361	-57.691	-66.757	-60.419	-50.903	-50.548	-49.494
-56.038	-56.911	-64.203	-47.684	-57.114	-49.166	-38.801	-38.227	-50.238
-46.007	-43.553	-47.919	-33.119	-40.233	-31.767	-25.167	-24.313	-48.126
-30.333	-29.074	-35.393	-24.246	-30.061	-22.301	-16.988	-16.404	-36.634

Table 5: First 20 data points of actual microstrain from Sisterbars

2009690	2009689	2009688	2009693	2009692	2009691	2009696	2009695	2009694
Actual Strain (micro) - SE-A-Sis	Actual Strain (micro) - Mid-A-Sis	Actual Strain (micro) - NW-A-Sis	Actual Strain (micro) - SE-B-Sis	Actual Strain (micro) - Mid-B-Sis	Actual Strain (micro) - NW-B-Sis	Actual Strain (micro) - SE-C-Sis	Actual Strain (micro) - Mid-C-Sis	Actual Strain (micro) - NW-C-Sis
-0.119	0.168	0.099	0.01	0.494	-0.538	0.335	-0.098	0.28
-57.854	-63.913	-81.838	-56.021	-72.562	-68.969	-37.689	-52.849	3.076
-111.523	-117.557	-145.457	-98.958	-127.887	-117.689	-70.419	-70.108	3.65
-198.372	-211.461	-249.231	-179.007	-226.909	-184.544	-136.018	-129.821	-44.909
-241.417	-254.319	-289.711	-222.172	-267.414	-223.939	-175.385	-166.919	-76.298
-261.249	-275.705	-312.427	-241.255	-290.088	-246.649	-195.373	-187.21	-116.714
-275.104	-288.181	-325.535	-253.527	-302.447	-259.226	-207.826	-201.275	-151.836
-291.129	-302.752	-339.285	-271.477	-319.755	-275.226	-226.563	-216.465	-173.437
-300.65	-313.649	-350.384	-282.687	-330.907	-286.347	-236.133	-229.033	-185.889
-312.27	-324.127	-359.285	-291.035	-339.835	-294.011	-246.387	-237.171	-201.248
-318.435	-328.686	-365.306	-298.435	-347.057	-301.425	-253.936	-243.377	-213.737
-323.151	-333.825	-368.877	-303.297	-349.286	-304.944	-258.641	-248.187	-222.928
-327.898	-338.197	-375.01	-308.717	-355.458	-310.42	-262.135	-253.656	-229.011
-327.878	-338.343	-374.203	-307.135	-353.174	-308.998	-260.72	-252.253	-233.976
-325.031	-336.218	-372.853	-304.41	-350.58	-306.013	-258.695	-250.68	-238.824
-330.563	-341.028	-377.597	-309.302	-355.24	-310.916	-263.55	-254.408	-238.924
-321.305	-331.033	-368.361	-298.041	-343.957	-299.669	-252.203	-245.798	-237.494
-290.888	-296.711	-334.803	-250.634	-298.564	-247.166	-195.551	-190.027	-241.238
-242.357	-233.853	-256.919	-177.769	-217.333	-164.317	-130.217	-122.213	-232.126
-162.883	-156.124	-189.943	-129.296	-159.861	-114.151	-87.388	-79.104	-177.634

4.4 Results and Analysis

The data show that the middle sensors experienced the highest amount of strain and deformation as expected. The max strain calculated from the Strandmeters is ~600 microstrain from the mid-a sensor. The max strain calculated from the Sisterbars is ~700 microstrain from the mid-c sensor.

5 Evaluation of FDOT Link-Slab Details

The research team conducted an evaluation of the link-slab design detail for FBS pedestrian bridge that is reinforced with Basalt Fiber Reinforced Polymer (BFRP) bars. The link-slab details are shown in Appendix E. The details of the link-slab for Bridge No. 019003 are presented in Figures E1 to E6 in Appendix E. The UHPC link-slab (Bridge 019004) was not reviewed as part of this project; yet some details of the UHPC link-slab are also shown in Appendix E.

The link-slab for Bridge No. 019003 is reinforced with longitudinal BFRP #5 bars spaced at 6 inch. The link-slab thickness of 6 inch (minimum) has a 2-inch concrete cover to the top surface of link-slab. The link-slab length is 8 ft – 2 inch, spanning over an open joint between the ends of the FSB beams. A construction joint is introduced at the location of the link-slab and the link-slab is debonded using roofing paper (or any other debonding material) from the supporting FSB beams for a debonding zone length of 5-1/2 ft. The deck thickness usually varies due to beam camber. The volume between the FSB beams (pockets and side face) and the debonding material shall be filled with Class II bridge deck concrete with SRA. The volume above the debonding material shall be filled with Class IV fiber-reinforced concrete.

The link-slab performed very well without showing any excessive cracking. The strains developed in the BFRP reinforcement and recorded by the sensors indicated small strain levels of about 600 microstrain compared to the BFRP ultimate strain values. After about 90 days over the time of monitoring, the average strain in the mid-joint gauges did not change significantly indicating minimal creep and/or shrinkage restraint was experienced to date by the link-slab since the initial casting date. The maximum daily strain change due to thermal effects is about 500 microstrain. In summary, the link-slab showed good performance. Further investigation should be conducted to monitor the long-term performance and live-load test effect using loading trucks. It is also recommended that the UHPC link slab to be investigated in future research projects.

6 Summary

The team investigated the concrete simple-span beams that are made continuous by pouring a continuity link-slab between the beam ends. The bridge has been instrumented with embedded and surface-mounted sensors and has been monitored to evaluate the performance of the new link-slab. No data is available from the initial installation of the surface mounted micro-crack meters A, B & C on the walking surface, as they were vandalized shortly after installation. If these sensors are to be re-installed in a later project, they should be put in a place that cannot be easily accessed by pedestrians.

Several types of sensors were used, and a data acquisition system recorded strains/deformations at a regular time interval. The preferred sensor types for this application are vibrating wire sensors with integrated thermistors (per FDOT request). The sensors were strategically located on both sides of the midline of the link slab to capture strains in the BFRP bars, strains in the concrete link-slab, and the gap between adjacent beams' ends.

All measurements have been corrected for temperature changes per recommendations of the gauge manufacturer. Data has been collected during service. The data acquisition system has been able to keep record of strains developed in the BFRP reinforcement. The strains experienced by the sensors indicated small strain levels compared to the BFRP ultimate strain levels.

In some cases, there have been some outliers or daily strain changes and maximum differential recorded on the site from Sisterbars and BFRP bars. That could be due to any interference with the system electronics or other electronics systems in the close vicinity of the sensors or due to glitches caused sometimes by the data acquisition system that could cause spikes.

In addition to live load flexural effects, this type of thermal cycling could contribute to the concrete cracking over time in the link-slab if tension stresses build-up due to global shrinkage and creep restraint of the connected FSB spans. However, after about 90 days over the time of monitoring, the average strain in the mid-joint gauges did not change significantly indicating minimal creep and or shrinkage restraint was experienced to date by the link-slab since the initial casting date. The maximum daily strain change due to thermal effects is about 500 microstrain.

Unfortunately, no live-load test was scheduled for this project due to time and budget restraints but should be considered on future projects.

7 References

- AASHTO. (2009). AASHTO LRFD bridge design guide specifications for GFRP reinforced concrete bridge decks and traffic railings, 1st Ed., Washington, DC.
- Alampalli, S. and Yannotti, A. P. (1998) “In-Service Performance of Integral Bridges and Jointless Decks” Transportation Research Record Journal of the Transportation Research Board 1624(1):1-7
- Au, A., Lam, C., Au, J., and Tharmabala, B (2013) “Eliminating Deck Joints Using Debonded Link Slabs: Research and Field Tests in Ontario” J. Bridge Eng., ASCE, 2013, 18(8): 768-778.
- Caner, A., and Zia, P. “Behavior and Design of Link Slabs for Jointless Decks” PCI Journal, Vol. 43, No. 3, pp. 68-80, May-June 1998.
- Caner, A., and Zia, P. (1998) “Behavior and Design of Link Slabs for Jointless Bridge Decks” PCI Journal, Page 68-80.
- Charuchaimontri, T., Senjuntichai, T., O’zbolt, J., and Limsuwan, E., (2008) “Effect of lap reinforcement in link slabs of highway bridges” Engineering Structures 30 (2008) 546–560.
- El-Safty, A. K.,” Analysis of Jointless Bridge Decks with Partially Debonded Simple Span Beams,” Ph.D. Dissertation, North Carolina State University, Raleigh, NC, 1994.
- ElSafty, A., and Okeil, A. M., (2008). “Extending the Service Life of Bridges Using Continuous Decks, PCI Journal - Precast/Prestressed Concrete Institute.” PCI, Vol. 53, No. 6, pp. 96-111. 30.
- Gastal, A.L. and Zia, P. (1989). “Analysis of Bridge Beams with Jointless Decks.” In: International Symposium on Durability of Structures, LISBON, Conference Report, Zurich, IABSE, ETH Honggrberg.
- Groli, G., Caldentey, A.P., Soto, A.G., Marchetto, F., and Parrotta, J.E. (2014) “Simplified serviceability design of jointless structures. Experimental verification and application to typical bridge and building structures” Engineering Structures 59 (2014) 469–483.
- Ho E. and Lukashenko, J., (2011) “LINK SLAB DECK JOINTS” 2011 Annual Conference of the Transportation Association of Canada, Edmonton, Alberta.
- Hong, Y. (2014) “Analysis and Design of Link Slabs in Jointless Bridges with Fibre Reinforced Concrete” PhD. Thesis, University of Waterloo, ON, Canada.
- Kendall, A., Keoleian, G, A., and Helfand, G.E., (2008) “Integrated Life-Cycle Assessment and Life-Cycle Cost Analysis Model for Concrete Bridge Deck Applications” J. Infrastruct. Syst., ASCE, 14(3): 214-222.
- Kim, Y. Y., Fischer, G., and Li, V. C. “Performance of Bridge Deck Link Slabs Designed with Ductile Engineered Cementitious Composite”, ACI Structural Journal, V. 101, No. 6, pp. 792-801, Nov-Dec 2004.

- Lepech., M. D. and Li. V.C. (2009) “Application of ECC for bridge deck link slabs” *Materials and Structures*, 42:1185–1195.
- Li, V. C., Fischer, V.C., Kim, G., Lepech, Y., Qian, M., Weimann, S., and Wang, S. (2003) “Durable Link Slabs for Jointless Bridge Decks Based on Strain-Hardening Cementitious Composites” Michigan Department of Transportation, Research Report RC-1438.
- Li, V.C., Lepech, M., and Li, M. (2005) “Field Demonstration of Durable Link Slabs for Jointless Bridge Decks Based on Strain-Hardening Cementitious Composites” Michigan Department of Transportation, Research Report RC- 1471.
- Mothe, R.N. (2006) “Partial continuity in prestressed concrete girder bridges with jointless decks” MSc. Thesis, Louisiana State University and Agricultural and Mechanical College.
- Okeil, A. M. and ElSafty, A. (2005). “Partial Continuity in Bridge Girders with Jointless Decks, Practice Periodical on Structural Design and Construction.” *ASCE Journal*, Vol. 10, No. 4, pp 229-238, doi:10.1061/(ASCE)1084-0680(2005)10:4(229).
- Okeil, A. M., Hossain, X., and Cai, C. S. (2013) “Field monitoring of positive moment continuity detail in a skewed prestressed concrete bulb-tee girder bridge” Spring 2013, *PCI Journal*, Page 80-90.
- Reyes, J. and Robertson, I.N., (2011). “PRECAST LINK SLABS FOR JOINTLESS BRIDGE DECKS.” Technical Report, Hawaii Department of Transportation
- Snedeker, K., White, D., and Kahn. L., (2011) “Evaluation of Performance and Maximum Length of Continuous Decks in Bridges – Part 1” GDOT Research Project No. 09-07, Task Order No. 02-64. Report, Page 130.
- Sun, C., N. Wang, and M. K. Tadros, M.K (2016). “Threaded Rod Continuity for Bridge Deck Weight.” *PCI Journal*, Precast/Prestressed Concrete Institute, Chicago, IL. V. 61, No. 3, pp. 47-67.
- Tadros, M.K. (2016), *Eliminating Expansion Joints in Bridges*, Concrete Bridge Technology, Aspire, pp. 32-35
- Thippeswamy, H.K., GangaRao, H.V.S., and Franco, J.M. (2002) “Performance Evaluation of Jointless Bridges” *J. Bridge Eng.*, ASCE, 7(5): 276-289.
- Ulku, E., Attanayake, U., and Aktan, H., (2009) “Jointless Bridge Deck with Link Slabs Design for Durability” *Transportation Research Record: Journal of the Transportation Research Board*, No. 2131, Transportation Research Board of the National Academies, Washington, D.C., 2009, pp. 68–78.
- Virginia Department of Transportation (VDOT), Jeff Milton, (March 2013), 2013 Virginia Concrete Conference Joint Maintenance and Best Practices in Deck Joint Replacement
- Wendner, R. and Strauss, A. (2015) “Inclined Approach Slab Solution for Jointless Bridges: Performance Assessment of the Soil–Structure Interaction” *J. Perform. Constr. Facil.*, ASCE, 29(2): 04014045.

- Wing, K. M. and Kowalsky, M. J. “Behaviour, Analysis, and Design of an Instrumented Link Slab Bridge” ASCE Journal of Bridge Engineering, Vol. 10, No. 3, pp. 331-344, May 2005.
- Xu, Z., Chen, B., Zhuang, Y., Tabatabai, H., and Huang, F. (2018) “Rehabilitation and Retrofitting of a Multispan Simply-Supported Adjacent Box Girder Bridge into a Jointless and Continuous Structure” J. Perform. Constr. Facil., ASCE, 32(1): 04017112.
- Zia, P., Caner, A., and ElSafty, A. (1995). “Jointless Bridge Decks.” Technical Report, FHWA/NC/95-006, North Carolina Department of Transportation (NCDOT).

8 Appendix A

Images and Illustrations Of The Bridge And Sensor Layout

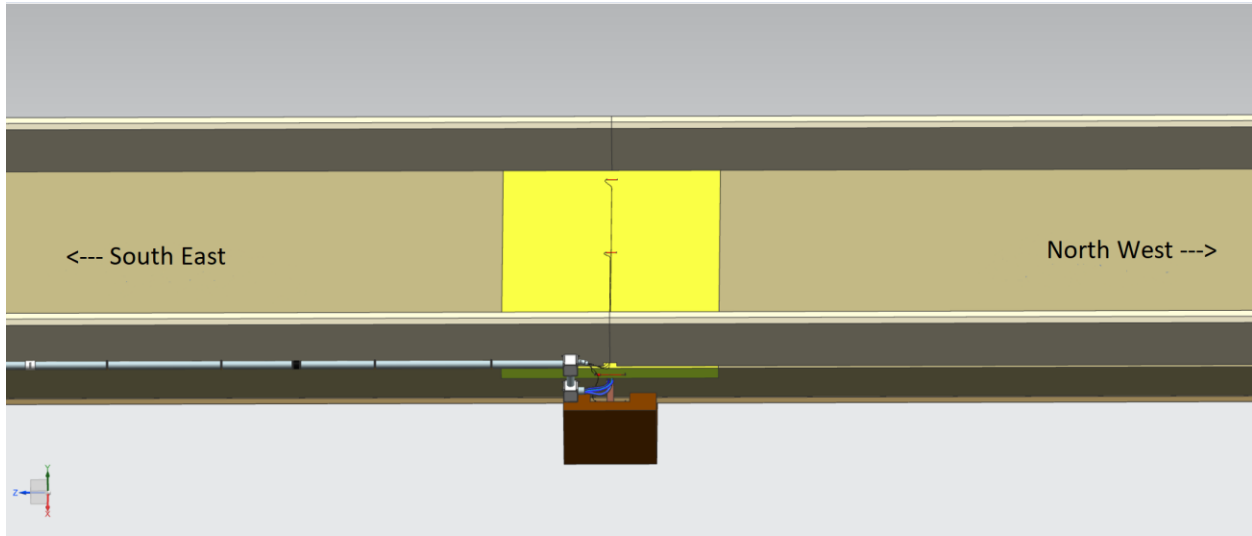


Figure A.1: Side View

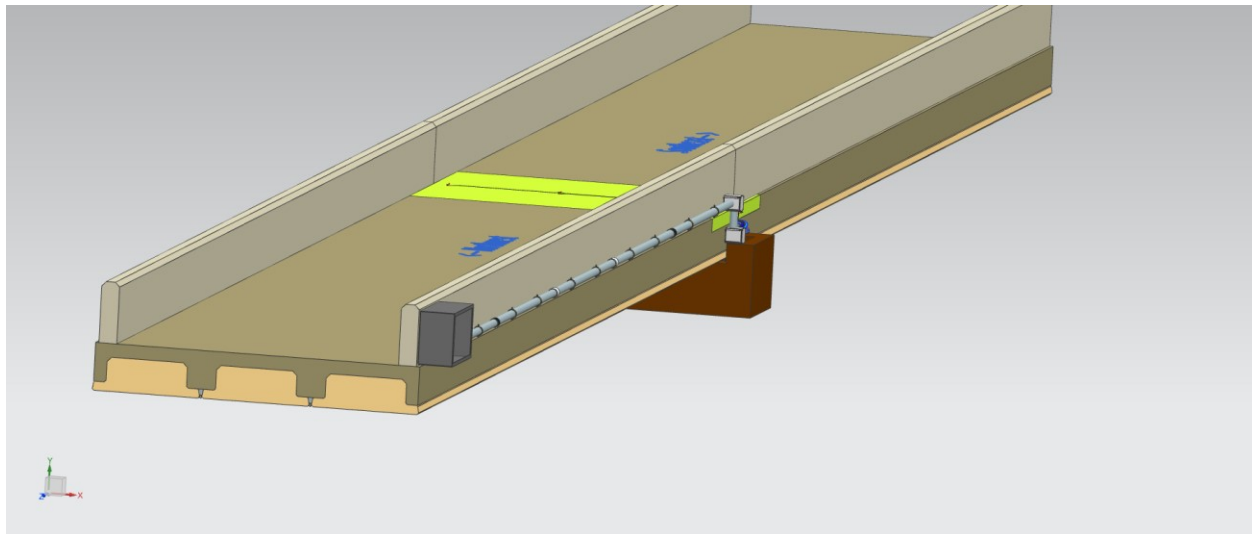


Figure A.2: Angled View

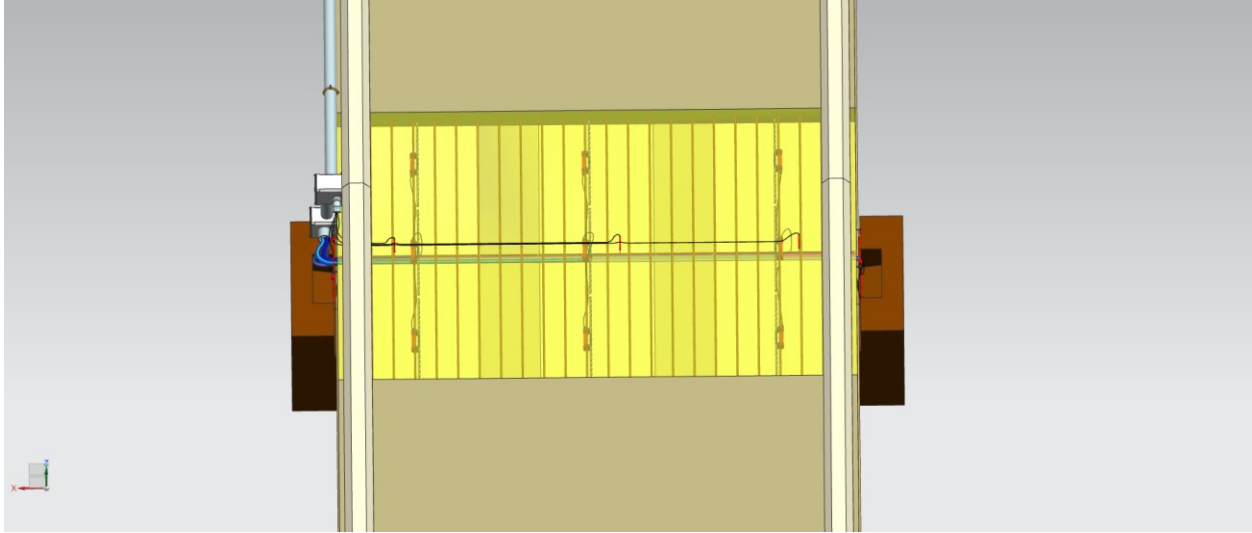


Figure A.3: Top View

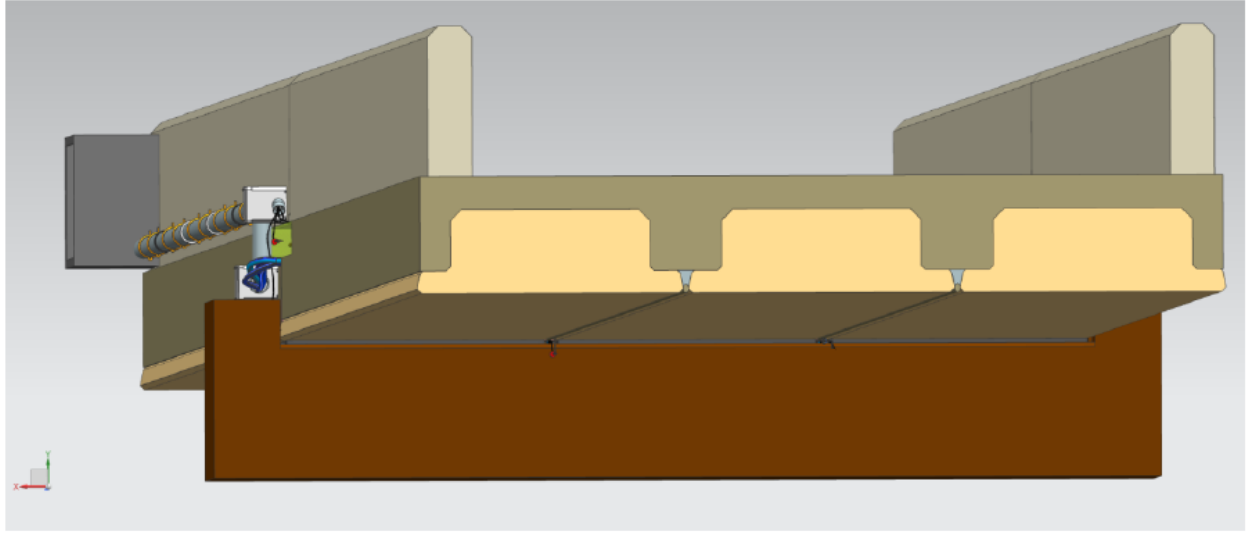


Figure A.4: End View

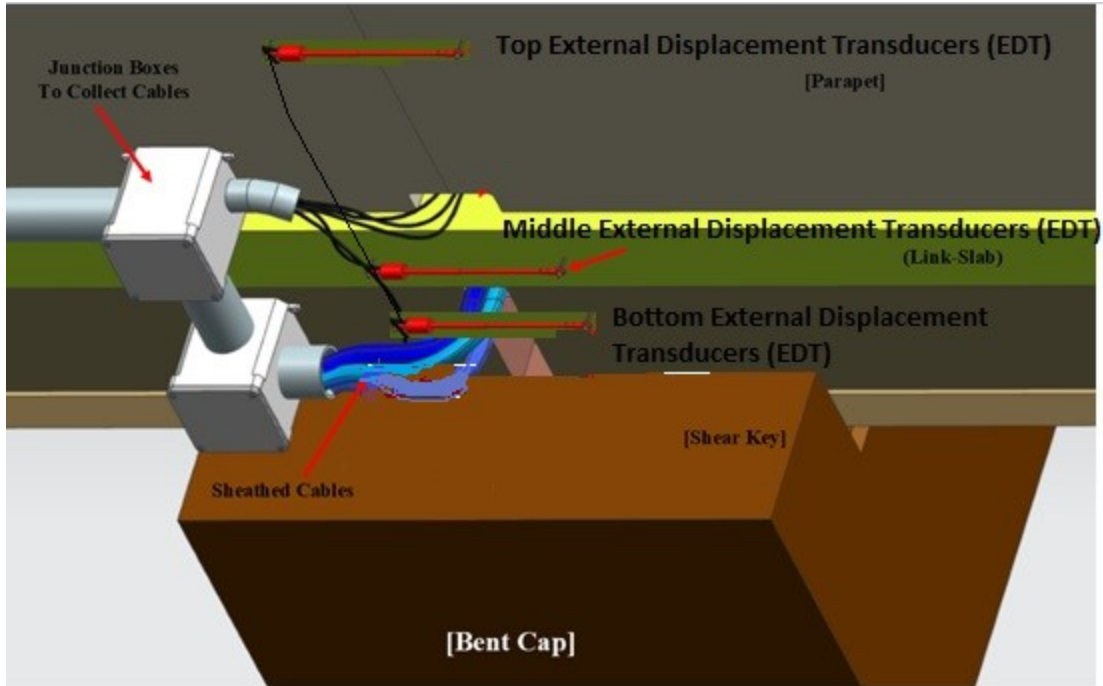


Figure A.5: Top View of Southwest Shear Key

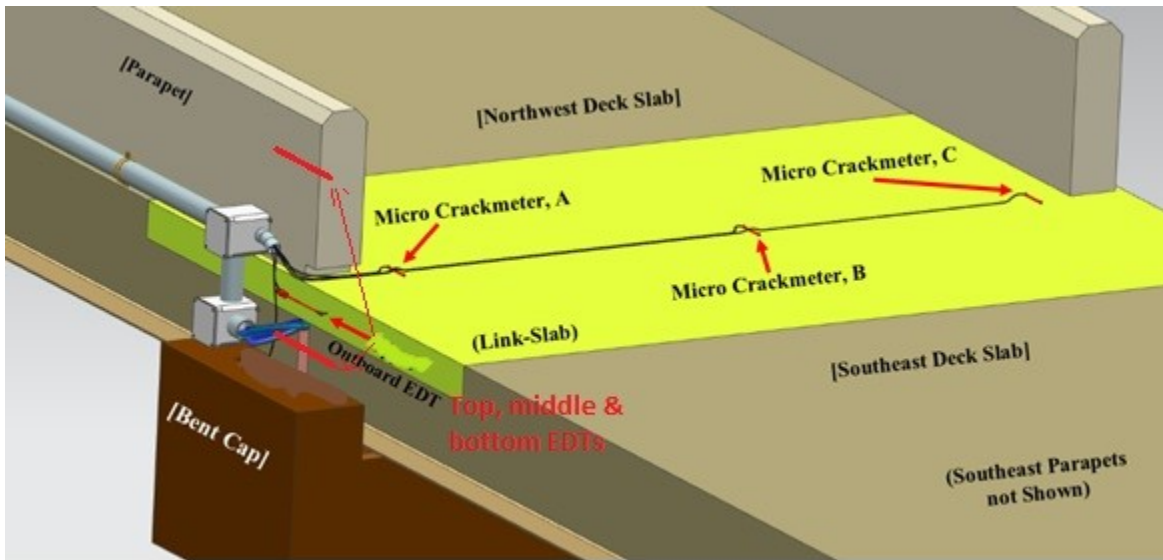


Figure A.6: Side View, Exposed

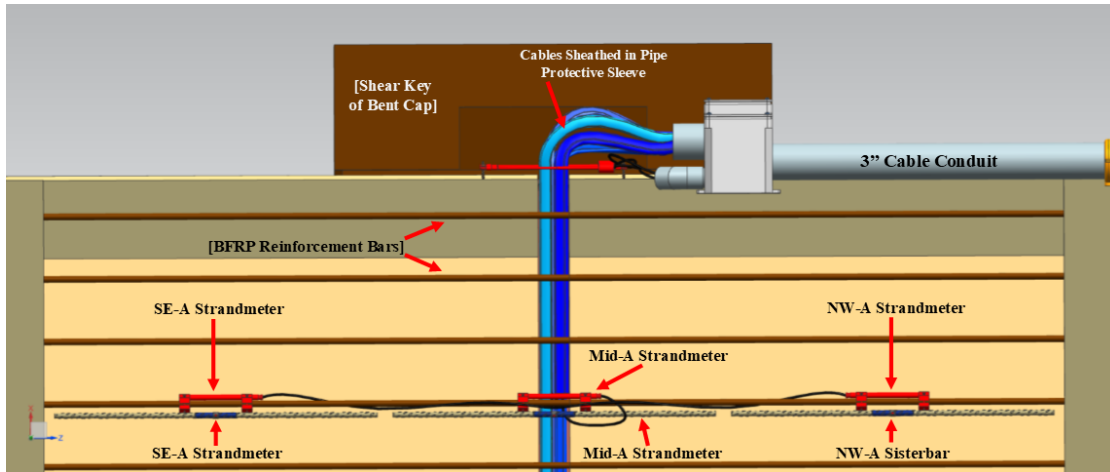


Figure A.7: Detail Link-Slab, Top View

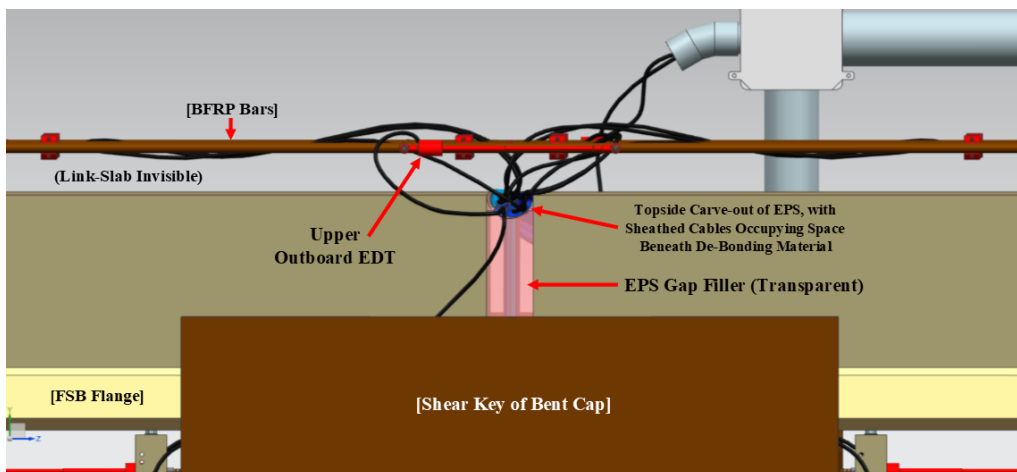


Figure A.8: Side View of Exposed Embedded Sensors and BFRP rebars

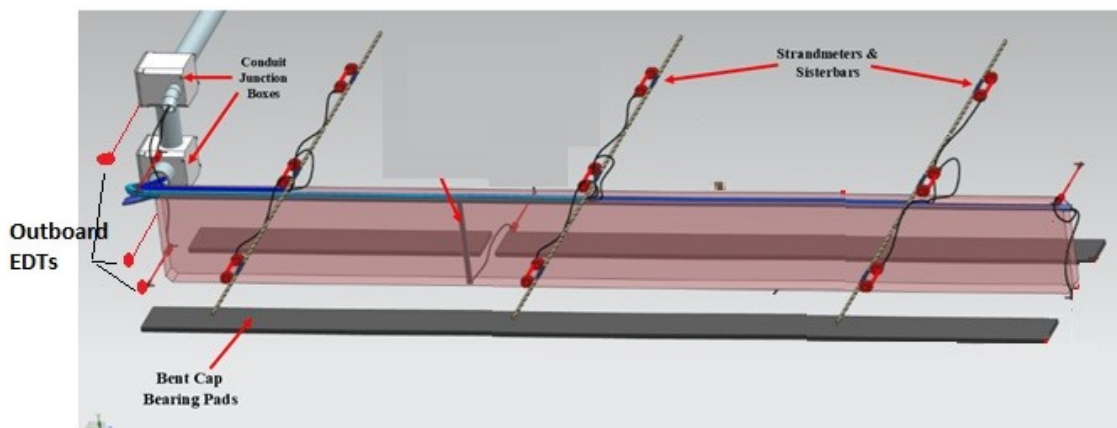


Figure A.9: Exposed View of Cable Routing (EPS is Translucent)

9 Appendix B

Sensor Layout and Information

Group #	Gauge Type/Model & Source	Resolution	Accuracy	Measuring Range	Dimensions	# of Units
1	<i>Strandmeter (4410, Geokon)</i>	<5 $\mu\epsilon$	(+/-) 0.003 mm	3 mm (15000 $\mu\epsilon$)	8" Long x 1.77" Wide Clamps	9
2	<i>Sisterbar (4911, Geokon)</i>	0.4 $\mu\epsilon$	(+/-) 7.5 $\mu\epsilon$	3000 $\mu\epsilon$	36" Length, #4 Size Rebar	9
3	<i>Micro Crackmeter (4422, Geokon)</i>	.001 mm	(+/-) 0.004 mm	4 mm	4.725" Long x 0.315" Diameter	3
4	<i>Crackmeter (4420-25, Geokon)</i>	.00625 mm	(+/-) 0.025 mm	25 mm	Gauge Length: 13.5", Dia:1"	4
5	<i>Crackmeter (4420-25, Geokon)</i>	.00625 mm	(+/-) 0.025 mm	25 mm	Gauge Length: 13.5", Dia:1"	2
6	<i>Datalogger (LC-2, Geokon)</i>	1 part in 20,000; Thermistor: 0.1 deg C	(+/-) 0.05% F.S. (450 to 4000 Hz); Thermistor: (+/-) 2.0% F.S.	450 to 4000 Hz; Thermistor: -30 deg C to 50 deg C	(LxWxH): 13.46" x 11.85" x 6.3"	2

Table B.1: Instrument Groups

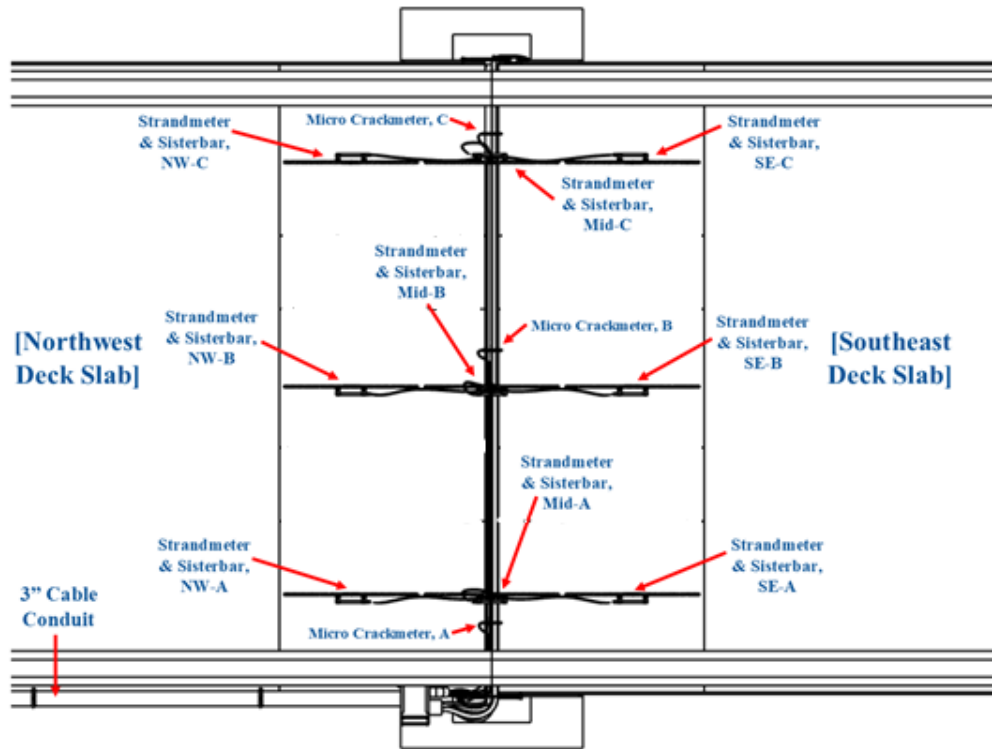


Figure B.2: Drawing, Labels of Embedded Array and Micro Crackmeters

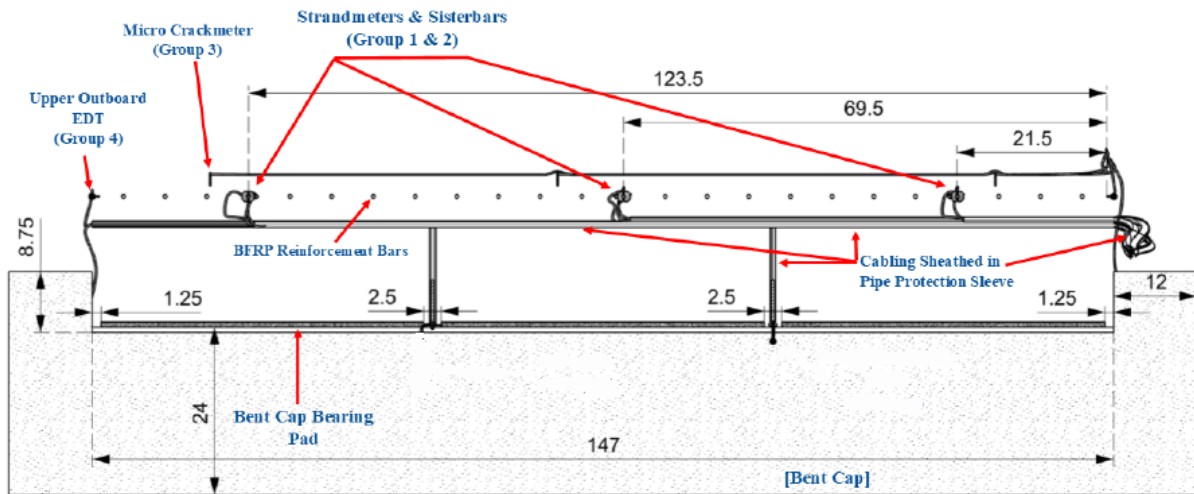


Figure B.3: Drawing, Bent Cap End View (Slabs, Beams, and Parapets not Shown)

Figure B.5: Drawing, Bridge End View No.1

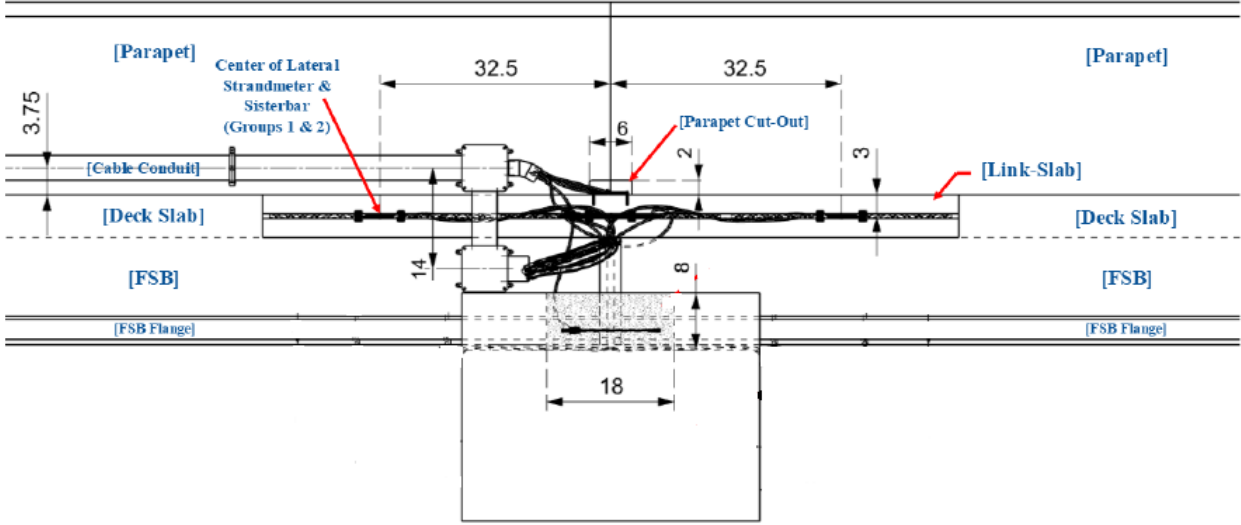


Figure B.6: Drawing, Bridge Side View No.2 (Detail of Link-Slab)

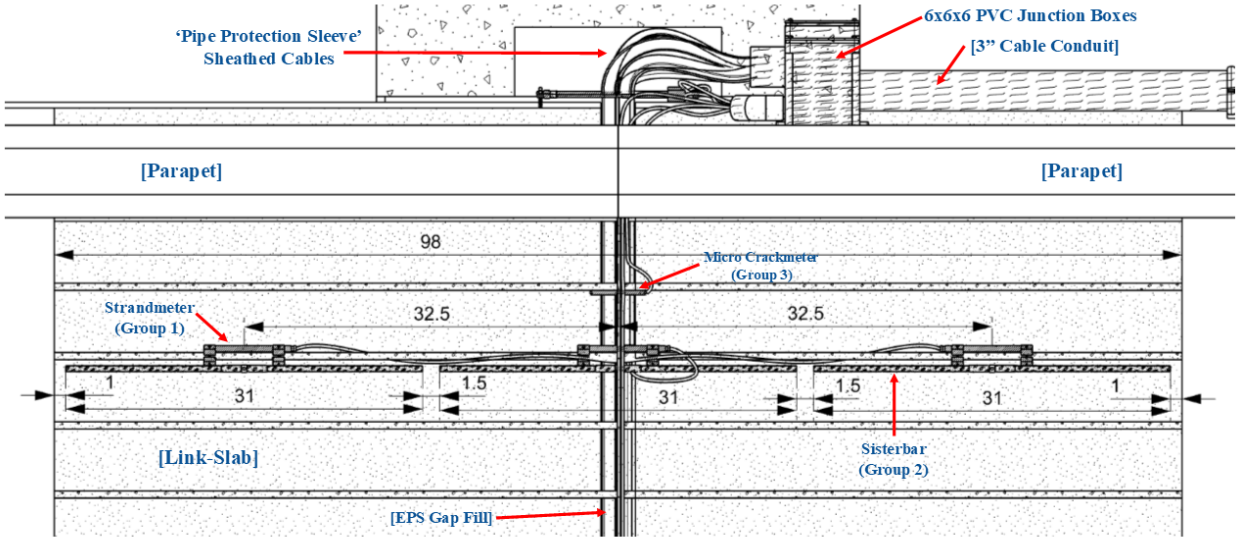


Figure B.7: Drawing, Top View Detail of Link-Slab (Southwest Side)

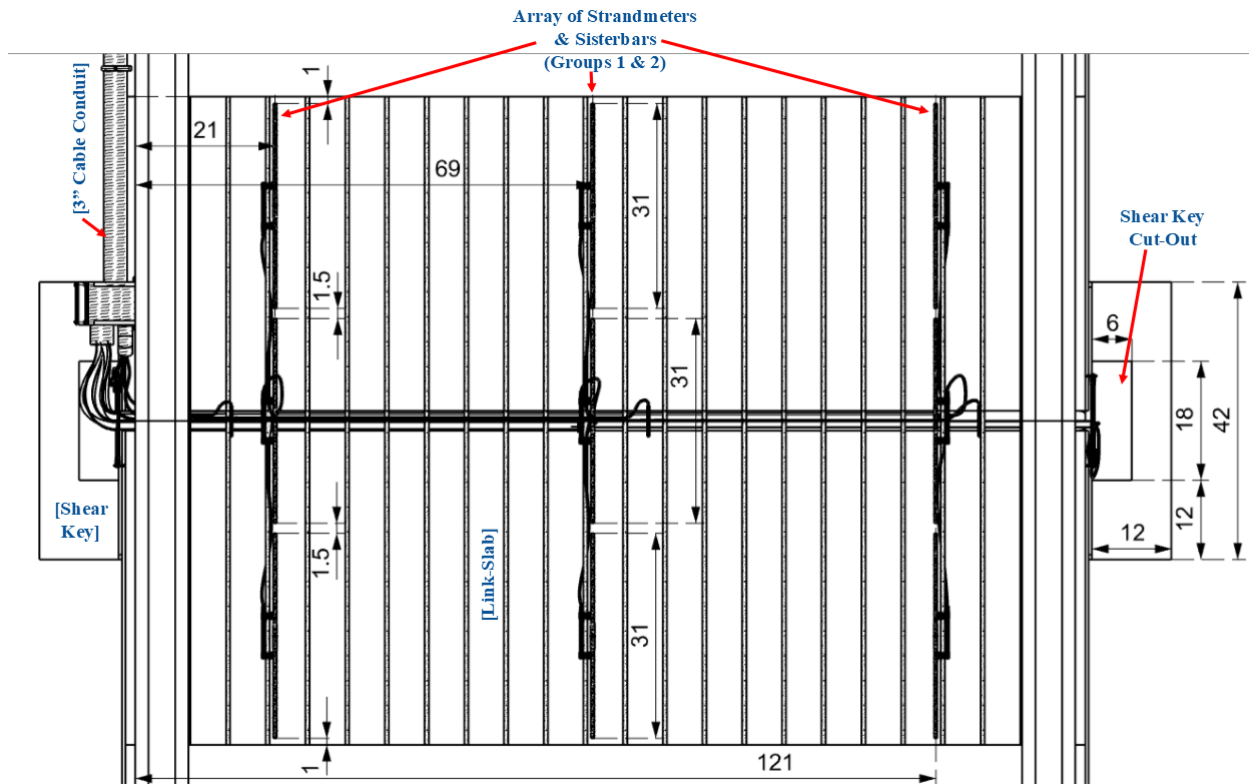


Figure B.8: Drawing, Top View of Whole Link-Slab

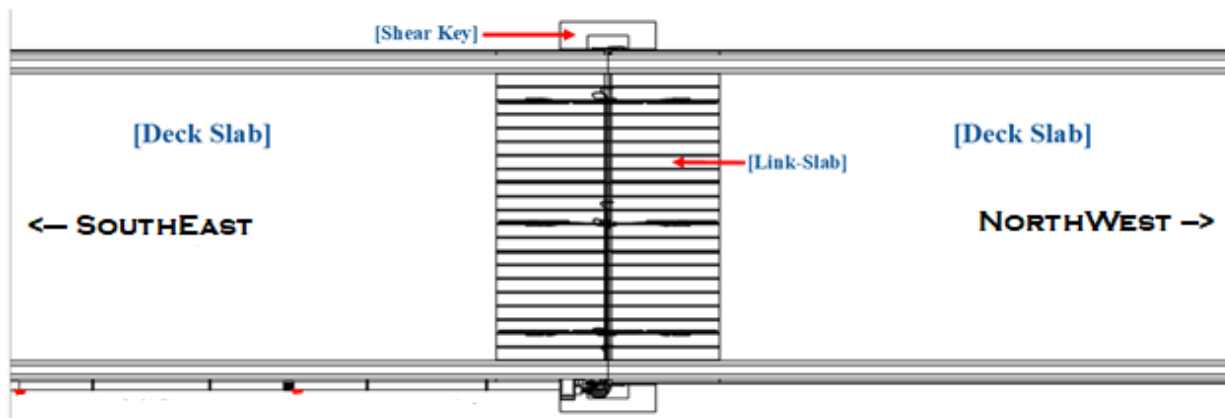


Figure B.9: Drawing, Top View of Bridge (Wide)

10 Appendix C
Manufacturer's instrument datasheets
(Credit: Geokon)

4400 Series

Vibrating Wire Displacement Transducers

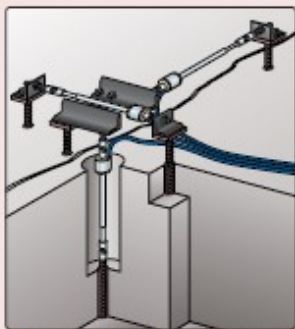
Applications

The 4400 Series are designed to measure or monitor the...

- Expansion or contraction of a joint
- Strains in tendons and steel cables
- Movement across surface cracks and joints
- Closures in underground excavations, tunnels, etc.
- Displacements associated with landslides
- Movement of boulders, snow, etc. on unstable slopes



• Model 4420 Crackmeter installation.



• Three Model 4420 Crackmeters configured as a single 3-D Crackmeter.



• Model 4410 Strandmeter (front), Model 4400 Embedment Jointmeter (center) and Model 4420 Crackmeter (rear).

Operating Principle

Geokon vibrating wire displacement transducers are designed to measure displacements across joints and cracks in concrete, rock, soil and structural members.

In essence, the transducer consists of a vibrating wire in series with a tension spring. Displacements are accommodated by a stretching of the tension spring, which produces a commensurate increase in wire tension.

The wire and spring are connected to a free-sliding rod which protrudes from, and is free to slide inside, a protective outer tube. An o-ring seal prevents water from entering.

The frequency signal is transmitted through the cable to the readout location, conditioned, and displayed on portable readouts or dataloggers.

Advantages and Limitations

The 4400 Series Displacement Transducers are fabricated entirely from stainless steel and are waterproof to 1.75 MPa, which, coupled with their excellent long-term stability, guarantees reliability and performance in even the harshest environments.

An advantage of vibrating wire displacement transducers over more conventional linear potentiometers (or LVDT's) lies mainly in the use of a frequency, rather than a voltage, as the output signal. Frequencies may be transmitted over long lengths of electrical cable without appreciable degradation caused by variations in cable resistance or leakage to ground. This allows for a readout location that may be over a thousand meters from the transducer.

Thermistors are provided with all transducers for temperature measurement.

Model 4400 Embedment Jointmeter

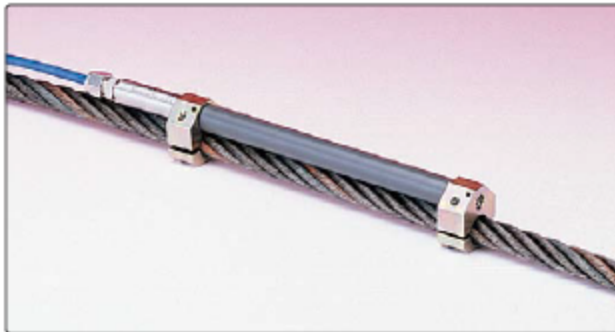


• Model 4400 Embedment Jointmeter shown with socket removed.

The Model 4400 is designed for use in construction joints; e.g. between lifts in concrete dams. In use, a socket is placed in the first lift of concrete and, when the forms are removed, a protective plug is pulled from the socket. The gage is then screwed into the socket, extended slightly and then concreted into the next lift. Any opening of the joint is then measured by the gage which is firmly anchored in each lift. The sensing gage itself, is smaller than the protective housing, and a degree of shearing motion is allowed for by the use of ball-joint connections on the gage.

A tripolar plasma surge arrestor is located inside the housing and provides protection from electrical transients such as those that may be induced by lightning.

Model 4410 Strandmeter



• Model 4410 Strandmeter

The Model 4410 Strandmeter is designed to measure strains in tendons and steel cables, including bridge tendons, cable stays, ground anchors, tiebacks, etc. Two clamps at each end of the strandmeter hold it firmly onto the cable. Various size clamps are available.

Model 4420 Crackmeter



• Model 4420 Crackmeter

The Model 4420 Crackmeters are designed to measure movement across joints such as construction joints in buildings, bridges, pipelines, dams, etc.; tension cracks and joints in rock and concrete.

The ends of the sensor are attached to anchors (with ball joints) that have been grouted, bolted, welded or bonded on opposite sides of the crack or fissure to be monitored. 3-D mounting brackets, which allow measurement of displacements in three orthogonal directions, and special clamps for attachment to a variety of earth reinforcements and geogrids, are also available.

Special versions are offered for underwater use, where water pressures exceed 1.7 MPa, and for use in cryogenic or elevated temperature regimes.

Model 4422 Micro Crackmeter



• Model 4422 Micro Crackmeter

The Model 4422 is a miniature crackmeter intended to measure displacements across surface cracks and joints. It has been specially designed for applications where access is limited and/or where monitoring instrumentation is to be as unobtrusive as possible (e.g. on historical structures or buildings).

Model 4425 Convergence Meter



• Model 4425 Convergence Meter

The Model 4425 Convergence Meter is designed to detect deformation in tunnels and underground caverns by measuring the contraction (or elongation) between 2 anchor points fixed in the walls of the tunnel or cavern.

The Model 4425 consists of a spring-tensioned vibrating wire transducer assembly, turnbuckle, 6 mm diameter connecting rods (stainless steel, fiberglass or graphite), rod clamp, and a pair of anchor points. Changes in distance between the 2 anchors are conveyed by the connecting rods and measured by the transducer.

The Model 4425 can operate in horizontal, inclined or vertical orientations. In areas where construction traffic is expected or where the instrument may be left in an exposed location, some form of protective housing should be considered.

Model 4430 Deformation Meter



• Model 4430 Deformation Meter

The Model 4430 Deformation Meter is designed to measure axial strains or deformations in boreholes in rock, concrete or soil. It can also be embedded in soils in embankments such as earth dams and highway fills. The Model 4430 can be installed in series to give a total deformation profile along a particular axis. Base lengths of the gage can vary from a minimum of 1 meter to over 25 meters.

When used in rock in horizontal or inclined downward boreholes, grouting is the most common method of installation. In vertical boreholes, a special grouting apparatus and hydraulic or snap-ring anchors are required. Direct placement or pre-wiring to a rebar cage allows use in concrete.

Model 4427 Long-Range Displacement Meter

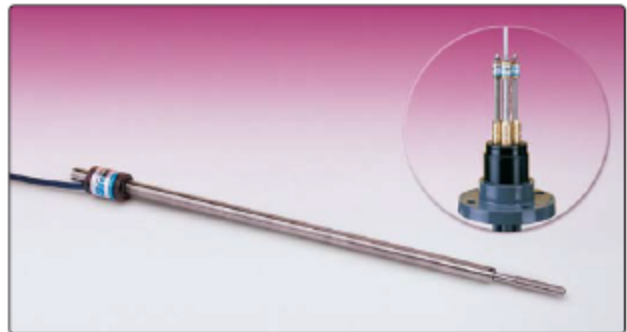


• Model 4427 Long-Range Displacement Meter

The Model 4427 Long-Range Displacement Meter is ideally suited for the measurement of large displacements associated with landslides. The Model 4427 can also be used for monitoring the movement of boulders, snow, etc., on unstable slopes.

The Model 4427 consists of a vibrating wire displacement transducer coupled to a spring motor drive by means of a lead screw. As the cable is pulled, the motor drum rotates and advances the lead screw. Thus the rotation is converted into a linear displacement which is measured by the vibrating wire displacement transducer.

Model 4450 Displacement Transducer



• Model 4450 Displacement Transducer and Extensometer Head Assembly (inset)

The Model 4450 Displacement Transducer provides remote readout capability for Borehole Extensometers (see the Geokon Model A-3, A-4, A-5, A-6 Rod-Type Borehole Extensometers data sheet for more information). They are particularly useful where other types of vibrating wire sensors are used and/or for installations where long cable runs are required.

The Model 4450 can also be installed between borehole anchors, in conjunction with the requisite length connecting rod, to provide a permanent, in-place incremental extensometer (contact Geokon for details).

Technical Specifications

Model	Standard Ranges ¹	Resolution	Accuracy	Nonlinearity	Temperature Range ¹	Dimensions
4400 Embedment Jointmeter	12.5, 25, 50, 100 mm	0.025% F.S.	±0.1% F.S.	<0.5% F.S.	-20°C to +80°C	Length: 406 mm Flange Diameter: 51 mm
4410 Strandmeter	20,000 µε	< 5 µε	±0.1% F.S.	<0.5% F.S.	-20°C to +80°C	Length: 203 mm Clamp Width: 45 mm
4420 Crackmeter	12.5, 25, 50, 100, 150 mm	0.025% F.S.	±0.1% F.S.	<0.5% F.S.	-20°C to +80°C	Lengths: 318, 362, 527 mm Coil Diameter: 25 mm
4422 Micro Crackmeter	3 mm (±1.5 mm)	0.001 mm	±0.1% F.S.	<0.5% F.S.	-20°C to +80°C	Length: 120 mm Diameter: 7.9 mm
4425 Convergence Meter	25, 50, 100, 150 mm	0.025% F.S.	±0.1% F.S.	<0.5% F.S.	-20°C to +80°C	Transducer Lengths: 356, 508, 838 mm Transducer Diameter: 25 mm
4427 Long-Range Displacement Meter	1, 2 m (without resetting)	0.025% F.S.	±1.0% F.S.	—	-30°C to +60°C	Enclosure (L × W × H): 610 × 152 × 152 mm
4430 Deformation Meter	25, 50, 100 mm	0.02% F.S.	±0.1% F.S.	<0.5% F.S.	-20°C to +80°C	Length: varies Flange Diameter: 50 mm
4450 Displacement Transducer	12.5, 50, 100, 150, 300 mm	0.02% F.S.	±0.1% F.S.	<0.5% F.S.	-20°C to +80°C	Lengths: 210, 212, 270, 410 mm Coil Diameter: 19 mm

¹Other ranges available on request.

Rebar Strainmeters and "Sister Bars"

Applications

Rebar Strainmeters are commonly used for measuring strains in...

- Concrete piles & caissons
- Slurry walls
- Cast-in-place concrete piles
- Concrete foundation slabs and footings
- Osterberg pile tests
- All concrete structures



• Close-up of Model 4911 shown as installed in concrete pile reinforcing cage.



• Model 4911A Rebar Strainmeter (front) and the Model 4911 "Sister Bar" (rear).

Operating Principle

Rebar Strainmeters and "Sister Bars" are designed to be embedded in concrete for the purpose of measuring concrete strains due to imposed loads. The Rebar Strainmeter is designed to be welded into, and become an integral part of, the existing rebar cage, while the "Sister Bar" is installed by tying it alongside an existing length of rebar in the rebar cage.

The rebar extensions on either side of the central strain-gauged area are long enough to ensure adequate contact with the surrounding concrete so that the measured strains inside the steel are equal to the strains in the surrounding concrete.

In use, Rebar Strainmeters and "Sister Bars" are usually installed in pairs on either side of the neutral axis of the structural member being investigated. This is done so that bending moments may be analyzed in addition to axial loads.

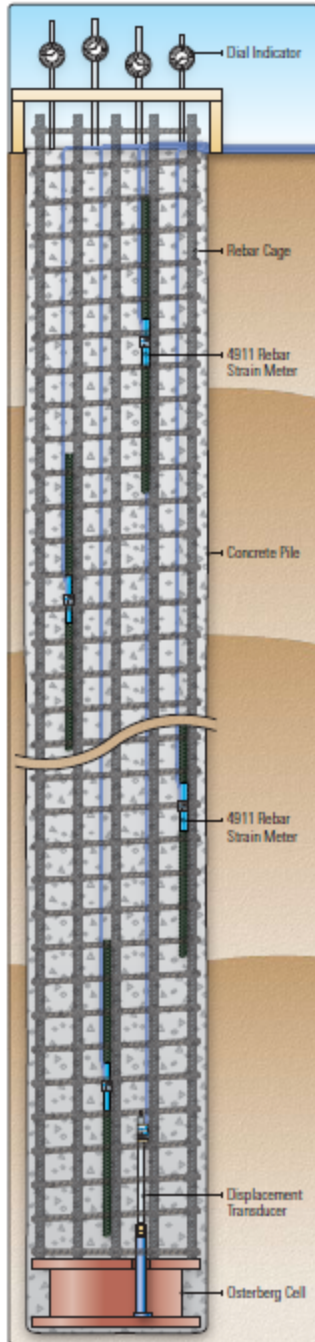
A built-in thermistor enables the measurement of temperatures and aids in the evaluation of thermally induced strains.

Advantages and Limitations

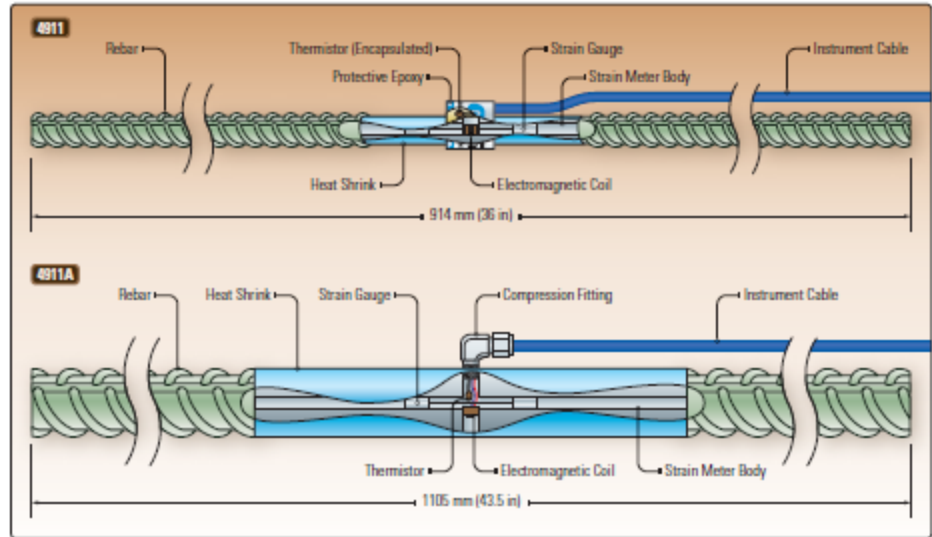
The main advantage of the Rebar Strainmeters and "Sister Bars" lies in their ruggedness. They are fully waterproof and virtually indestructible so that, if the cable is adequately protected, they are safe from damage during the concrete placement.

Each Rebar Strainmeter and "Sister Bar" is individually calibrated and tested for weld strength. The Rebar Strainmeter requires the services of an experienced welder who can guarantee full-strength welds, whereas the "Sister Bar" is very easy to install.

The single vibrating wire strain sensor, located along the axis of the strainmeter, is not affected by the bending of the strainmeter itself. It also has the advantage of all vibrating wire sensors, namely: long-term stability, it can be used with long cables and it's relatively unaffected by moisture intrusion into the cables.



● Installation of the Model 4911 in an Osterberg Cell pile test. (For more information regarding Osterberg Cell pile testing, please contact Loadtest, Inc. — www.loadtest.com.)



● Illustration of the Model 4911 "Sister Bar" and Model 4911A Rebar Strainmeters and their various components.

System Components

A vibrating wire strain gauge sensor is fixed axially inside a short, central length of round steel bar. This central section is de-bonded from the surrounding concrete by means of a plastic coating, and is extended by welding a length of rebar to each end. The Model 4911A Rebar Strainmeter is available in various sizes to match the size of the rebar cage into which it is to be welded, whereas the Model 4911 "Sister Bar" comes in one size only (#4 rebar, at approximately 12.7 mm in diameter).

A thermistor to measure temperature changes can be included in the 4911 and 4911A sensors.

Readouts and Cables

The 4911 Series Rebar Strainmeters are read using the Model GK-404 or GK-405 Readouts. Alternatively, the LC-2 Series or 8600 Series Dataloggers can be used.

The 4911 Series Rebar Strainmeters use the Model 02-250V6 4 pair, 22 AWG cable.

Technical Specifications

	4911	4911A
Standard Range	3000 $\mu\epsilon$	3000 $\mu\epsilon$
Resolution	0.4 $\mu\epsilon$	0.4 $\mu\epsilon$
Accuracy ¹	$\pm 0.25\%$ F.S.	$\pm 0.25\%$ F.S.
Nonlinearity	< 0.5% F.S.	< 0.5% F.S.
Temperature Range ²	-20°C to +80°C	-20°C to +80°C
Rebar Sizes	#4 (Sister Bar)	#6, 7, 8, 9, 10, 11, 14
Length	914 mm	1105 mm

¹Accuracy established under laboratory conditions.
²Other ranges available on request.

LC-2 Series Dataloggers

Applications

The LC-2 Series Dataloggers are used to read all **GEOKON®** vibrating wire instruments. Sensors that can be read and monitored include...

- Piezometers
- Precision water level sensors
- Crackmeters
- Settlement systems
- Temperature sensors



• Model 8002-WP-2 (LC-2WP) Waterproof Single-Channel Datalogger.



• Model 8002-16-1 (LC-2x16) 16-Channel, Model 8002-4-1 (LC-2x4) 4-Channel and Model 8002-1-1 (LC-2) Single-Channel Dataloggers.

Operating Principle

The Model 8002 LC-2 Series Dataloggers are designed to read both the vibrating wire element and the integral thermistor of any **GEOKON** vibrating wire sensor.

The LC-2 (internal hard wired transducer connection), LC-2A (10-pin transducer connector option) and LC-2WP (waterproof option) are designed to be standalone, single-channel dataloggers, which makes them especially useful for the remote and continuous monitoring of isolated sensors.

The LC-2x4 is a self-contained, 4-channel version (vibrating wire with thermistor) of the LC-2, and the LC-2x16 is a 16-channel (vibrating wire with thermistor) version.

The LC-2, LC-2x4 and LC-2x16 are housed inside Fiberglass NEMA 4X enclosures, which makes them very robust, weather-proof and particularly well-suited to operation in harsh environments. The LC-2WP is a waterproof version housed inside a rugged PVC enclosure. Low power consumption provides long battery life and the condition of the main batteries is reported as an element in the data array.

Data memory consists of 320K bytes of EEPROM. This translates into a memory storage capacity of 16,000 arrays for the LC-2 and LC-2A, 10,666 arrays for the

LC-2x4 and 3,555 arrays for the LC-2x16. Each array consists of the datalogger ID, day (Julian or month/day format), time (HHMM), seconds, main battery voltage, datalogger temperature, vibrating wire sensor reading (in engineering units), the sensor temperature and array number. The array transmission is in comma delineated ASCII text, for easy importation into popular spreadsheet programs.

Up to 6 intervals may be specified from a logarithmic table, with a maximum of 255 iterations. The programmed intervals can be started or stopped once at preset times of the day.

Power

The Model 8002 LC-2 Series Dataloggers are powered by easily accessible alkaline or lithium (optional) D cells. Additional power options, including internal and external 12 V batteries and solar panels, are available (please contact **GEOKON** for more information).

Communications

The Model 8002 LC-2 Series Dataloggers are available with an RS-232 Serial Interface or with a direct USB 2.0 connection; patch cords are supplied for this purpose.

Technical Specifications

	Single-Channel	4-Channel	16-Channel
	LC-2, LC-2A, LC-2WP*	LC-2x4, LC-2x4A	LC-2x16
Measurement Accuracy	±0.05% F.S. (450-4000 Hz)	±0.05% F.S. (450-4000 Hz)	±0.05% F.S. (450-4000 Hz)
Measurement Resolution	1 part in 20,000	1 part in 20,000	1 part in 20,000
Program Memory	24K FLASH	24K FLASH	24K FLASH
Data Memory	320K EEPROM	320K EEPROM	320K EEPROM
Data Connection	RS-232, USB or RS-485	RS-232, USB or RS-485	RS-232, USB or RS-485
Storage Capacity (Arrays)	16,000 ¹	10,666	3,555
Temperature Range	-30°C to +50°C	-30°C to +50°C	-30°C to +50°C
Temperature Measurement	(accuracy) 2.0% F.S. (resolution) 0.1 °C	(accuracy) 2.0% F.S. (resolution) 0.1 °C	(accuracy) 2.0% F.S. (resolution) 0.1 °C
Communication Speed	9600 bps	9600 bps	9600 bps
Communication Parameters	8 data bits, no parity, 1 stop bit	8 data bits, no parity, 1 stop bit	8 data bits, no parity, 1 stop bit
Power Supply	3 VDC (2 Alkaline 'D' cells)	3 VDC (2 Alkaline 'D' cells)	3 VDC (4 Alkaline 'D' cells)
Communication Current	< 100 mA	< 100 mA	< 100 mA
Measurement Current	< 250 mA	< 250 mA	< 250 mA
Quiescent Current	< 500 µA	< 500 µA	< 500 µA
Scan Interval	3 - 86,400 seconds (24 hours)	10 - 86,400 seconds (24 hours)	30 - 86,400 seconds (24 hours)
Operating Time (20°C)	3 days - 3 years, depending on scan interval	8 days - 2 years, depending on scan interval	8 days - 2 years, depending on scan interval
Sensor Connection	(LC-2, LC-2WP*) Hard wired (LC-2A) 10-pin Connector	(LC-2x4) Hard wired (LC-2x4A) 10-pin Connector	(LC-2x16) Hard wired (LC-2x16A) 10-pin Connector
L x W x H H x B	(LC-2, LC-2A) 122 x 120 x 91 mm (LC-2WP*) 211 x 168 mm	260 x 160 x 91 mm	342 x 301 x 160 mm ²

¹8,000 arrays when used with LogView software. ²Does not include mounting feet.

Ordering Information

	Single-Channel	4-Channel	16-Channel
Data Connection	LC-2, LC-2A, LC-2WP*	LC-2x4	LC-2x16
RS-232	8002-1-1, 8002-1A-1	8002-4-1, 8002-4A-1	8002-16-1, 8002-16A-1
USB	8002-1-2, 8002-1A-2, 8002-WP-2*	8002-4-2, 8002-4A-2	8002-16-2, 8002-16A-2
RS-485	8002-1-3, 8002-1A-3	8002-4-3	8002-16-3

Software

LogView Software simplifies the task of configuration, communication, monitoring, data collection and data reduction using the Model 8002 (LC-2) Series Dataloggers.

LogView is compatible with **Windows®** 2000, XP, XP Pro, Vista and 7.

Please see the Model 8001-3 LogView Software data sheet for more information.

*PLEASE NOTE: THE MODEL 8002-WP-2 (LC-2WP) WATERPROOF SINGLE-CHANNEL DATALOGGER IS NOT CE APPROVED.

Instrumentation Cables

Applications

GEOKON® cables are of the highest quality materials and construction. They are designed to be matched with the appropriate instrument for a variety of geotechnical and hydrological applications. Standard and specialized cables are available for...

- Typical applications
- High temperature environments
- Extra abrasion resistance
- Heavy duty use



• The Model 4500HT High Temperature Piezometer depicts a **Teflon®** cable threaded inside stainless steel tubing.



• Standard **GEOKON** cables.

Cable Design

GEOKON cables are made from individual stranded copper conductors encased in an insulation material. Individual, insulated conductors are twisted into pairs, bundled inside a conductive Mylar-type shielding material and then covered by an outer jacket made from the most suitable material. In addition, cables may be water blocked, armored, or may contain steel or **Kevlar®** cables for additional strength, or plastic tubes for circulation fluids, or for venting to atmosphere.

Cable Conductors

In general, the number of conductors in a cable is determined by the number of sensors to be connected to the cable, and the number of conductors required by each sensor.

The type of conductor normally used is stranded, 22 AWG tinned copper. Stranded conductors are more flexible than solid conductors, which makes the cable easier to handle during installation.

Cable Shielding and Insulation

Shielding provides protection from electromagnetic radiation coming from nearby electrical equipment, lightning strikes and fields surrounding power lines, transformers, etc. **GEOKON** multi-conductor cables are individually shielded and twisted in pairs, which helps minimize common mode interference. Drain wires connected electrically to Mylar-type shields provide a simple means of connecting all the shields to a common ground. For applications with very high levels of EMI, such as in pumping wells, a special cable with a braided shield can be provided.

Plastic insulation is typically used on the individual copper conductors. Polyethylene or polypropylene insulation is used at normal temperatures and **Teflon** is most often used for high temperature.

Outer Jackets

GEOKON cable jackets are thicker than regular commercial types, and pressure extruded, which produces cables that are rounder, firmer and easier to grip and seal at the point of entry on the sensor. A wide variety of outer jacket materials is available depending on the end use:

Neoprene: A synthetic rubber compound commonly used for outdoor applications, with good resistance to gasoline, oils etc. Ordinary rubber should never be used.

PVC: A common choice for its good electrical properties and for being waterproof. It should not be used at low temperatures where it becomes brittle.

Polyurethane: This material is very resistant to cuts and abrasions making it useful for cables that are subject to repeated rough handling. It is not as water resistant as PVC but has better low temperature capabilities.

High Density Polyethylene: An excellent material that is highly resistant to environmental attack and exhibits excellent low temperature characteristics. Unfortunately, like **Teflon**, the material is so slippery that splicing and potting compounds will not stick to it.

Teflon: This material is essential wherever sensors and cables are subject to high temperature. It has outstanding resistance to environmental attack and has excellent low temperature properties. However, splicing and potting compounds will not adhere to it.

Other compounds such as **Kevlar** or **Kapton®** etc. may be required where there is a need for low smoke emissions, flame retardant, or resistance to nuclear radiation.

Armor

Armored cables are most often needed for sensors installed in earth embankments or landfills where large forces are exerted on the cable by compaction equipment and earth moving vehicles, and by settlement, "weaving," and side-ways spreading of the embankment as it is built. Armored cables should not be connected directly to strain gauges or crackmeters because the stiffness of the cable would pull on the gauge and alter the readings. Armored cable is not necessary in concrete. The armor usually takes the form of a helically laid layer of steel wire. In very severe situations, regular cable may be put inside stainless steel tubing.

Vented Cables

Special cables are available which contain plastic tubes inside of them as well as the usual conductors. These tubes can be used to transport air or other fluids. This kind of cable is required for vented piezometers, where a single vent tube allows the inside of the pressure sensor to be connected to the ambient atmosphere to provide automatic barometric compensation.

Cable Splices

Cable splicing is best done using commercially available splicing kits containing butt splice connectors and epoxy potting compounds. These help provide a waterproof and mechanically strong splice. Armored cables are difficult to splice if the mechanical strength is to be maintained; special mechanical connections need to be fabricated which will grip the armor firmly.

Technical Specifications

Model	Conductors	Conductor Insulation	Drain Wire	Cable Jacket*	Nominal O.D.	Temp. Range
02-187P6	4-conductor, 2 twisted pairs, 22 AWG 7/30	8 mil HDPP	24 AWG	Blue PU	4.75 mm (±0.25 mm)	-20 °C to +80 °C
02-187V3	4-conductor, 2 twisted pairs, 22 AWG 7/30	8 mil HDPP	24 AWG	Red PVC	4.75 mm (±0.25 mm)	-20 °C to +80 °C
02-250P4	4-conductor, 2 twisted pairs, 22 AWG 7/30	8 mil HDPP	24 AWG	Green PU	6.35 mm (±0.25 mm)	-20 °C to +80 °C
02-250T	4-conductor, 2 twisted pairs, 22 AWG 19/34	10 mil FEP	24 AWG	White Teflon with aluminum polyester foil shielding	5.20 mm (±0.25 mm)	-80 °C to +200 °C
02-250V6	4-conductor, 2 twisted pairs, 22 AWG 7/30	10 mil HDPP	24 AWG	Blue PVC	6.35 mm (±0.25 mm)	-20 °C to +80 °C
02-313P1	4-conductor, 2 twisted pairs, 22 AWG 7/30	10 mil HDPP	24 AWG	Black PU with Integral stranded steel wire	7.95 mm (±0.38 mm)	-20 °C to +80 °C
02-335V78	4-conductor, 2 twisted pairs, 24 AWG 7/32	10 mil HDPP	24 AWG	Yellow PU with Integral 0.125" Ø PE vent tube	8.50 mm (±0.38 mm)	-20 °C to +80 °C
02-500PE1A	4-conductor, 2 twisted pairs, 22 AWG 7/30	10 mil HDPP	24 AWG	Black PVC Inner; Black MDPE outer, with served armor	12.70 mm (±0.38 mm)	-20 °C to +80 °C
03-250V0	6-conductor, 2 twisted pairs, 24 AWG 7/32	10 mil HDPP	24 AWG	Black PVC	6.35 mm (±0.38 mm)	-20 °C to +80 °C
04-375V9	8-conductor, 4 twisted pairs, 22 AWG 7/30	10 mil HDPP	22 AWG	Violet PVC	9.50 mm (±0.38 mm)	-20 °C to +80 °C
04-500VT10	8-conductor, 4 twisted pairs, 22 AWG 7/30	10 mil HDPP	22 AWG	Gray PVC with Integral 0.125" Ø PE vent tube	12.70 mm (±0.38 mm)	-20 °C to +80 °C
05-375V12	10-conductor, 5 twisted pairs, 22 AWG 7/30	10 mil HDPP	22 AWG	Tan PVC	9.50 mm (±0.38 mm)	-20 °C to +80 °C
06-312V0	12-conductor, 6 twisted pairs, 24 AWG 7/32	10 mil HDPP	24 AWG	Black PVC	7.95 mm (±0.38 mm)	-20 °C to +80 °C
06-500V7	12-conductor, 6 twisted pairs, 22 AWG 7/30	10 mil HDPP	22 AWG	Orange PVC	12.70 mm (±0.38 mm)	-20 °C to +80 °C
12-625V5	24-conductor, 12 twisted pairs, 22 AWG 7/30	10 mil HDPP	22 AWG	Brown PVC	15.90 mm (±0.38 mm)	-20 °C to +80 °C

*All outer cable jackets are pressure extruded. In addition, other cable jackets are available for special applications.

FEP - Fluorinated Ethylene Propylene (Teflon) | HDPP - High Density Polypropylene | MDPE - Medium Density Polyethylene | PE - Polyethylene | PP - Polypropylene | PU - Polyurethane | PVC - Polyvinylchloride

GEOKON | **TRUSTED MEASUREMENTS**

GEOKON
48 Spencer Street
Lebanon, NH 03766 · USA

www.geokon.com
e: info@geokon.com
p: +1-603-448-1562

GEOKON is an
ISO 9001:2015
registered company

The **GEOKON** logo and word mark are registered trademarks with the United States Patent and Trademark Office. | **GEOKON** maintains an ongoing policy of design review and reserves the right to amend products and specifications without notice. | **Teflon**®, **Kevlar**® and **Kapton**® are registered trademarks of E.I. du Pont de Nemours and Company or its affiliates. | All other trademarks are the property of their respective owners.

©GEOKON. All Rights Reserved. | Rev-G-04/11/2019

11 Appendix D

Literature Review

The national bridge inventory indicates that a big percentage of the highway bridges in United States are designed as single or multiple simple-span girders supported at the piers and abutments and separated by joints (FHWA 2004). These joints are provided at the girder ends of each simple span to allow the movement of the deck and superstructure due to temperature changes, shrinkage, creep, and other effects. These deck joints generally lead to water, sometimes contaminated with chlorides, leaking through the joints causing deterioration and corrosion of the bridge deck, girders, bearing, and supporting systems. Joints can also get filled with debris and fail to allow expansion and contraction of the superstructure. Therefore, the joint systems affect the durability of bridge structures and do not provide a reliable and leak-proof performance. In addition, joints and bearings can be expensive to install and maintain.

A growing trend in bridge design has been toward the elimination of joints and bearings in the bridge superstructure. Yet, the behavior of jointless bridge deck is not precisely known and the designs could have some uncertainties. Despite the numerous benefits of jointless bridge decks, there is no standardized design procedures for these bridges and there is only a list of specifications and design recommendations available. Therefore, there is a need to further investigate the feasibility of an innovative system for reducing or eliminating the number of bridge deck joints. The alternatives include using a concrete or ultra-high-performance concrete (UHPC) link-slab reinforced with steel or fiber-reinforced polymer (FRP) rebar to join adjacent bridge decks without imposing girder continuity.

Over many years, the use of jointless bridges has proven to be an excellent alternative to preserve bridges from the adverse effects of debris, leaking water, and salt induced corrosion damage. The jointless bridge option had also proven to be an economical option that provided several inherent design advantages. In the AASHTO LRFD Bridge Design Specifications, there are no requirements for maximum bridge length allowed without expansion joints. Most state highway agencies allow eliminating joints for bridges whose lengths are less than 350 feet for bridges with steel beams and 650 feet with concrete beams; however, there are some bridges over 1000 ft long that have performed well without expansion joint (Tadros 2016).

Several researchers indicted the effect of deck continuity over the piers on the moment developed in the spans, the reduction in deflection and vibration than simple span bridge girders, the improved durability and riding quality after eliminating the joints. Gastal and Zia (1989) performed an analysis of bridge beams with jointless decks. ElSafty (1994) conducted an analysis and investigation of jointless bridge decks with partially debonded simple span beams. Zia et al. (1998) investigated casting fully-continuous deck over simply supported girders with partial debonding of the deck from the girders ends at supports, using both numerical and experimental analysis, as shown in Fig. 2. Okeil and Elsafty (2005) investigated the partial continuity in bridge girders with jointless decks and the effect of the system's support configuration on the axial force developed in the link-slab. Caner and Zia (1998) presented the results of a test program to investigate the behavior of link-slabs connecting two adjacent simple-span girders and proposed a simple method for designing the link-slab. ElSafty and Okeil (2008) also investigated extending the service life of bridges using continuous decks, as shown in Fig. 3 and Fig. 4.



Fig. 2: Testing of a 2-span bridge model - Zia et al. (1998)

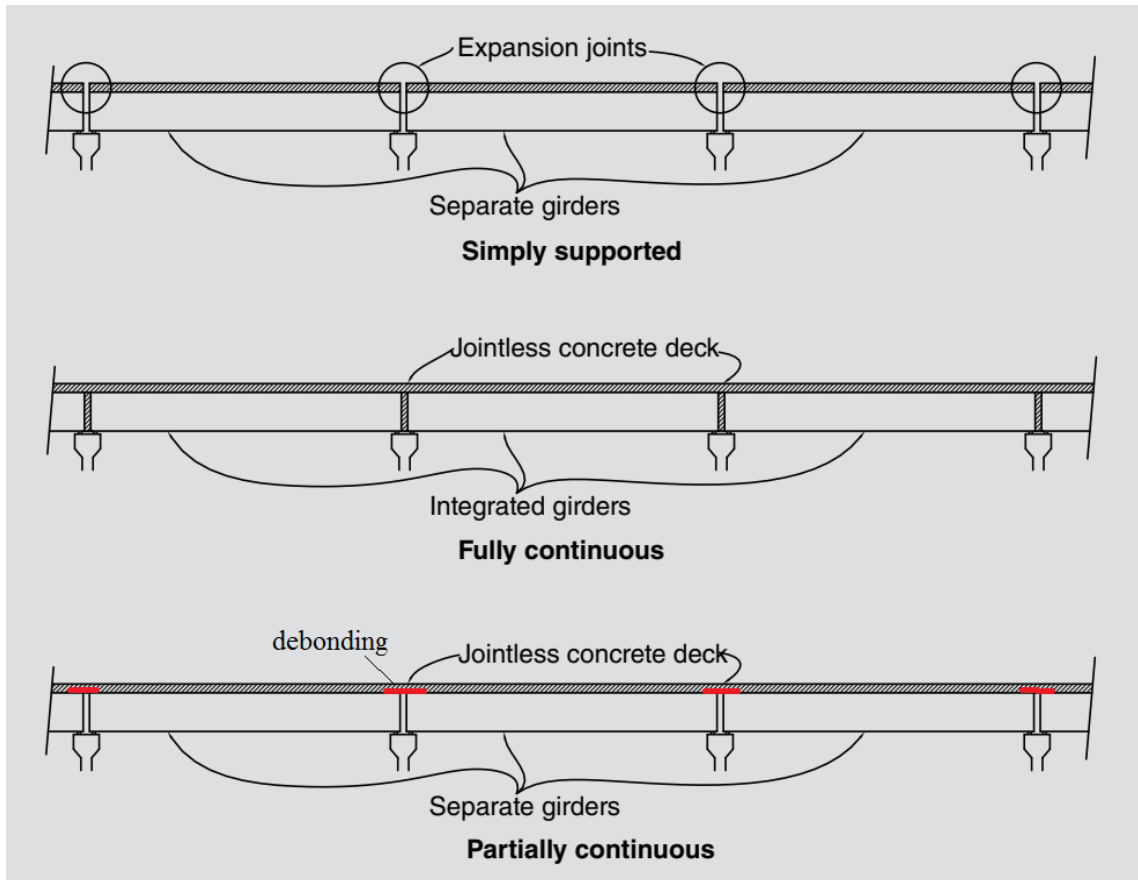


Fig. 3: Some types of jointless bridge decks

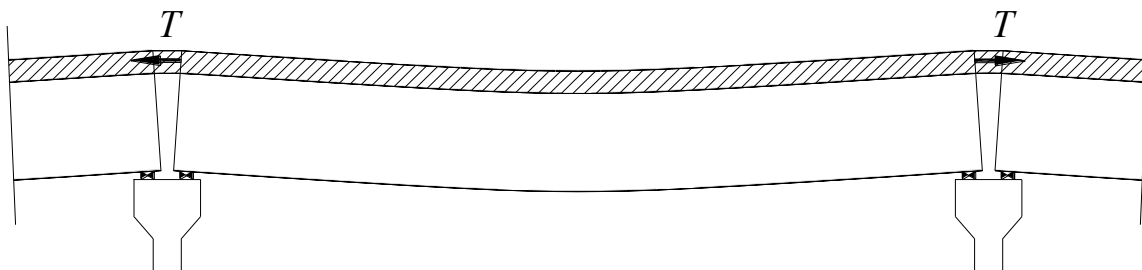


Fig. 4: Continuity caused by linking concrete decks in adjacent spans

Thippeswamy et al. (2002) conducted an investigation on jointless bridges to study the behavior of jointless bridges supported on piles and spread footings and subjected to varying load conditions. In addition, time-dependent material properties have also been investigated. In their study, Thippeswamy et al. (2002) presented synthesized analytical data to understand the performance under varying load combinations, field testing and monitoring results of a jointless

bridge West Virginia, and effects of primary versus secondary loads, boundary conditions, and system flexibility on induced stresses at various bridge locations.

Reyes and Robertson (2011) investigated the use of high-performance fiber-reinforced cementitious composite (HPFRCC) reinforced with glass fiber reinforced polymer (GFRP) bars as link-slabs to replace the bridge expansion joints. Several small-scale specimens were tested. Then, a full scale test specimen with a full scale bridge expansion joint was investigated to characterize the performance of HPFRCC with GFRP reinforcing bars. The full-scale bridge expansion joint specimen emulated an expansion joint condition of a composite steel girder to concrete deck slab section. The link-slab was subjected to cyclic axial strains in both tension and compression and later in direct tension until failure. It was found that the cast-in-place link-slab had the advantage of providing good continuity with the bridge deck. The failure was due to rupture of the anchorage at the ends of the link-slab.

Virginia DOT also suggested the shown link-slab detail, Fig. 5.

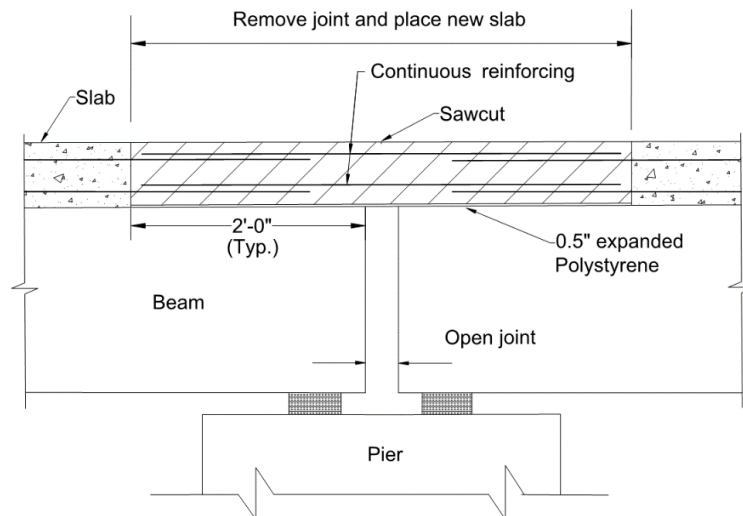


Fig. 5: Use of link-slab by VDOT for rehabilitation work to eliminate expansion joint

Virginia DOT also listed the following types of joint systems used in Virginia, as shown in Figs. 6-13:

- **Armored Joints – Open or Sealed**

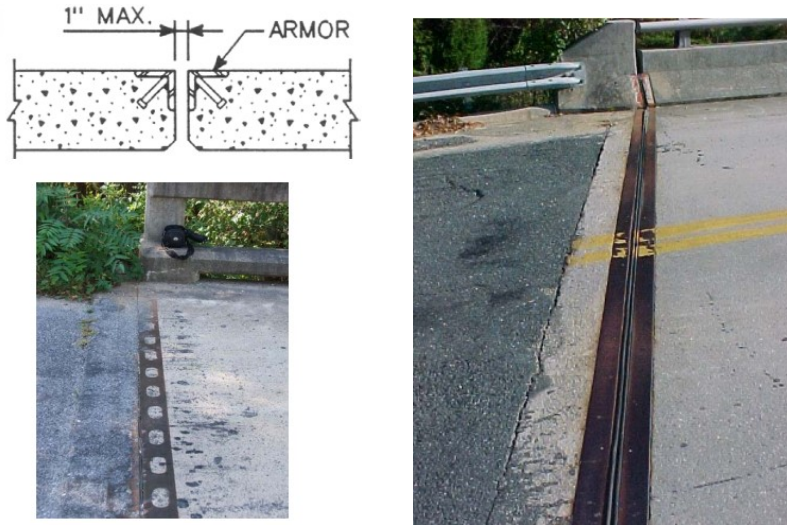


Fig. 6: Armored Joints

- **Hot Poured Sealer /Expansion Material**

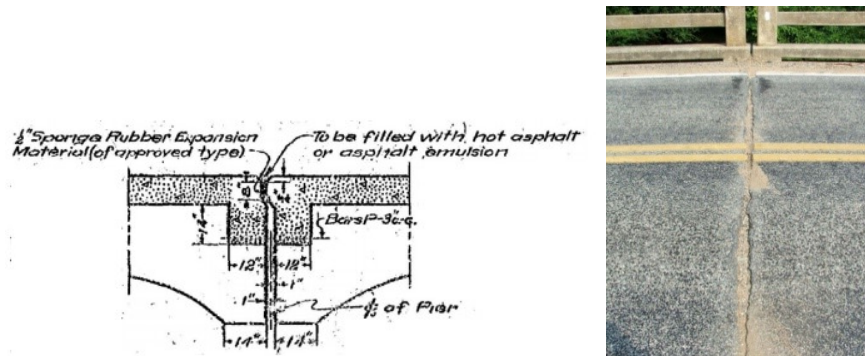


Fig. 7: Hot Poured Sealer

- **Preformed Elastomeric Compression Seals**

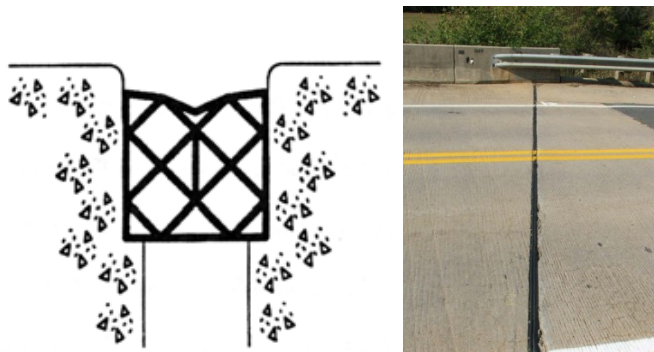


Fig. 8: Preformed Elastomeric Compression Seals

- **Poured (Silicone) Seals**

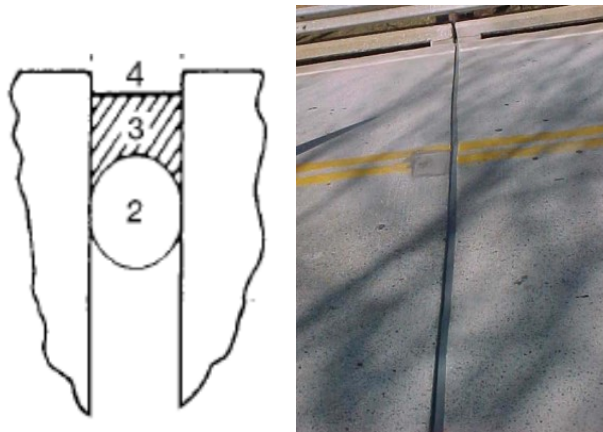


Fig. 9: Poured (Silicone) Seals

- **Asphalt Plug Joints**

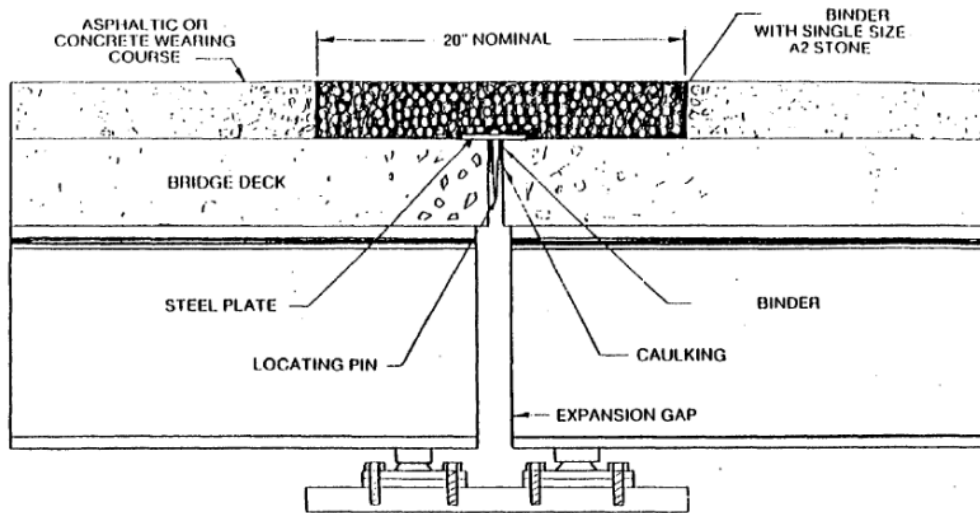


Fig. 10: Asphalt Plug Joints

- Strip Seals

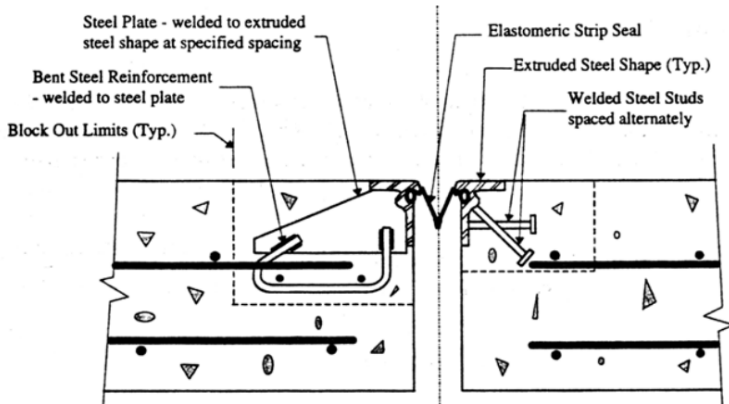
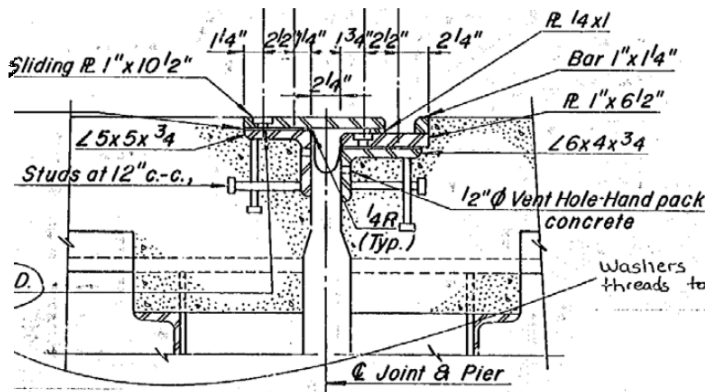


Fig. 11: Strip Seals

- Sliding Plate Joints



- Finger Joints

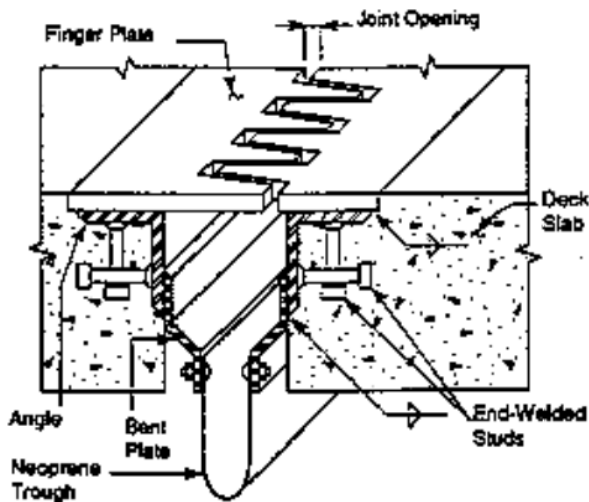


Fig. 12: Finger Joints

- **Cushion Seal (Elastomeric Expansion Dam)**

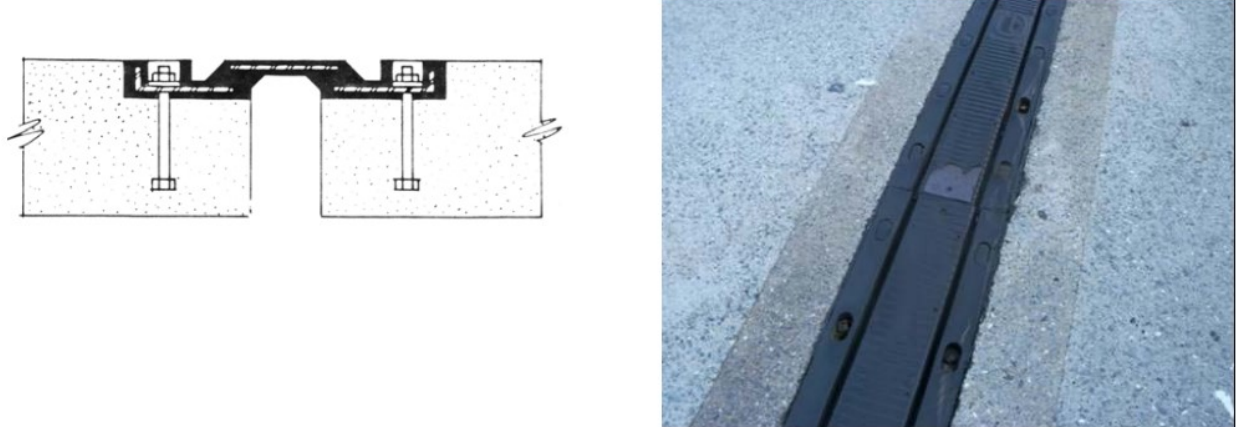


Fig. 13: Cushion Seal (Elastomeric Expansion Dam)

Xu et al. 2018 discussed an approach taken to rehabilitate the Shili Bridge by eliminating expansion joints and retrofitting the structure from simply-supported concrete box girders into a continuous bridge. Condition assessments were performed before retrofitting. In addition, several design options and construction procedures were considered and analyzed. Static and dynamic load tests were carried out after the completion of rehabilitation. The lessons learned in this project are presented and discussed. This practical and novel methodology was a step forward toward improving safety, sustainability, reliability, and quality of such existing bridges in China and elsewhere. It was concluded that Continuity of side-by-side box girders not only eliminated joints between the spans, but also reduced the positive moment at midspan by introducing negative dead load bending moment over the supports. Removal of joints over the abutments enhances bridge durability and eliminates the typical bump at the ends of a bridge. These factors would contribute to improved bridge durability, better ride quality, and reduced maintenance costs. The rehabilitation and strengthening of Shili Bridge provide a basis for the retrofitting of similar existing bridges to address durability and deterioration problems. Providing continuity can also reduce the amount of strengthening materials (CFRP and metal plates) that may be needed along the bottom of the girders. This is because the length of the positive bending moment region would be shortened after continuity of girders is achieved, thus reducing construction quantities and achieving overall cost savings. Steps must be taken to limit any restraints to the free sliding of the approach slab. A separation is needed between the sliding approach slab and the curbs to ensure that the approach slab can slide as freely as possible.

Groli et al. (2014) conducted an experimental campaign aimed at validating a previously published simplified serviceability design method of the columns of long jointless structures. The proposed method was also extended to include tension stiffening effects which proved to be significant in structures with a small amount of reinforcement subjected to small axial loading. This refinement allowed significant improvement of predictions for this type of element. The campaign involved columns with different reinforcement and axial load ratios, given that these parameters had been identified as crucial when designing columns subjected to imposed displacements. Experimental results were presented and discussed, with particular regard to cracking behaviour and structural stiffness. Considerations on tension stiffening effects were also made. Finally, the application of the method to typical bridge and building cases was presented, showing the feasibility of jointless construction, and the limits which should be respected.

Mothe (2006) investigated the behavior of the link-slab and its effect on the behavior of the bridge system as a whole. The scope of the study was to develop FE models to analyze the variation of forces, stresses and moments in the link-slab as well as the level of continuity generated in the girder system. The analysis was carried out for different bridge parameters which are likely to affect the behavior of link-slab; namely, bearing stiffness, skew angle, span lengths and debonding length ratio of link-slab. The study helped in understanding the effects of the aforementioned factors on the behavior of the link-slab and the system. The study also proposed development of a modified three moment equation for different parameters. The parameters which influence the three-moment expression are the bearing stiffnesses, material properties and geometric information. A thorough parametric study is required to validate the expression. The results can be used for development of a design procedure for the link-slab and the expression can be used for analysis of the link-slab. The results obtained showed that the link-slab behaves more like a tensile member rather than a bending member with the increase in bearing stiffness and debonding length ratios. This observation was consistent in all the bridge types and skew angles considered for the study.

Ho and Lukashenko (2011) described the available design methodologies and provide an example of its application for a bridge retrofit. Link-slabs are currently being installed in new bridge construction, and also used to replace expansion joints in the rehabilitation of existing structures. The applicable use of link-slabs in the field is limited by variables such as girder end rotation from applied loads, bridge skew, and girder depth. Link-slabs are designed to flex, however excessive deflection causes potential for the development of wide cracks, exposing the interior steel reinforcement to susceptibility of corrosion. The concrete deck is typically composite with the supporting steel or concrete girders but is debonded in the link-slab region to increase the link-slab curvature length, resulting in a reduced slab flexure and minimizing cracking. Although flexural cracking cannot be completely eliminated, water ingress into the cracks can be controlled by the following design considerations: limiting deck crack opening width by limiting end girder rotation; application of waterproofing membrane on top of concrete deck; and use of fiber reinforced concrete in the link-slab. It was indicated that examples of successful link-slab applications have been implemented in Ontario, Canada and Michigan, USA. The benefits of the use of link-slabs include reduced costs for maintenance of expansion joints, and less reinforcing steel in the deck resulting in less construction time and cost. Also with the elimination of expansion joints, there is less likelihood of chlorides permeating through the joint and causing corrosion and damage to the reinforced deck and substructure components. The use of link-slabs are slowly gaining acceptance as Canadian Ministries of Transportation learn more about their benefits of reduced maintenance costs over the lifespan of new or rehabilitated structures. It is recommended that these link-slabs be monitored over their service lives to better determine their long-term effectiveness.

Kendall et al. (2008) developed and applied an integrated life-cycle assessment and life-cycle cost analysis model to enhance the sustainability of concrete bridge infrastructure. The objective of that model was to compare alternative bridge deck designs from a sustainability perspective that accounts for total life-cycle costs including agency, user, and environmental costs. A conventional concrete bridge deck and an alternative engineered cementitious composite link-slab design were examined. Despite higher initial costs and greater material related environmental impacts on a per mass basis, the link-slab design results in lower life-cycle costs and reduced environmental impacts when evaluated over the entire life cycle. Traffic delay caused by construction comprises 91% of total costs for both designs. Costs to the funding agency comprise less than 3% of total costs, and

environmental costs are less than 0.5%. These results showed life-cycle modeling is an important decision-making tool since initial costs and agency costs are not illustrative of total life-cycle costs. Additionally, accounting for construction-related traffic delay was vital to assessing the total economic cost and environmental impact of infrastructure design decisions.

New York DOT

New York DOT has been building integral bridges as well as jointless decks since the late 1970s. They performed well from the beginning, but a recent study evaluated their performance to identify details possibly needing improvement in future construction. Ratings obtained during a field survey of numerous integral bridges and jointless bridge abutments were analyzed, as well as condition ratings assigned by bridge inspectors during their biennial inspections (Alampalli and Yannotti 1998). Results indicate that these bridges have been functioning as designed and showed superior performance when compared with conventional bridges. These types thus should be used whenever possible to eliminate joints in bridge construction. Details needing improvement were identified. On the basis of these observations, design changes have been recommended for future construction. Integral bridges will be limited to structures having skews less than 30 degrees pending further study. A research project was initiated for further examination of construction practices and assumptions made during the design process.

North Carolina DOT

Gastal and Zia (1989) performed an analysis of bridge beams with jointless decks. ElSafty (1994) conducted an analysis and investigation of jointless bridge decks with partially debonded simple span beams. Zia et al. (1998) investigated casting fully-continuous deck over simply supported girders with partial debonding of the deck from the girders ends at supports, using both numerical and experimental analysis, as shown in Fig. 2. Okeil and Elsafty (2005) investigated the partial continuity in bridge girders with jointless decks and the effect of the system's support configuration on the axial force developed in the link-slab. Caner and Zia (1998) presented the results of a test program to investigate the behavior of link-slabs connecting two adjacent simple-span girders and proposed a simple method for designing the link-slab. ElSafty and Okeil (2008) also investigated extending the service life of bridges using continuous decks. Wing and Kowalsky (Wing 2005) evaluated the link-slab concept proposed earlier by Caner and Zia (1998),

constructed, and instrumented a full-scale jointless bridge and its link-slabs for performance evaluation. This study has concluded that although the design rotation of the link-slab, obtained by assuming simply-supported deck, was 0.002 radian, actual rotation was far below this value. However, to control crack width, link-slabs were still heavily reinforced, thus stiffening the slab and decreasing its ability to act as a hinge between the adjacent decks. In addition, the study suggested that the performance of reinforced concrete link-slabs was highly affected by the construction quality, which most often results in large crack width.

Michigan DOT

ECC: To overcome the problem of heavily reinforced link-slabs, Engineered Cementitious Composites (ECC) were proposed to replace conventional concrete slabs. ECC are high performance fiber reinforced cementitious composites that have high durability and strain capacity over 400 times that of a normal concrete. The tensile strain of ECC material was associated with a large number of microcracks that have a limited crack width between 50 μm and 70 μm at 1% tensile strain. These cracks do not increase in width with increasing the tensile strain even up to failure (4% strain) (Lepech and Li - 2009). Kim et al. (2004) have evaluated the performance of bridge deck link-slabs designed with ductile ECC experimentally using full-scale slabs. The results of these experiments have shown significant enhancements in deflection capacity and crack width control of link-slabs when constructed using ECC material.

Li et al. (2003 and 2005) conducted a research project with Michigan DOT describing the development of durable link-slabs for jointless bridge decks based on strain hardening cementitious composite - engineered cementitious composite (ECC). Specifically, the superior ductility of ECC was utilized to accommodate bridge deck deformations imposed by girder deflection, concrete shrinkage, and temperature variations, providing a cost-effective solution to a number of deterioration problems associated with bridge deck joints. Current design concept of link-slabs was first examined to form the basis of design for ECC link-slabs. Microstructurally optimized ECC material, with good workability and satisfactory mechanical properties was then developed. After the material design, the shrinkage, shrinkage crack resistance and the freeze-thaw behavior of the pre-selected mix proportion was investigated and revealed excellent for the durability concern. Improved design of ECC link-slab/concrete deck slab interface was confirmed

in numerical analysis and further strengthened by excellent reinforcement pullout and shear stud pushout behavior in ECC. Based on the above findings, monotonic and subsequent cyclic tests of full-scale ECC link-slab specimens were performed and compared with those of a conventional concrete link-slab. It was revealed that the inherent tight crack width control of ECC decouples the dependency of crack width on the amount of reinforcement. This decoupling allows the simultaneous achievement of structural need (lower flexural stiffness of the link-slab approaching the behavior of a hinge) and durability need (crack width control) of the link-slab. Overall investigation supported the contention that durable jointless concrete bridge decks may be designed and constructed with ECC link-slabs. Finally, a simple design guideline was presented. Also, the results of full-scale mixing trials and demonstrations were summarized, and recommendations were made along with batching sequences and mix designs for large scale mixing. A summary of construction practices and procedures was also included, followed by the results of full-scale load testing on the completed ECC link slab demonstration bridge. The load tests concluded that the ECC link-slab functions as designed under bending loads.

The Michigan DOT incorporated link-slabs during deck replacements and deep resurfacing. Field performance assessment documented full-depth cracking of most of the link-slabs. These cracks allow surface water infiltration, which leads to accelerated deterioration. Ulku et al. (2009) conducted a study to address link-slab design and performance issues. The literature is inconsistent with the influence of design parameters on link-slab performance. The objective was to document the link-slab behavior of its design parameters, to propose a method to calculate the link-slab moment and axial force, and to propose recommendations for updating current design details and construction procedures. Single-girder, two-span, finite element assemblage models under various types and levels of loads in conjunction with the link-slab design parameters were used to evaluate the moments and axial forces developed in the link-slab. Analysis showed that support conditions underneath the link-slab greatly influence the link-slab moment and axial force. Use of moment interaction diagram is recommended for the design. A detailed analysis and design example is presented incorporating live load, temperature gradient load, and the support configurations.

Lepech and Li (2009) investigated the application of ECC in a bridge deck link-slab. The unique ultra-high tensile ductility and tight crack width of self-consolidating ECC was exploited in this

application to improve bridge deck constructability, durability, and sustainability. Design guidelines and material specifications were developed for implementation of this ECC link-slab technology. A construction project implementing these guidelines and specifications was conducted in 2005 on an ECC-concrete bridge deck in southeast Michigan, USA. A full-scale load test was conducted to explore the structural response of the constructed ECC link-slab. These load tests validated that the incorporation of an ECC link-slab in placement of a conventional expansion joint did not alter the simply supported nature of the bridge spans, and that ample strain capacity of the ECC is reserved for temperature induced straining as designed. Two years after this ECC link-slab was placed, the performance of this link-slab remains unchanged. With further long term performance monitoring and additional demonstration experience, ECC link-slab can be an effective replacement of conventional expansion joints resulting in significantly reduced bridge deck maintenance needs.

Georgia DOT

Snedeker et al. (2011) evaluated the performance history of continuous bridge decks in the State of Georgia, to determine why the current design detail works, to recommend a new design detail, and to recommend the maximum and/or optimum lengths of continuous bridge decks. The continuous bridge decks have continuous reinforcement over the junction of two edge beams with a construction joint for crack control. It was indicated that the current technical literature and current practices and design procedures were synthesized and summarized. GDOT maintenance reports were reviewed, and preliminary field evaluations were conducted to determine the performance of the continuous deck detail. The effects of bridge movement due to thermal strains, shrinkage, and live loads were considered in simplified analytical studies to better understand the demands placed on the GDOT continuous deck detail. A summary of the preliminary design and length recommendations were provided upon completion of Part 1 of the research.

Europe

In recent years, the so called jointless or integral bridge design has seen a significant rise in popularity in Europe. Whereas in the last decades, designers preferred clearly defined statical systems and only adopted jointless design principles for small structures, the new generation of engineers pushes for integral design wherever possible. This development is to some degree

motivated by a paradigm shift towards life-cycle cost-orientated design. Integral bridge structures lack joints and bearings, which typically are the least durable elements and thus remove the need for costly inspections and replacements. However, the obvious advantage of reduced direct and indirect maintenance costs entails novel and complex design solutions, especially for the transition area between structure and soil body. Furthermore, their statically indeterminate nature leads to increased importance of the soil–structure interaction. Both aspects are associated with significant uncertainty.

Wendner and Strauss (2015) focused on the probabilistic performance assessment of an inclined approach slab solution for integral bridge structures of up to 150 m of total length. Findings are presented by the example of a recently constructed and ever since monitored 67-m-long prototype structure. Monitoring data recorded by a multisensor monitoring system during the first 30 months after construction serves as inputs for a probabilistic, extreme value-based assessment of critical design assumptions. In particular, (1) the modeling of boundary conditions, (2) the activated degree of earth pressure against the abutment wall, and (3) the strain distribution in the fiber-reinforced soil above the inclined approach slab were investigated. It was concluded that the combination of short and long extensometers represents a robust and cost-effective monitoring approach for relative and absolute abutment movements that has already been adopted by Austrian bridge owners. The obtained information can be used to investigate the soil–structure interaction in terms of actual boundary conditions and developing earth pressure, in case no other sensor system is available. Based on the observed linear relationship between temperature within the deck slab and recorded abutment movements, it was found that the recorded displacements account for only 42% of the expected displacements, assuming free thermal expansion. Hence, the assumption of free thermal expansion during the design of the dilatation area is highly conservative by itself. In the current engineering practice, the assumption of free thermal expansion compensates for the lack of experience regarding the actual performance of the approach slab that represents a hidden safety margin. The observed strain field is in agreement with the theoretical assumptions, showing a high strain concentration near the tip of the slab and indicating an inclined area of localized deformation going up to the surface.

Charuchaimontri et al. (2008) investigated the influence of lap reinforcement in link-slabs of highway bridges under four independent boundary conditions by using a three-dimensional nonlinear finite element code based on the microplane model. Numerical solutions for load–deflection relationships, internal force distribution and failure cracking planes are presented for link-slabs with different details of lap reinforcement. A full-scale test was performed on three reinforced concrete long span link-slabs with various lap reinforcement details subjected to mid-span loading. The comparison indicated a good agreement between the results from finite element analysis and the experiment. The model can be used to predict the effective moment of inertia of the link-slab under mid-span loading, end rotation and end translation for the development of design criteria for a link-slab.

MTO

To address this problem of joints in bridges, the Ministry of Transportation of Ontario (MTO) has recently rehabilitated a number of bridge decks using a debonded link-slab system to replace the deck joints at the pier locations. MTO recently carried out an experimental research study of the long-term performance of the system on scale test models that were subjected to extensive cyclic loading in the laboratory. It also conducted a load test of a recently rehabilitated structure to study its structural behavior both before and after the link-slab was constructed. The test structure was instrumented with sensors that measured deflections and strains in the link-slab and girders.

Au et al. (2013) described the experimental research study on link-slab and the behavioral load tests that were carried out, and discusses the results obtained. The experimental study showed that the long-term performance of the link-slab was not affected by the extensive cyclic loading to which the model was subjected, and the load testing of the test structure showed that it satisfied the serviceability limit state requirements of the Canadian Highway Bridge Design Code, thus validating the design methodology of the system.

PCI

Details of jointless bridge superstructures are available in the PCI publication, “The State-of-the-Art of precast/Prestressed Integral Bridges,” authored by the Subcommittee on Integral Bridges of the Committee on Bridges.

THE USE OF FRC and FRP REBAR IN LINK-SLABS

Several researchers have investigated the use of Fiber-Reinforced Polymers (FRP) for bridge deck reinforcement (NCHRP – 2003) as alternatives to conventional steel reinforcement to provide corrosion resistant reinforcement that increases bridge service life and achieve economic and environmental benefits

FRC

Materials with high tensile strain capacity, such as fiber-reinforced concrete (FRC), can be used for application in the link-slab to improve the strength, durability, and cracking characteristics of the link-slab. Hong (2014) established a computational model of an existing bridge (Camlachie Road Underpass). It is found that the model and modelling approach in SAP2000 closely predicted the field test results obtained by the Ministry of Transportation of Ontario (MTO). Additionally, it is established that the horizontal stiffness of the elastomeric bearings is very low and therefore the supports are representative of roller supports. Therefore, axial forces are not generated when there are no horizontal restraints in the supports.

Hong (2014) examined the properties of FRC from experimental tests. Four-point bending tests are used to estimate the ultimate and service stresses of FRC using procedures from the fib Model Code (2010). It is found that the results from the fib Model Code are in agreement with the experimental beam tests by Cameron. Therefore, it is concluded that the fib Model Code procedures are valid for calculating the ultimate and service stresses in FRC and are used in the computational and analytical models. Hong 2014 conducted a parametric study to provide a better understanding of link-slab bridge behavior to assess the impact of design decisions on the bridge response. It is found that the use of hooked steel fibres minimized the crack width of the link-slab, and a debonded length a 5% to 7.5% is found to be optimal based on cost and serviceability. Moreover, it is found that fibres are more effective when less steel reinforcements are used in the link-slab. Lastly, a parametric study is conducted on the computational model using non-linear analysis by including FRC in the computational model in the form of plastic hinges. It is concluded that the computational model has shown signs of cracking at the pier supports, which is consistent with the site observations during the MTO field test for the Camlachie Road Underpass. Hong 2014 developed an analytical model (i.e., design guideline) on the analysis and design of link-slab

bridges with FRC. It is found that the proposed analytical model is able to closely represent the link-slab bridge behavior with very small difference (2-3%), whereas the current method of analysis using Caner and Zia's approach shows a larger prediction error (16%). For the link-slab design with FRC, it is found that fibres in reinforced concrete helped increase the bending moment capacity of the link-slab by more than 10% compared to normal reinforced concrete (without fibres). The use of polypropylene fibres and hooked steel fibers in the link-slab reduces the required steel reinforcement by 3.5% and 21%, respectively, and the crack width of the link-slab reduces by more than 3 times with the addition of fibres. Okeil et al. (2013) conducted a field study in Louisiana investigating the performance of a skewed prestressed concrete bulb-tee girder bridge made continuous. The study presented details of the monitoring system developed for this project, which has been in service for more than two years. Temperature, strain, rotation, and elongation readings are presented. It was concluded that positive moments develop in bridges employing the new continuity detail. They are caused by creep and thermal effects that cause upward camber at midspans, which leads to positive moments at continuous girder ends. Seasonal and daily temperature variations can induce large restraint moments in the bridge, especially temperature gradients. The level of restraint moment due to the combined seasonal and daily temperature effects is probably the most important factor in the design of this detail because the designer has no influence on the temperatures at the bridge site. The other positive-moment-inducing factor (girder creep caused by prestressing forces) can be greatly reduced by not establishing continuity until after a large portion of the creep takes place.

Hawaii DOT

Reyes and N. Robertson (2011) in the report of the State of Hawaii Department of Transportation indicated that a cast-in-place link-slab has the advantage of providing good continuity at the ends of the FRCC section to the concrete or bridge deck, meaning it can be built to be flush with the bridge deck. However, because of the limitation of permanent strain in the link-slab, the effectiveness of the slab in compression is reduced. Therefore, a precracked link-slab would be more appropriate in most applications. The study also indicated that because HPRCC concrete requires a long setting and curing time to reach its optimal strength, it may not be practical to cast-in-place especially when time is a construction consideration. The study also suggested that pre-cast slabs has the advantage of pre-cracking but are limited by the bond of the link-slab to the

existing concrete. It suggested bonding through vertical dowels installed at an angle so that the slab is essentially pulled downward during tension loads, or a combination of vertical dowels and horizontal GFRP bars that would be more effective than either acting alone

TYPES OF BEAM CONTINUITY AT PIERS

There are several alternatives to create a link-slab and or jointless superstructure over the piers. AASHTO LRFD specifications (2009), Article 5.14.1.4 allows designers to use any one of the shown methods of design. Some examples of these jointless superstructure are listed as follows:

(a) Continuous deck slab or link-slabs supported by simple span beams

Most of the concrete beam bridges in Florida are currently built using continuous deck over the joint between beams/girders at a pier. A typical detail is shown in Fig. 14. The details do not include beam end diaphragms or debonding between the deck and beam. The absence of end diaphragms in these details significantly simplifies construction but may not be feasible in states subjected to significant seismic activities. Some of the details include a saw-cut or tooled crack control joint in the deck over the pier that may be filled with sealant.

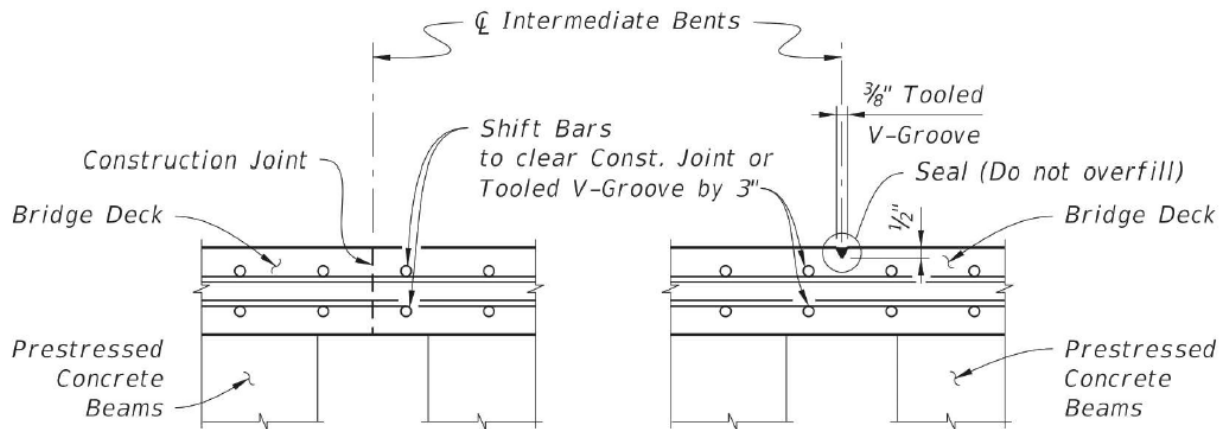


Fig. 14: Florida Department of Transportation details for continuous slab over joint between simple spans. Figure: Florida Department of Transportation Structures Detailing Manual

A similar method is also adopted using a link-slab to connect the simply-supported girders/beams with a continuous deck, while part of the slab is debonding from the girder ends at both sides of the joint. This detail of the link-slab with debonding results in a reduction in developed strains

and cracking in the continuous deck slab since it distributes the deformations over a greater length. This method has a simpler construction than a fully continuous superstructure and is considered as a cost-effective way of developing a jointless deck. To control cracking, a groove is formed, preinstalled or cut transversely in the deck at the pier centerline and may be filled with a sealant. Several researchers [ElSafty (1994); Zia et al. (1995)] provided early recommendations for design and construction of link-slabs. They recommend debonding the end 5% of the deck slab from the ends of the beams to reduce strains and control cracking in the link-slab region. Recommended analysis is to impose the end rotations of the beams on the slab. The resulting stress in the deck reinforcement should be limited to 40 ksi and cracking should be checked with current AASHTO LRFD specifications crack control provisions.

Virginia DOT

An example of a link-slab system used to remove expansion joints when rehabilitating bridges in Virginia is shown in Fig. 15. In this detail, which is used for relatively short spans, the debonded length is a constant 2 ft (VDOT 2013).

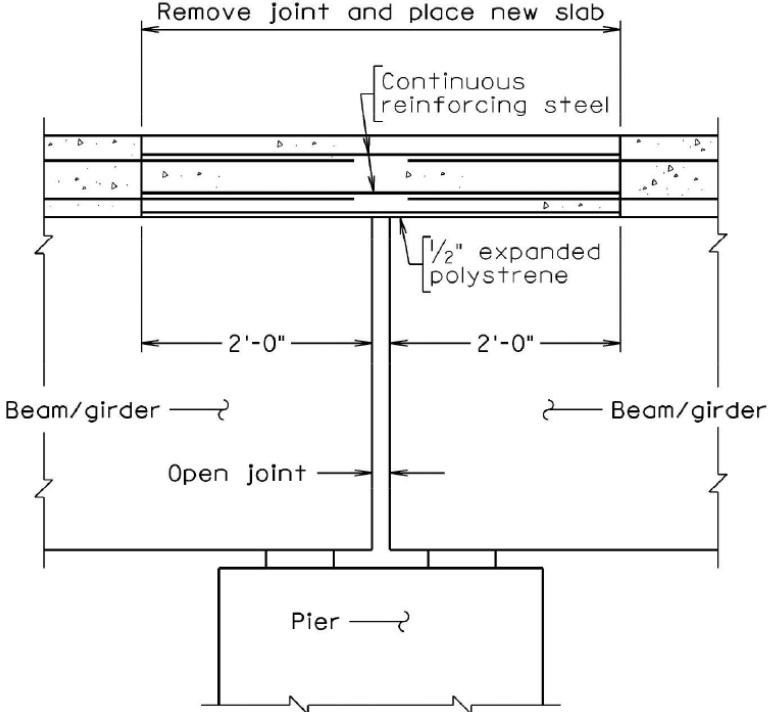


Fig. 15: Link-slab detail used by Virginia Department of Transportation to eliminate expansion joint in rehabilitation projects

(b) Continuous-for-Live-Load Beams

The prestressed concrete beams are set on bearings as simple spans and the diaphragm concrete may be placed partial height (Fig. 16). The deck concrete is then placed on the simple-span beams. Longitudinal deck reinforcement that extends over the pier region is designed to resist all subsequent loads, such as live load, as a continuous span composite superstructure. This system has been performing well for more than 40 years.

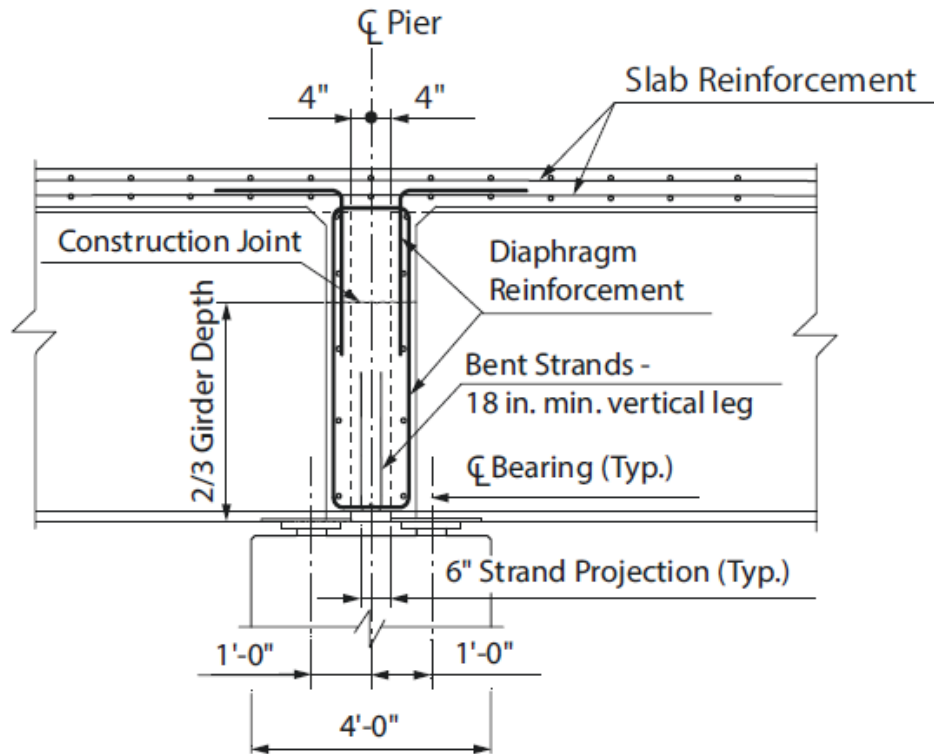


Fig. 16: Example of pier diaphragm details with either fixed or expansion bearings (Tadros 2016)

(c) Threaded Rod Continuity System

A method called threaded rod continuity was reported by Sun et al. (2016), where beams were made continuous using high-strength threaded rods placed on top of the beams in the negative moment zone over the piers. The rods were embedded in a concrete placement on the top flange of the beam that is constructed at the same time as the continuity diaphragm, as shown in Fig. 17. The result is a continuous beam for deck weight as well as all subsequent loads. This system, while slightly more complicated than the continuous-for-live-load system, allows for further

optimization of the capacity of the beams. Also, as an additional benefit, the negative moment due to deck weight generally offsets the long-term positive restraint moment at the pier, eliminating the need for bars or strands extending from girders to provide a positive moment connection.

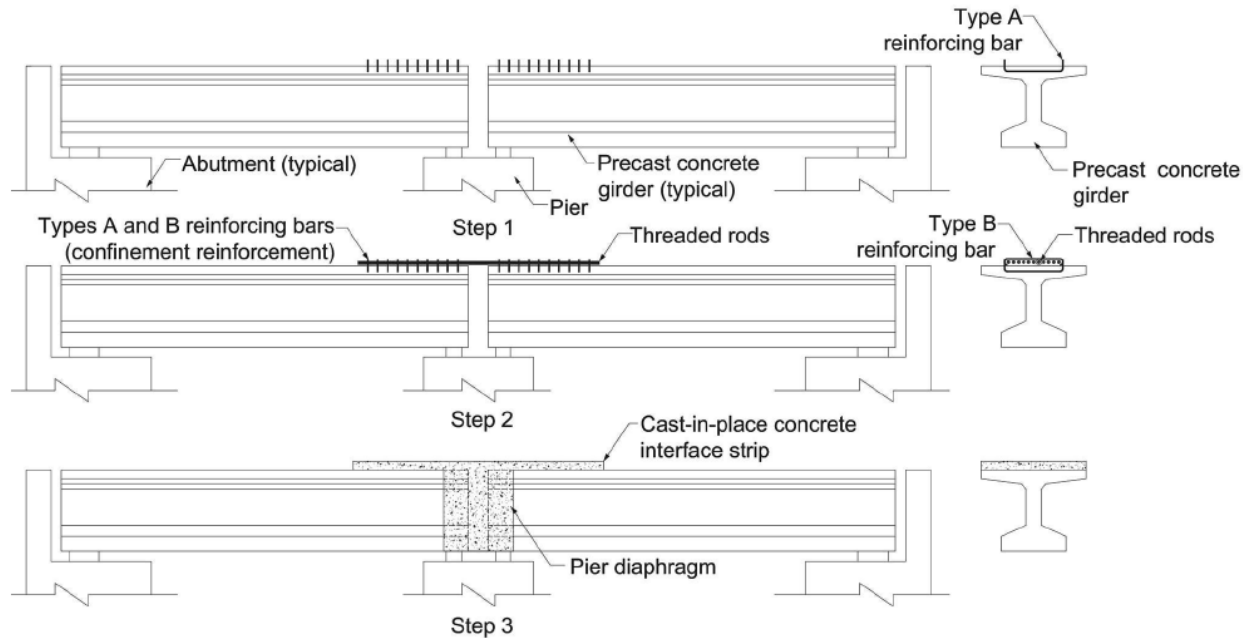


Fig. 17: Construction steps of implementing threaded rod continuity system prior to deck placement (Sun et al. 2016)

(d) New Link-slab System Details

Louisiana Transportation Research Center proposed a link-slab to be designed with enough FRP reinforcement to withstand the loads placed on the slab. Also, when possible, the link-slab was designed to be uncracked while under typical service loads. Design has been in accordance with the newest ACI 440 criterion. When creating the FRP link-slab, special measures should be considered to anchor the FRP reinforcement to the existing bridge deck during the installation of a link-slab in an existing deck. Using FRP grating or FRP bars for the creation of a link-slab in a new bridge or a complete bridge deck replacement was considered.

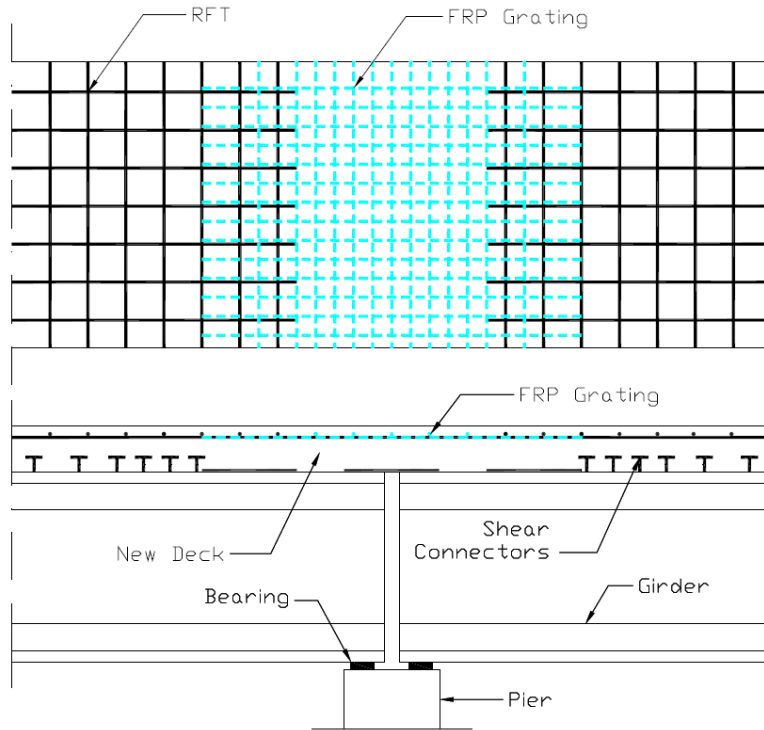


Fig. 18: FRP grating as reinforcement for new link-slab.

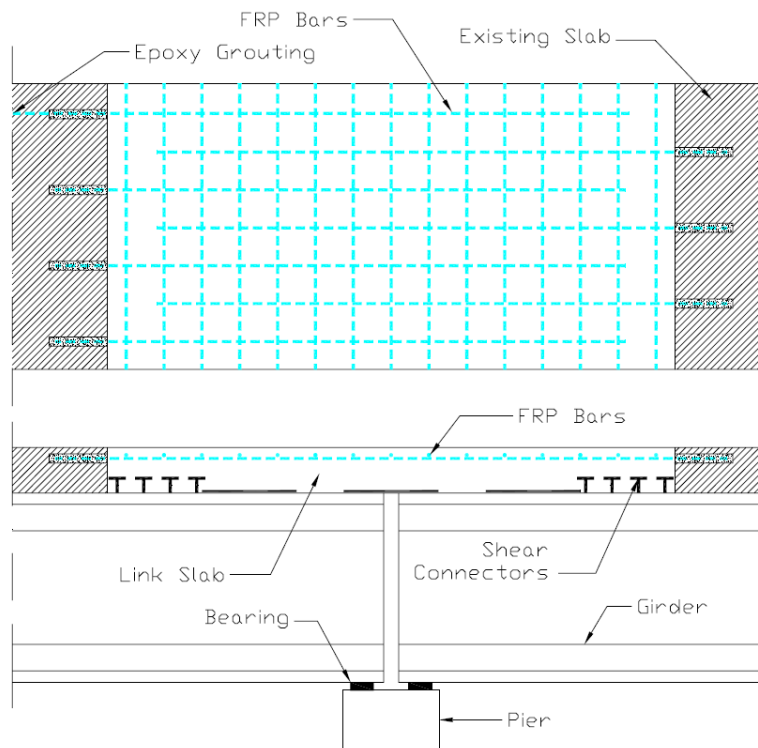


Fig.19: FRP rebar for use in link-slab installed in existing deck

INSTRUMENTATION OF THE LINK-SLAB

Researches have indicated that the link-slabs were instrumented using real-time strain inducers, thermocouples, and pH meters. Data was collected during field tests and service. The data logger has record when certain strains were reached in the FRP reinforcement.

Okeil, et al. (2013) investigated a precast prestressed-concrete simple-span girders that were made continuous by pouring a continuity diaphragm between the girders ends. Special reinforcement was extended from the girders' bottom flanges into the diaphragm to ensure continuity under positive moments that result from time-dependent effects such as creep, shrinkage, and temperature gradient. The bridge has been instrumented with embedded and surface-mounted sensors and was monitored for over 2 years to evaluate the performance of the new continuity detail. A live-load test was carried out to evaluate the response of the new detail under truck loads. A bridge segment was monitored that was a three-span continuous superstructure, 242 ft (73.8 m) long with a 45-degree skewed layout. American Association of State Highway and Transportation Officials (AASHTO) bulb-tee girders (BT-72) were used for the construction of this segment. Because of the bridge's symmetry, only one of the identical intermediate bents was monitored. A 96-channel monitoring system was designed to record essential performance measures for evaluating the continuity detail. Several sensor types were chosen to measure temperatures, strains, rotations, crack widths, and gaps. All sensors used the vibrating wire technology, which is known to be more suitable for long-term monitoring projects because they do not suffer from drifting. Embedded as well as surface-mounted sensors were employed.

Six types of sensors were used, and the monitoring system included 66 active sensors. The sensors were strategically located at midspan and on both sides of the continuity diaphragm to capture the important measures that are most influenced by continuity, such as strains in hairpin bars and the gap between adjacent girder ends. The relative movement between the bottom flanges at the ends of the adjacent girders on both sides of the continuity diaphragm was investigated using the gapmeters installed at girders. Rotations on both sides of the continuity diaphragm were recorded. All measurements were corrected for temperature changes per recommendations of the gauge manufacturer. Figure 20 shows a schematic of the sensor locations. Okeil et al. (2013) provide more details about the instrumentation. Figure 21 shows instrumentation options and details.

Live load test on the monitored segment was conducted to assess the continuity detail's performance under truck loads. Dump trucks weighing 54.1 and 57.0 kip (24.5 and 25.9 tonnes) were used to load the bridge in nine static loading cases.

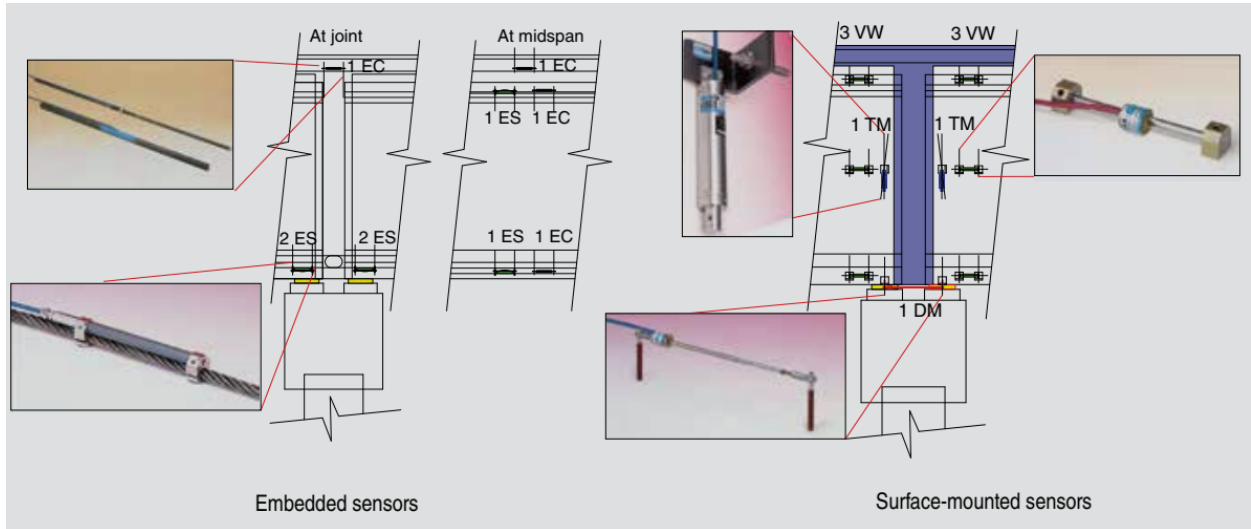
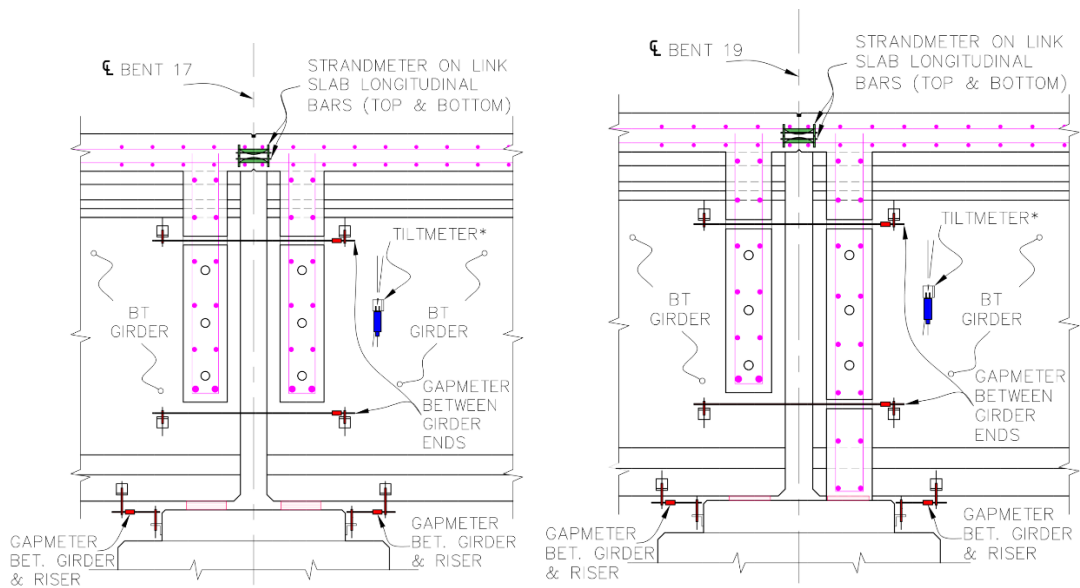


Fig. 20: Distribution of sensors at each monitored location. Note: DM = gapmeter gauge; EC = sisterbar gauge; ES = strandmeter gauge; TM = tiltmeter gauge; VW = vibrating wire strain gauge.



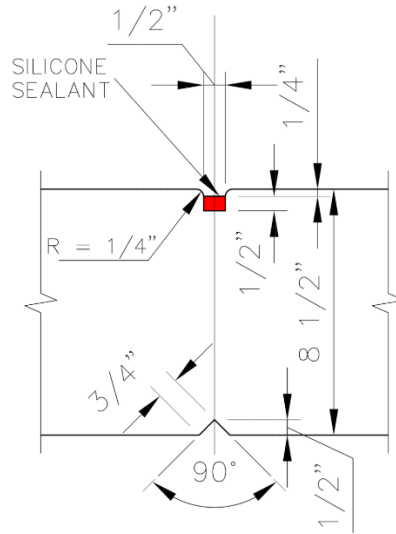


Fig. 21: Details of typical instrumentations

The monitoring of the tested bridge indicated that the continuity detail has the ability to transfer forces from one girder to the adjacent girder across the continuity diaphragm, as evidenced by the recorded data under long-term effects as well as live loads.

The authors concluded that seasonal and daily temperature variations can induce large restraint moments in the bridge, especially temperature gradients. The level of restraint moment due to the combined seasonal and daily temperature effects is probably the most important factor in the design of this detail because the designer has no influence on the temperatures at the bridge site. The other positive-moment-inducing factor, such as girder creep caused by prestressing forces, can be reduced by not establishing continuity until after a large portion of the creep takes place. The results from the instrumentation and monitoring also indicated that the live load test revealed that the continuity detail transferred negative and positive moments across the diaphragm. The strains from the live load test were lower than long-term effects. Even if the actual design load was to be applied (approximately twice the test live load), the strains would still be small. Therefore, the live load case should be considered in the design; however, it is not the most demanding action on the detail.

12 Appendix E

ANNOTATED PLANS DETAILS FOR LINK-SLAB MONITORING PROJECT BDV34 986-02

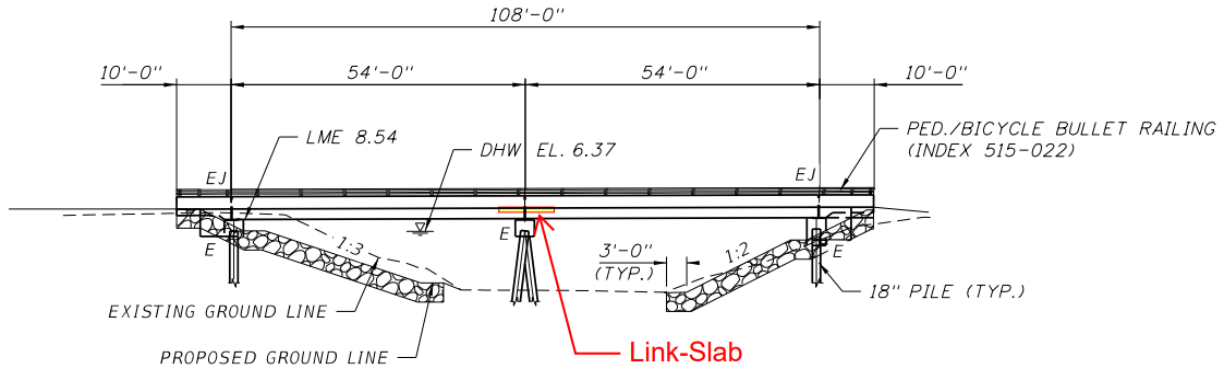
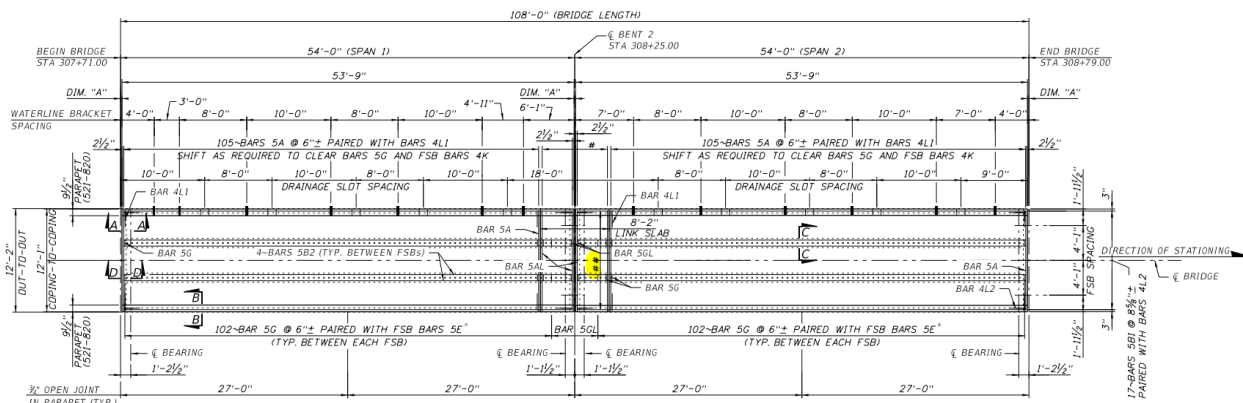


Figure E.1: Elevation of the Bridge with the link-slab (Bridge No. 019003)



These longitudinal bars are replaced with Basalt FRP under BDV34 986-02 monitoring project

17-BAR 5A1 @ 6"±
24-BAR 5G1 @ 6"± PAIRED WITH FSB 5E"

Figure E.2: Plan view of the Bridge with the link-slab (Bridge No. 019003)

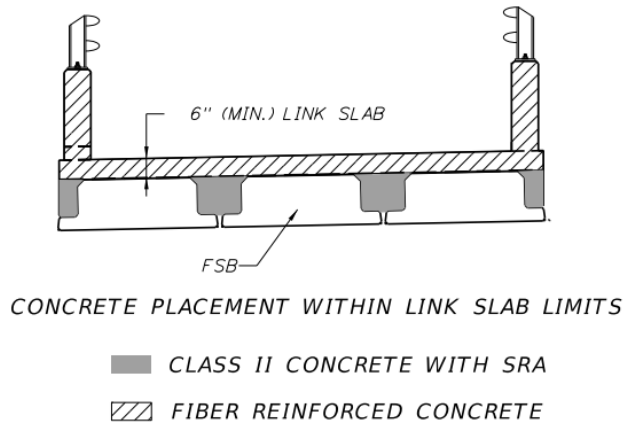
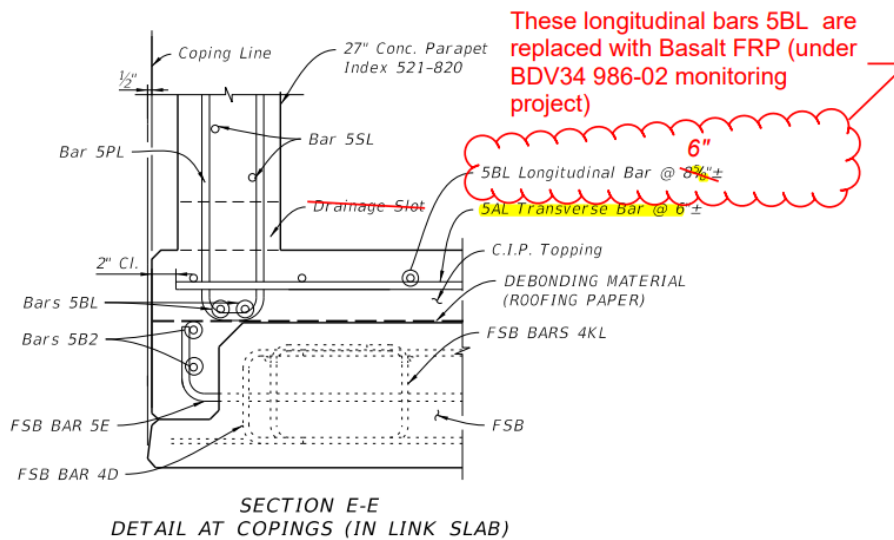


Figure E.5: Concrete within the link-slab (Bridge No. 019003)



Pedestal reinforcing bars within the limit of the link slab shall be GFRP Bars and shall be incidental to the cost of the parapet.

Figure E.6: Concrete within the link-slab (Bridge No. 019003)

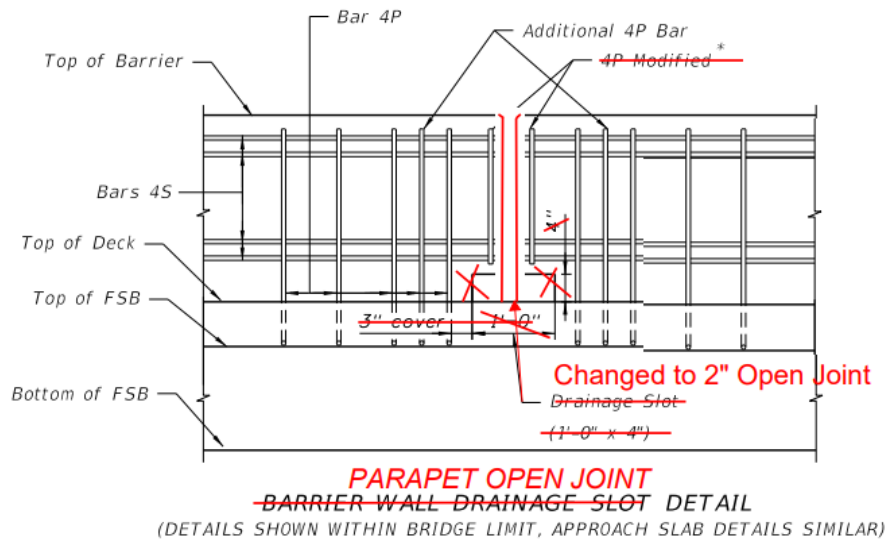


Figure E.7: Detail of the link-slab (Bridge No. 019003)

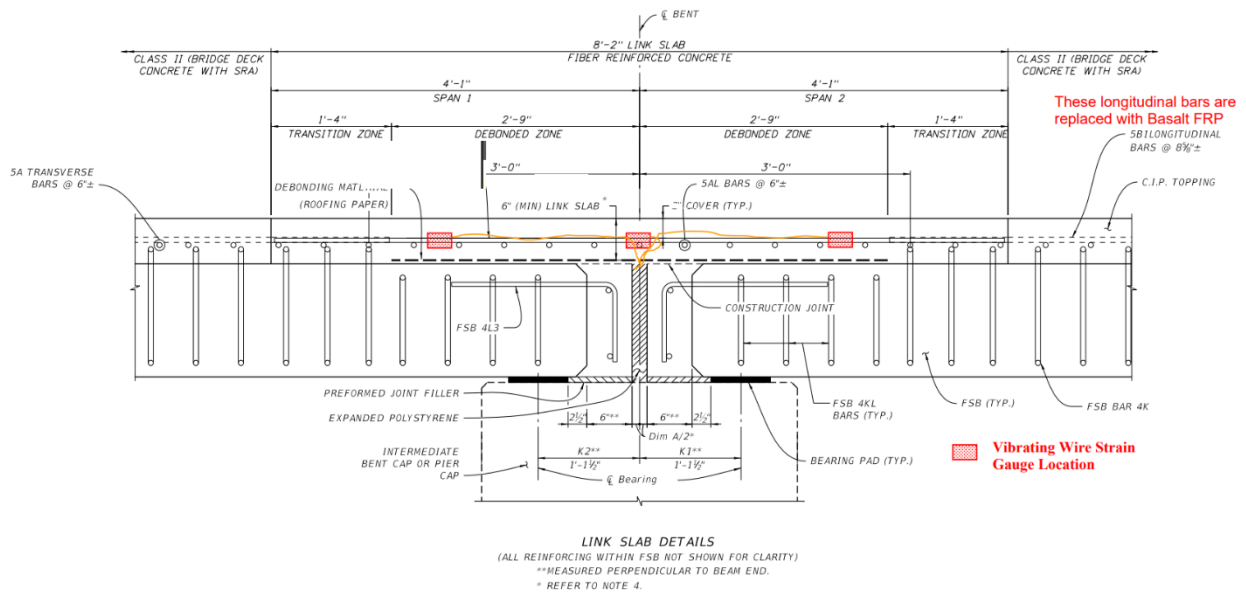
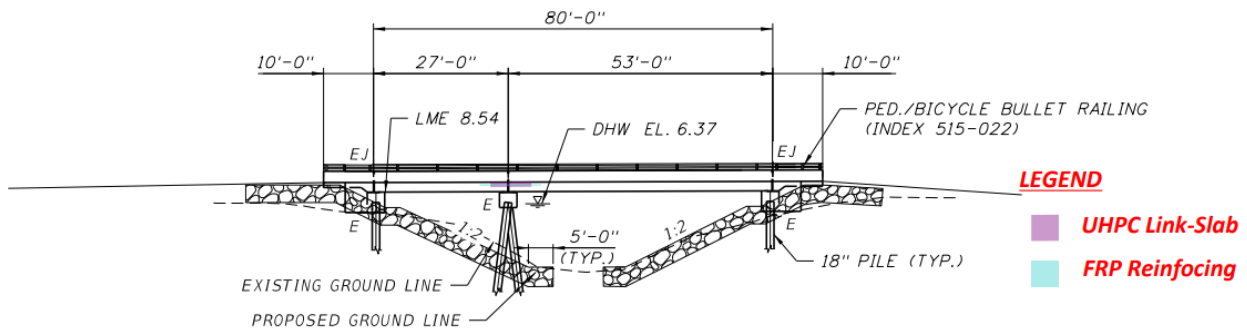


Figure E.8: Longitudinal Section Detail of the link-slab (Bridge No. 019003)



ELEVATION

Figure E.9: Elevation of Bridge No. 019004

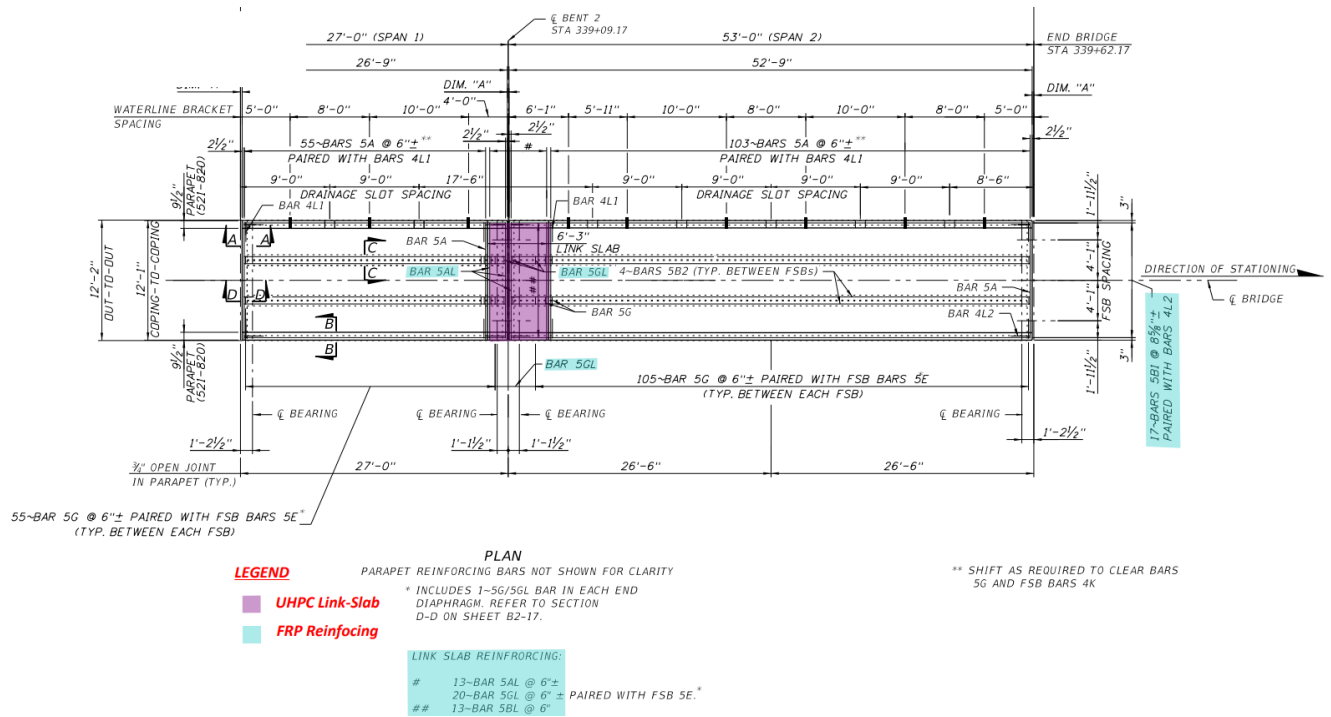


Figure E.10: Plan View of Bridge No. 019004

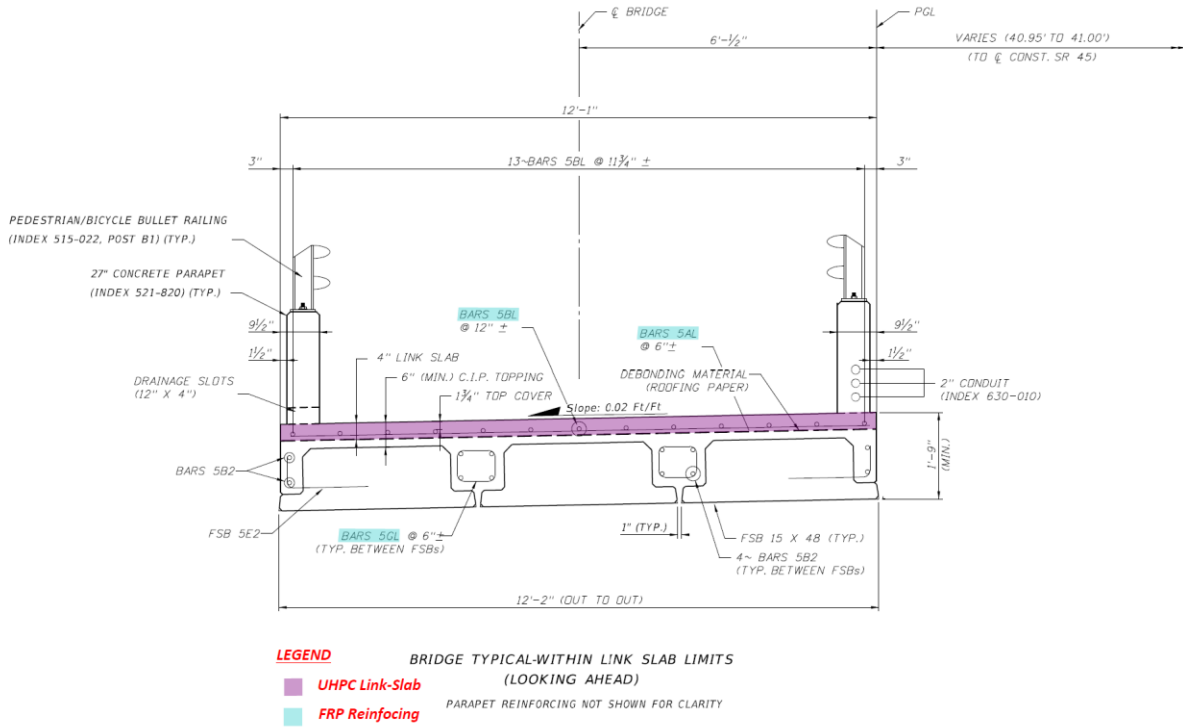


Figure E.11: Sectional cut of link-slab (Bridge No. 019004)

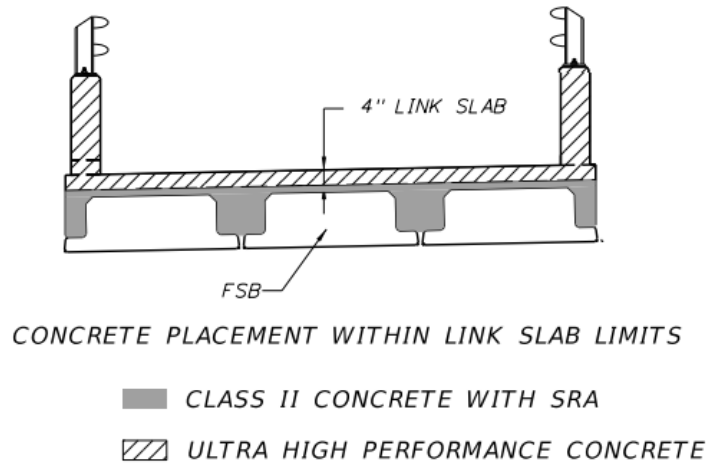


Figure E.12: Concrete within the link-slab (Bridge No. 019004)

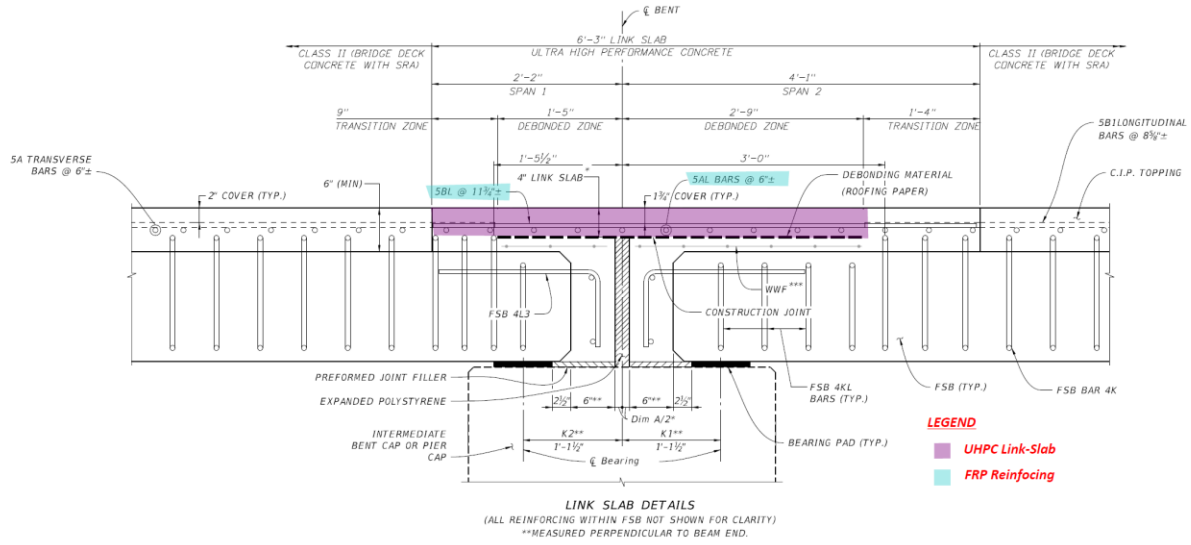


Figure E.13: Link-slab side view (Bridge No. 019004)